QUBIT READOUT WITH THE JOSEPHSON PHOTOMULTIPLIER

by

Guilhem Ribeill

A dissertation submitted in partial fulfillment of
the requirements for the degree of

Doctor of Philosophy

(Physics)

at the

UNIVERSITY OF WISCONSIN–MADISON

2016

Date of final oral examination: 3/29/16

The dissertation is approved by the following members of the Final Oral Committee:
    Robert McDermott, Professor, Physics
    Maxim Vavilov, Professor, Physics
    Mark Saffman, Professor, Physics
    Peter T. Timbie, Professor, Physics
    Mikhail A. Kats, Assistant Professor, Electrical and Computer Engineering

ProQuest Number: 10077441

ProQuest 10077441

Published by ProQuest LLC (2016). Copyright of the Dissertation is held by the Author.

ProQuest LLC.
789 East Eisenhower Parkway
P.O. Box 1346
Ann Arbor, MI 48106 - 1346

A ma famille.

ACKNOWLEDGMENTS

We have come a long way, we have a long way to go. In between, we are somewhere.

— Kim Stanley Robinson

It goes without saying that there are too many people to thank for the help, support, encouragement and occasional prodding that is needed to finish a doctoral program in this short space. My sincere thanks to anyone who was inadvertently left out. You know who you are.

First, I would like to thank my advisor, Robert McDermott. He was the origin of many of the ideas in this thesis and an even larger number of interesting experiments that didn't make it in. Robert taught me how to be a better scientist by making sure every experiment taught me something new, and as we tried to do something no one else had thought to try. Alongside Robert, the other members of the McDermott group have provided a constant source of support and friendship. David Hover and Steve Sendelbach took me under their wings and taught me how to do most of the everyday work around the lab, and I thank them for their humor and patience. Many other graduate students and postdocs in the group took the time to help: Umesh Patel, Ted Thorbeck, Joey Suttle, Matt Beck, Ed Leonard and Chris Wilen made the lab fun and their questions helped sharpen my understanding of what I was doing. Much of the work in this thesis was accomplished in close collaboration with Ivan Pechenezhskiy. He pushed me to step back and understand each piece of the experiment, and always kept me honest with his incredible ability to quickly understand everything we were trying to do. He made me a better scientist and forced me to clean up my atrocious software code, all while making me laugh with his dark sense of humor, and I am happy to count him as a colleague and friend. Thanks to Britton Plourde as well as Caleb Howington, Matt Hutchings and Matthew Ware at Syracuse University for collaborating with us on this project and fabricating qubit chips for us. Finally, I'd also like to thank Luke Govia for always being ready to patiently answer theory questions.

CONTENTS

LIST OF FIGURES

ABSTRACT

Recent demonstrations of error correction in many qubit circuits, as well as efforts to build a logical qubit, have shown the need for a simple and scalable superconducting quantum bit (qubit) readout. Current solutions based on heterodyne detection and cryogenic amplification of microwave readout tones may prove difficult to scale, while photon counting presents an attractive alternative. However, the development of counters operating at these frequencies has proved technically challenging. In this thesis, we describe the development of the Josephson Photomultipler (JPM), a microwave photon counting circuit. We discuss the JPM theoretically, and describe the fabrication of the JPM using standard thin film lithography techniques. We measure its properties as a microwave photon counter using a qubit as an *in-situ* calibrated source of photons. We measure a JPM quantum efficiency at the few percent level. We then use the JPM to perform readout of a transmon qubit in both the dispersive and bright regimes. We observe raw measurement fidelities of 35% and 62% respectively. We discuss how the JPM and measurement protocol could be further optimized to achieve fidelities in excess of 90%.

1 INTRODUCTION

...nature isn't classical, dammit, and if you want to make a simulation of nature,

you'd better make it quantum mechanical, and by golly it's a wonderful problem,

because it doesn't look so easy.

— RICHARD FEYNMAN (1982)

In many ways, human history during the twentieth century has been shaped by the history of computers. Starting with the use of the first large-scale systems used during the Second World War to break Axis encryption, computers have deeply affected the course of world events, the way we live our lives, and even the way in which we think. Alan Turing's paradigm of the universal computer now transcends its origin in pure mathematics and informs how we think about questions in science, in fiction, and even human cognition. From the invention of the first solid-state transistors by Bardeen, Brattain and Shockley in 1947, physicists have been intimately involved in the bewildering pace of innovation and miniaturization of digital computers that has made them as ubiquitous as they are powerful. As we approach the third decade of the twenty-first century, what new paradigms can we look towards to continue to expand the reach of computers?

1.1 Quantum Computers

In a 1981 speech [45], Richard Feynman challenged the assembled physicists to envision a different kind of computing machine: one that would explicitly use

the rules of quantum mechanics to simulate nature. As he pointed out, the use of a quantum system is necessary, as a classical computer would require an amount of resources exponential in the size of the simulated system. David Deutsch [35, 36] refined this idea into that of the *quantum computer*: a collection of quantum bits (quantum two-level systems that can be entangled with one another) and quantum gates (unitary operations) acting on these qubits. Such a device is not only capable of universal computation, but can be more powerful than any classical computer. A striking demonstration of this fact came with the discovery of Shor's algorithm [134], which gives an exponential speedup to factorization of composite numbers [1]. These theoretical developments have led to a large experimental effort to build a quantum computer. DiVincenzo listed the criteria that would be needed for such a machine [43]:

1. A scalable physical system with well-characterized qubits

2. The ability to initialize the state of the qubits to a simple state

3. Long decoherence times, much longer than the gate operation time

4. A universal set of quantum gates

5. A qubit-specific measurement capability

---

[1]That many encryption algorithms rely on the difficulty of the factoring problem, and so could be broken by Shor's algorithm, has not escaped the intelligence community. This fact has driven much of the interest in, and consequently the funding for quantum computing research. It is clear, at least, that the National Security Agency believes that quantum computers will one day be built, recently encouraging end users to migrate to forms of encryption resistant to attack by quantum techniques [80].

While there are many possible physical systems in which these requirements can be satisfied, this thesis will focus on quantum circuits built out of superconducting elements [38, 39]. More specifically, the focus will be on criterion 5: the readout of superconducting qubits.

1.1.1 The Quantum Bit
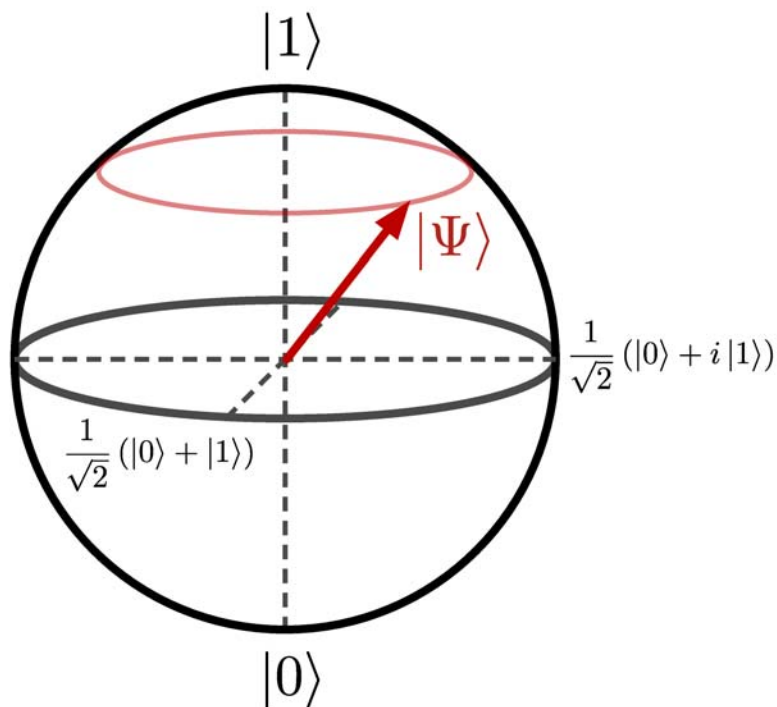
Figure 1.1: Representation of a qubit wavefunction $|\Psi\rangle$ as a vector on the surface of the Bloch sphere. A state is characterized by two complex amplitudes, or the two polar angles: $|\Psi\rangle = \cos\theta |0\rangle + e^{i\psi} \sin\theta |1\rangle$.

A computer is a device which performs logical operations on memory. For a classical digital computer, this memory is comprised of 'bits', which can take one

of two values: 0 or 1. In a quantum computer, the analog of a bit is a 'qubit': a quantum system with two states, typically denoted $|0\rangle$ and $|1\rangle$. The qubit can then be in any superposition state, with a wavefunction: $|\Psi\rangle = a_0 |0\rangle + a_1 |1\rangle$, with $|a_0|^2$ and $|a_1|^2$ the probability of measuring the qubit in either state. The state of the qubit is represented as a point on the surface of the Block sphere, as shown in Figure 1.1. $|\Psi\rangle$ is represented as a vector on the unit sphere, with $|0\rangle$ at the south pole and $|1\rangle$ at the north pole. The unitary operations that the quantum computer will perform on the qubit then become rotations of the vector on the Bloch sphere.

Any two level system found in nature can in principle be used as a qubit, with the standard example being the two spin states of an electron in a magnetic field. Much of the difficulty in making a qubit practical for quantum computation lies in creating a system that is strongly coupled to the environment so that it can be controlled and measured, but not so strongly coupled that the interaction with the environment leads to excessive decoherence, destroying the quantum state. There is active research on many different physical realizations of qubits: spins on quantum dots [94], Rydberg atoms [126], and NV centers in diamond [151], to name just a few. While every architecture presents tradeoffs, superconducting qubits have many advantages, and there has been tremendous experimental progress in the last two decades.

1.1.2 Superconducting Qubits

Superconducting qubits exploit the remarkable fact that superconductors show quantum behavior at macroscopic scales. We can use this to build the qubits from

electrical circuits designed to have anharmonic spectra. The lowest two energy levels of the oscillator can then be used as the computational $|0\rangle$ and $|1\rangle$ states. While we defer a more detailed description of the physics of superconducting qubits to Chapter 2, all such qubits share a common element: a resonator with a nonlinear inductance. Conveniently, this circuit element can be made with a Josephson junction: two superconductors separated by a weak link, often a thin metal oxide.

This approach offers many benefits. The qubits can be made from superconductors microfabricated using traditional thin film processing techniques, and their macroscopic size makes them easy to model using standard integrated circuit simulation tools. The energy scale is at microwave frequencies, and the impedance [38] of the circuit is close to the 50Ω standard of electrical engineering. This tight coupling to the control leads allows for fast gate operations on the qubit, but comes at a cost: significant decoherence due to environmental noise sources. Much of the progress in the field has been due to an assault against these sources of noise. For example, materials research has cleaned up defects in the junction barrier [100], reduced loss due to dielectrics and the superconductor-substrate interface [98, 118, 42], and continues to search for the source of $1/f$ magnetic flux noise [12]. Along with clever circuit engineering to decouple the qubit and heavy filtering on control lines, qubit lifetime has improved from sub-nanosecond in 1999 [110] to in excess of 50 μs in transmon qubits today [124].

1.1.3 Scaling Up

The long coherence time demonstrated by these circuits, as well as the development of high-fidelity single and two qubit gates, has made it possible to construct small-scale quantum "processors" that can perform coherent operation on several qubits (for example, [156, 9]). However, individual qubits and gates are still far from the threshold required to build a *useful* quantum computer that could run an interesting algorithm. Quantum algorithms are based on the manipulation of large entangled states of many qubits, so even extremely small error rates can accumulate and render the calculation useless. Rather than trying to use physical qubits with potentially impossible perfection, it seems likely that a quantum computer will need to use a quantum version of error correction [119]. There are many possible implementations [106, 55, 78, 75], but all of them trade reduced demands on qubit and gate fidelities for increased physical and algorithmic complexity. The quantum information is stored in logical qubits, groups of many physical qubits. Recently, small circuits that can correct for bit-flip errors [77] and bit and phase-flip errors [33] have been experimentally demonstrated. One implementation that has received considerable recent attention is the surface code [47]. Implemented as a two-dimensional mesh of qubits, it requires only nearest-neighbor qubit-qubit couplings, and can accommodate error rates at the 1% level. The large number of qubits required to implement this form of error correction is a significant hurdle: one design [46] for a computer able to factor a large semi-prime number estimates that it will need millions of physical qubits to function. Even for a smaller system with a more modest number of qubits, a key challenge is the need to measure the

state of many qubits at each step of the algorithm to detect and correct for errors. As the superconducting quantum information field looks towards ever larger systems, it is becoming increasingly urgent to design readout schemes that will scale with the size of our devices. The next few sections will look at one readout technique that offers many interesting possibilities: circuit quantum electrodynamics (circuit QED).

1.2   Circuit QED
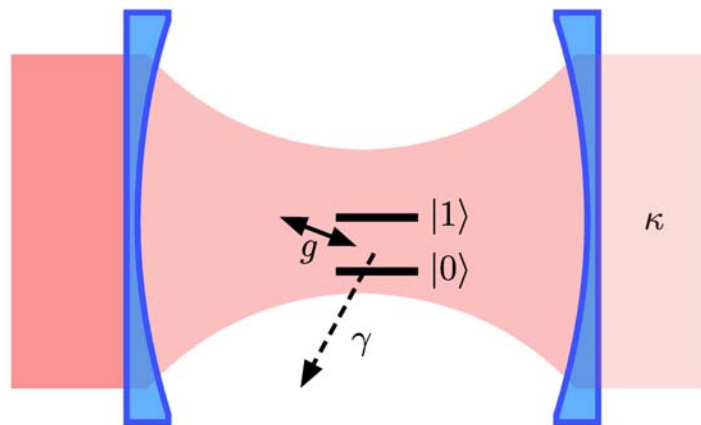
Figure 1.2: Cavity QED scheme. An atom with two energy levels interacts with light trapped in an optical cavity with strength g. Main sources of dissipation are from the atom coupling to other modes with rate γ or photons leaking out of the cavity at rate κ.

First developed by the Yale group [15, 131], circuit QED is a close cousin to cavity

quantum electrodynamics (cavity QED) [107, 148], an atomic physics technique used to study the interaction between electromagnetic fields and single atoms. Figure 1.2 illustrates the typical cavity QED setup. A high quality Fabry-Pérot cavity confines a single electromagnetic mode, which interacts with a single atom placed in the cavity. If the mirrors are semi-transparent, a measurement of photons leaking out of the cavity yields information about the state of the atom. In circuit QED, the optical cavity is replaced by a microwave resonant cavity and a superconducting qubit plays the role of the atom, as shown in Figure 1.3a. The cavity can be a microfabricated thin-film circuit in two-dimensional implementations, or a macroscopic microwave resonator in 3D implementations; these circuits typically operate in the C and X bands of the RF spectrum (approximately 4 to 12 GHz). By weakly coupling radiation to the cavity through small coupling capacitors, we can measure the state of the qubit by looking at its microwave transmission. In electrical engineering language, the impedance of the qubit depends on its state, and the different amounts of current flowing through the qubit to ground modify the cavity resonance.

It is instructive to write down the Hamiltonian of the coupled cavity-qubit system, the Jaynes-Cummings Hamiltonian:

$$\hat{H}_{\mathrm{JC}} = \hat{H}_{\mathrm{qb}} + \hat{H}_{\mathrm{cav}} + \hat{H}_{\mathrm{int}}$$
$$= \frac{1}{2}\hbar\omega_{10}\hat{\sigma}_z + \hbar\omega_c(\hat{a}^\dagger\hat{a} + \frac{1}{2}) + \hbar g(\hat{a}^\dagger\hat{\sigma}_- + \hat{a}\hat{\sigma}_+) \quad (1.1)$$

This is the Hamiltonian for a two-level system with energy $\hbar\omega_{10}$ coupled to a harmonic oscillator (representing the cavity) with level spacing $\hbar\omega_c$ through an
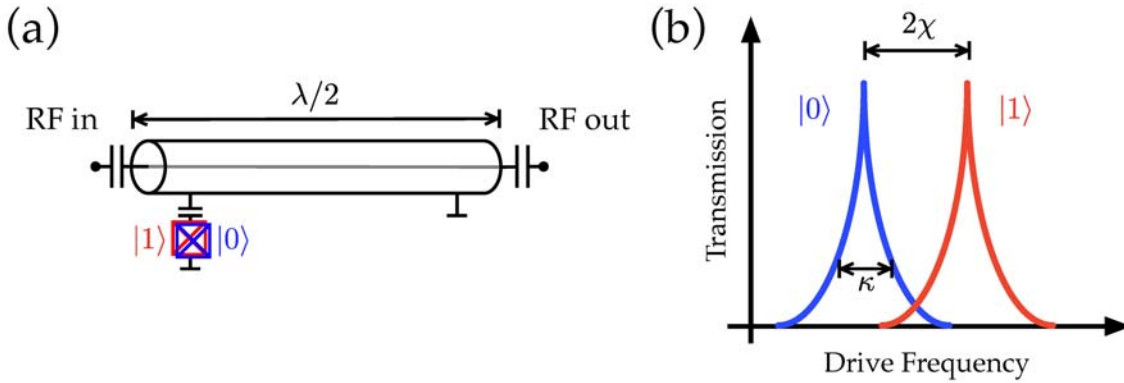
Figure 1.3: (a) Circuit QED. The qubit is capacitively coupled to a $\lambda/2$ resonator which is itself capacitively coupled to the environment. (b) Transmission through the cavity depends on the state of the qubit, with a frequency difference of 2χ between the states. The state of the qubit can be resolved in this measurement so long as $\chi > \kappa$, the linewidth of the resonator.

interaction of strength $\hbar g$. This Hamiltonian is written in the rotating wave approximation, keeping only the energy conserving terms $\hat{a}^\dagger \hat{\sigma}_-$ and $\hat{a}\hat{\sigma}_+$, which represent the transfer of energy between the cavity and the qubit. While this form can be explicitly diagonalized [146], a limit that is particularly useful for quantum information is the dispersive limit, where the cavity and qubit frequencies have a large detuning $\Delta \equiv \omega_{10} - \omega_c \gg g$. An expansion to first order in the small parameter g/Δ gives:

$$\hat{H}_{\text{disp}} = \frac{1}{2}\hbar\omega_{10}\hat{\sigma}_z + \hbar\left(\omega_c + \frac{g^2}{\Delta}\hat{\sigma}_z\right)\left(\hat{a}^\dagger\hat{a} + \frac{1}{2}\right) \tag{1.2}$$

This equation makes it easy to see that the dispersive limit can be understood in one of two equivalent ways: the cavity frequency is pulled by $\chi \equiv g^2/\Delta$ depending on the state of the qubit, or the qubit transition frequency is shifted by $2g^2/\Delta$ for each photon in the cavity. As Figure 1.3b illustrates, measuring the transmitted

signal through the cavity is a measurement of the qubit state.

1.2.1   Measurement

While the question of measurement in quantum mechanics has always been contentious, we will limit ourselves to considering it in the framework of von Neumann measurements [70]. We choose some basis over which a quantum state $|\Psi\rangle$ is defined, and perform a measurement to check which basis state the system is in. Independent of the initial state of the system, we will find it in one of the basis states of the measurement with random probability. As a concrete example, performing measurement of a qubit in the energy basis $|\Psi\rangle = a_0 |0\rangle + a_1 |1\rangle$ will collapse the wave function to either of the two eigenstates $|0\rangle$ and $|1\rangle$. By performing repeated measurements we can access $|a_0|^2$ and $|a_1|^2$.

Types of measurements which are especially important for quantum information are Quantum Non-Demolition (QND) measurements [32]. QND measurements leave the system in its measured state, making it possible to perform repeated measurements. This is possible if the observable being measured is an eigenstate of the system; mathematically, we want our measurement Hamiltonian to commute with the system Hamiltonian:

$$[\hat{H}_{\text{sys}}, \hat{H}_{\text{meas}}] = 0 \tag{1.3}$$

For a qubit, this type of measurement still probabilistically collapses the state vector onto the z-axis, but all subsequent measurements will return the same result.

Of course, information about the x and y components of the state vector is lost since σ_x and σ_y do not commute with σ_z. The ability to make consistent repeated measurements of our system is advantageous, as it allows us to turn a single weak QND measurement of the system above into a strong projective measurement through repeated measurements. The dispersive measurement discussed above is one example of this type of weak QND measurement (i.e. $[\hat{H}_{\text{disp}}, \sigma_z] = 0$).

1.2.2 Amplifier Readout

Dispersive QND measurement of a superconducting qubit has been demonstrated by many groups [66, 144, 73, 20, 147]. Experimentally, one uses a low noise amplifier and a heterodyne detection setup to monitor the phase or frequency shift through the qubit cavity. The output RF signal is modulated by the state of the qubit, so it is natural to decompose it into its two quadratures, I and Q:

$$V_{\text{out}}(t) = \text{Re}\left[I(t) + iQ(t)\right] e^{i\omega t}$$
$$= I(t)cos(\omega t) - Q(t)sin(\omega t) \tag{1.4}$$

In the complex I, Q plane, the two states of the output signal will appear as Gaussian distributions, as show in Figure 1.4. The width σ_n of these gaussians reflects the noise added to the signal by the measurement amplification chain. For a measurement with bandwidth B, and an amplifier that adds n_{add} photons of noise

to the signal, this will be :

$$\sigma_n = \sqrt{\hbar\omega(n_{\text{add}} + 1/2)Z_0 B} \tag{1.5}$$

The signal to noise ratio of the measurement will be $v_{\text{sig}}/2\sigma_n$, where v_{sig} is the voltage separating the two state gaussians. The integration time of the measurement is limited by the energy decay of the qubit (parametrized by T_1). Additionally, the measurement power is limited (although it is possible to perform readout using a strong drive in a non-QND manner [120]), since the dispersive approximation of 1.2 breaks down past a critical number of photons given by

$$n_{\text{crit}} = \frac{\Delta^2}{4g^2} \tag{1.6}$$

Improving SNR and thus measurement fidelity for amplifier based readouts therefore requires maximizing gain while minimizing the added noise of the amplifiers. However, all linear phase-preserving amplifiers must add at least a half-quantum of noise to the signal [27]. This is often referred to as the standard quantum limit (SQL). When cascading amplifiers, the noise of the first amplification stage is the dominant contribution for sufficiently large gain [116], so there has been considerable effort spent developing quantum-limited amplifiers for qubit readout. Fortunately, the physics of Josephson junctions offers many ways to realize quantum-limited or near quantum-limited amplifiers.

A popular approach relies on parametric amplification of the signal using a strongly driven nonlinear resonator incorporating a Josephson junction. Known as
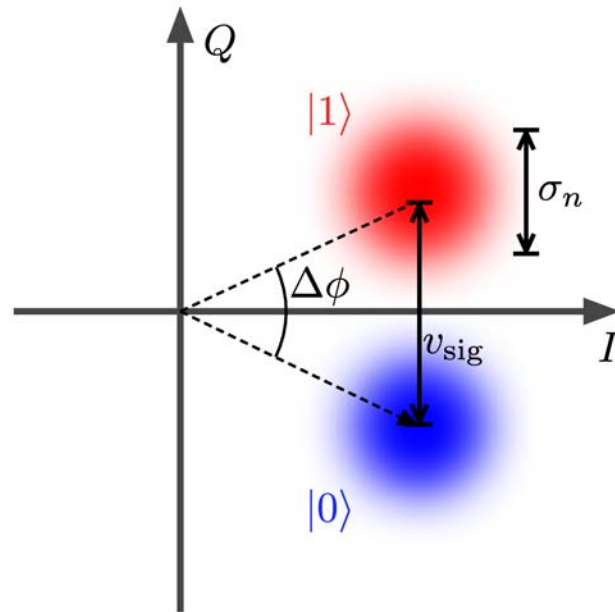
Figure 1.4: Schematic of the readout signal in the complex I, Q plane using a good amplifier. The two cavity states are gaussian distributions with width σ_n, separated by v_{sig}.

Josephson parametric amplifiers (JPAs), these devices have become a mainstay of superconducting qubit experiments. Despite offering very high gain (often in excess of 30 dB) and truly quantum-limited performance, their narrow bandwidth and low saturation power are challenging for experiments which require the readout of multiple qubits simultaneously through frequency multiplexing. They are slowly being replaced by parametric amplifiers which use traveling wave structures to perform parametric amplification. This can be implemented either with chains of Josephson junctions forming a transmission line in the traveling wave parametric amplifier (TWPA) [159, 157, 96], or with extremely long kinetic inductors [62]. These amplifiers have demonstrated extremely high bandwidth, gain and saturation

power while being within a factor of two of the standard quantum limit. A different approach has relied on voltage-state superconducting quantum interference device (SQUID) based amplifiers.x The most successful of these is the superconducting low inductance galvanometer (SLUG) amplifier [122, 65, 66], which not only is near quantum-limited over an instantaneous bandwidth of a few hundred megahertz, but also provides some intrinsic non-reciprocity, protecting the qubit from noise from later gain stages.

While these amplifiers have been used in impressive experiments on single qubits, such as quantum feedback stabilization of Rabi oscillations [143], and have been a key enabler for the small-scale demonstrations of error correction mentioned above, there remain significant challenges to their scalability. Parametric amplifiers require large pump tones which must be isolated from the qubit using one or more microwave circulators, which is problematic as circulators are bulky and rely on magnetic fields to generate the needed non-reciprocity. The SLUG amplifier does not need a pump tone to provide gain, and it offers intrinsic non-reciprocity [64], but it is a hot voltage state device[2] and has not yet shown performance comparable to the paramps. Amplifiers are also expensive in terms of physical size and device complexity, and even today we are reaching the limits on the number of microwave lines that can be routed to the cold stage of a dilution refrigerator.

---

[2]The SLUG operates with $I_b > I_c$ and therefore dissipates power in the resistors that shunt the SQUID loop[66].

1.2.3 Photon Counting

Can we implement qubit readout in a more simple and scalable way? One potential solution is to replace amplifier-based readout, which corresponds to measuring the qubit cavity field amplitude $\hat{a} + \hat{a}^\dagger$ with a device that can measure the photon occupation of the cavity $\hat{a}^\dagger \hat{a}$. While in principle a single photon contains enough information to determine the qubit state, photon detection at microwave frequencies has been a formidable challenge. Optical photon counters rely on a metal with a work function small enough that an incident photon will create a photoelectron that can then be multiplied in order to generate a large signal. This approach is doomed to failure for microwaves as photon energies are far too small: 5 GHz corresponds to an energy of only 20 μeV, tens of thousands of times smaller than typical work functions.

Despite this, photon counting is an attractive technique for qubit readout in circuit QED systems if a few requirements are met. The photon detecting circuit should be as small and simple as possible, allowing tight integration with the quantum system and readout of a large number of qubits. The counter should provide a large and easily measurable classical signal in order to minimize the physical overhead of the readout. Finally, we would like to build the photon counter using the standard building blocks of superconducting electronics: Josephson junctions. The first proposal for such a circuit, using current-biased junctions, was made by Romero *et al.* in 2009 [125]. In 2011, Chen *et al.* [28] implemented this type of photon counter, naming them Josephson Photomultipliers (JPMs), and used them to measure non-classical correlations in the arrival times of microwave photons

emitted from a thermal source. This thesis describes our results on perfecting the JPM and using it to read out a transmon qubit.

2   QUANTUM ELECTRONICS

It should not be surprising that to build superconducting quantum computers we need to consider the quantum dynamics of electrical circuits. A circuit is completely described by the voltages at its nodes, the currents flowing through its branches, and the topology of their connections. These voltages and currents (or equivalently, charges and fluxes) can be taken as the generalized coordinates of the system, playing the roles of particle positions and velocities in classical mechanics. The equations of motion of the circuit can then be computed by using a Lagrangian or Hamiltonian approach. This is a powerful technique[1] that also presents us with the opportunity to quantize electrical circuits by straightforwardly copying the way in which we quantize systems from classical mechanics. For a more in depth discussion on this approach than offered here, the reader is referred to the work of Devoret [37] and Yurke and Denker [162].

This use of quantum mechanics is different from its usual realm of applicability: instead of describing microscopic particles, we are studying macroscopic circuit elements. The quantum mechanical approach to circuit theory does not describe the dynamics of individual particles, but that of collective degrees of freedom which can exhibit quantum properties. For macroscopic quantum dynamics to become relevant, the system should be sufficiently well isolated such that the spacing between energy levels is much larger than thermal fluctuations and much larger than their width. Thinking of a microwave LC oscillator with a resonant frequency

---

[1]And can be even further generalized by considering circuits as networks using category theory, see [5].

$\omega_0/2\pi \sim 5\,\text{GHz}$, we want $\hbar\omega_0 \gg k_B T$ and a quality factor $Q \gg 1$. Practically, this means temperatures on the order of a few tens of millikelvins or less and circuits with very low dissipation, which can both be realized by building circuits out of superconducting elements.

2.1 Quantizing Circuits

The formal approach to quantizing a lumped-element superconducting circuit is to write down the classical circuit Hamiltonian (or Lagrangian), and replace the classical variables with quantum-mechanical operators. In order to do so, we must settle on a convenient set of variables to describe the circuit; a good choice is to use the charge Q and magnetic flux Φ stored by circuit elements. We define the flux as:

$$\Phi(t) = \int_{-\infty}^{t} V(t')dt' \tag{2.1}$$

where $V(t)$ is the voltage across the circuit element. When we promote q and Φ to quantum variables, we need only replace them with operators $\hat{q}$ and $\hat{\Phi}$, which satisfy the canonical commutation relation:

$$[\hat{\Phi}, \hat{q}] = i\hbar \tag{2.2}$$

From standard circuit theory, we can then write the energy stored in capacitors and inductors [2]:

$$E_C = \frac{1}{2}CV^2 = \frac{q^2}{2C} \tag{2.3}$$

$$E_L = \frac{1}{2}LI^2 = \frac{\Phi^2}{2L} \tag{2.4}$$

2.1.1 Quantum LC Oscillator
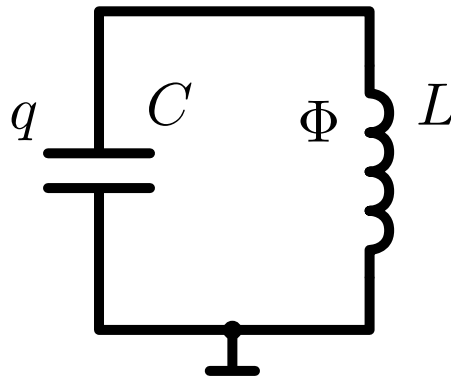
Figure 2.1: An LC oscillator circuit.

As a concrete example, we consider the quantum mechanics of a simple parallel LC oscillator, as seen in Figure 2.1. In this two-node circuit, we only need to consider charges and fluxes at one node, since the other is grounded. The equation of motion of the circuit is derived by equating the current flowing from the inductive element

---

[2]Of course, this whole formalism can be extended to cover dissipative elements such as resistors. This is straightforward in the classical case, see [152] for details. The quantum formulation requires much more care; an overview can be found in [95]. The standard approach, due to Caldiera and Leggett [24], is to model a resistance as an infinite bath of parallel LC oscillators. The general study of such open quantum systems remains an area of active research.

to that flowing to the capacitor:

$$\frac{\Phi}{L} = -C\frac{d^2\Phi}{dt^2} \tag{2.5}$$

Noting the obvious similarity to Newton's equation of motion for a particle moving in a potential $\Phi^2/2L$, the Lagrangian of the circuit is given by:

$$\mathcal{L} = \frac{C\dot{\Phi}^2}{2} - \frac{\Phi^2}{2L} \tag{2.6}$$

where Φ takes on the role of particle position and $\dot{\Phi}$ that of velocity. To write down the Hamiltonian we replace the latter by the conjugate momentum

$$\frac{\partial\mathcal{L}}{\partial\dot{\Phi}} = C\dot{\Phi} \equiv q \tag{2.7}$$

and use the Legendre transform to calculate:

$$H = \dot{\Phi}q - \mathcal{L} = \frac{q^2}{2C} + \frac{\Phi^2}{2L} \tag{2.8}$$

Following the standard treatment of the quantum harmonic oscillator, we can introduce creation and annihilation operators which satisfy $[\hat{a}, \hat{a}^\dagger] = 1$:

$$\hat{\Phi} = \sqrt{\frac{\hbar Z_0}{2}}(\hat{a} + \hat{a}^\dagger) \tag{2.9}$$

$$\hat{q} = -i\sqrt{\frac{\hbar}{2Z_0}}(\hat{a} - \hat{a}^\dagger) \tag{2.10}$$

where $Z_0 = \sqrt{L/C}$ is the characteristic impedance of the oscillator. Substituting

these into Equation 2.8, we finally arrive at a Hamiltonian that takes a very familiar form:

$$\hat{H} = \hbar\omega\left(\hat{a}^\dagger\hat{a} + \frac{1}{2}\right) \tag{2.11}$$

While this is not a particularly surprising result given the simple circuit we started with, this procedure is general and can be used to derive the Hamiltonian of much more complicated devices.

2.2 Superconducting Circuits

The modern microscopic theory of superconductivity was developed by Bardeen, Cooper and Schrieffer in their Nobel-prize winning 1957 work [7]. Below a critical temperature T_c, some metals undergo a phase transition when the interaction between electrons near the Fermi surface becomes attractive. This attractive potential, resulting from the coupling of electrons to lattice phonons, allows electrons of opposite momentum to bind into Cooper pairs. Since electrons are spin-$\frac{1}{2}$ particles, the Cooper pairs are composite bosons, and can condense into a Bose-Einstein condensate. Their overall state is then described by a single wavefunction like order parameter:

$$\Psi(\boldsymbol{r}, t) = \sqrt{n(\boldsymbol{r}, t)}e^{i\theta(\boldsymbol{r}, t)} \tag{2.12}$$

where $n(\boldsymbol{r}, t)$ is the density of Cooper pairs, and $\theta(\boldsymbol{r}, t)$ a quantum-mechanical phase.

The fact that the electronic state of a superconductor can be described by a single wavefunction, what Edward Teller called the "miracle of superconductivity", leads

to several remarkable properties. In the superconducting state, they exhibit zero DC resistance. They can also support persistent currents with no dissipation, with the lifetime of currents in superconducting rings measured to be in the billions of years [140]. Superconductors also exclude magnetic fields through the Meissner effect. This example of perfect diamagnetism forces currents in superconductors to their edges, decaying exponentially away from the surface. The characteristic length scale of this decay is the London penetration depth, λ_L. These effects allow the realization of circuits with extremely high quality factors due to negligible dissipation.

2.3 Josephson Junctions
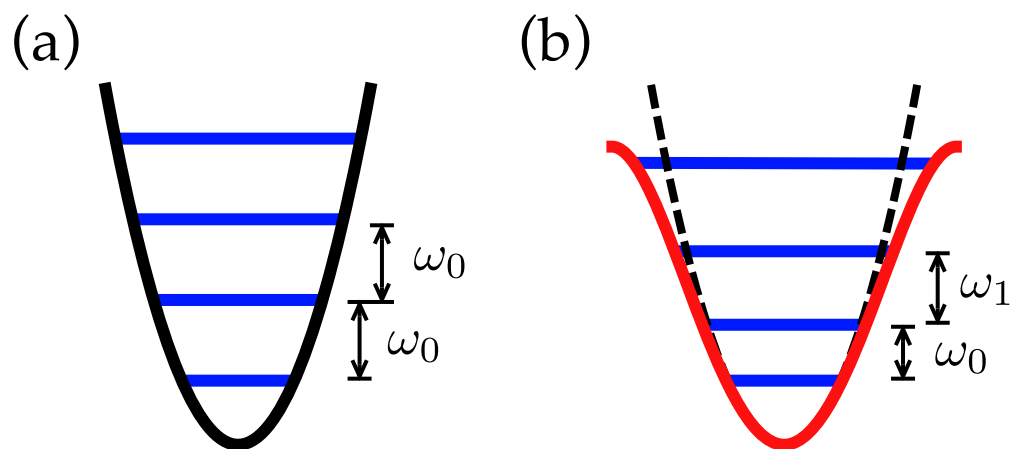
Figure 2.2: (a) Harmonic oscillator with equally spaced levels with energy $E_n = \hbar\omega_0(n + 1/2)$. (b) Anharmonic oscillator with $\omega_0 < \omega_1 < \ldots$

Superconducting quantum circuits built out of only linear elements would be interesting, but not useful as quantum bits. The reason is simple: the energy levels

of a quantum harmonic oscillator, such as that described subsection 2.1.1, all have the same spacing ω_0 as shown in Figure 2.2a. An individual transition cannot be addressed since all transitions have the same energy, and applying a drive at frequency ω_0 will result in a superposition of many states (in fact, a coherent state). If the system has some nonlinearity, however, the resulting potential (Figure 2.2b) has unequally spaced energy levels and it becomes possible to address individual transitions. Typically, the two states (cf. Section 1.1.1) of superconducting qubits are chosen to be the lowest two states of such an anharmonic potential.
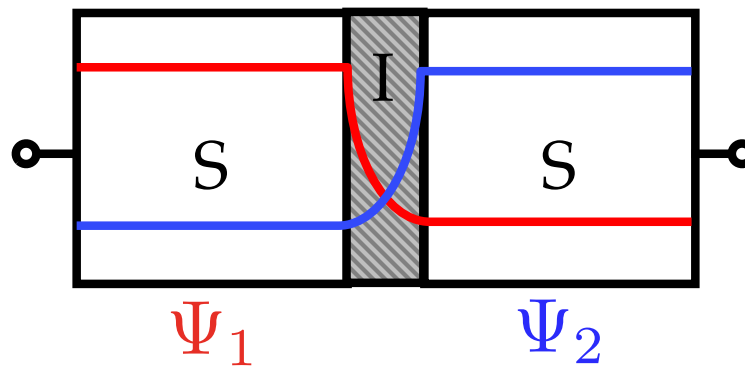
Figure 2.3: SIS Josephson junction, formed by two superconductors (S) separated by a thin insulating barrier (I), typically an oxide. The amplitude of the wavefunctions Ψ_1 and Ψ_2 of the condensate in each superconductor is represented by the red and blue lines, showing how Cooper pairs can tunnel across the barrier.

Fortunately, superconductors provide us with the only known nonlinear, non-dissipative element, the Josephson junction (JJ). As shown in Figure 2.3, a Josephson junction is formed by two superconducting electrodes separated by a thin barrier. Most commonly this barrier is a thin metal oxide, such as aluminum oxide, but it can also be formed by a constriction in the size of the superconductor. If the barrier is sufficiently thin, there is an appreciable probability for electrons to tunnel across

it, leading to a current flowing through the junction of the form [140]:

$$I = I_c \sin \delta \tag{2.13}$$

$\delta \equiv \theta_2 - \theta_1$ is the phase difference between the wavefunctions describing the superconductors on either side of the junction. The parameter I_c, known as the *critical current* of the junction, sets the maximum current that can pass through the barrier. I_c is set by the thickness and area of the barrier, the superconducting gap of the electrodes, and any magnetic field present. Additionally, the voltage across the junction is related to the phase difference by:

$$V = \frac{\Phi_0}{2\pi} \dot{\delta} \tag{2.14}$$

Where $\Phi_0 \equiv h/2e = 2.067834 \times 10^{-15}$ Wb is the magnetic flux quantum. Taken together these two equations, known as the Josephson relations, imply two effects: a DC current will flow across the junction even in the absence of a voltage, and an AC current will appear across a DC voltage biased junction at a frequency $f = V_{\mathrm{DC}}/\Phi_0$.

A Josephson junction is a nonlinear inductance. This can be seen most easily by directly computing the inductance from the Josephson relations:

$$
\begin{aligned}
L_J &= V \left(\frac{\partial I}{\partial t} \right)^{-1} \\
&= \frac{\Phi_0 \dot{\delta}}{2\pi} \frac{1}{I_c \dot{\delta} \cos \delta} \\
&= \frac{\Phi_0}{2\pi I_c \cos \delta} = \frac{L_J(0)}{\cos \delta}
\end{aligned}
\tag{2.15}
$$

The inductance depends nonlinearly on the phase across the junction and can in fact diverge. $L_J(0)$ is the zero-flux inductance and is referred to as the Josephson inductance of the junction. The potential energy of the junction can also be computed:

$$
\begin{aligned}
U &= \int_0^t IV\,dt \\
&= \frac{\Phi_0}{2\pi} \int_0^\delta I_c \sin(\delta)d\delta \\
&= \frac{\Phi_0 I_c}{2\pi}(1 - \cos \delta)
\end{aligned}
\tag{2.16}
$$

The energy scale of the junction potential is set by $E_J \equiv \Phi_0 I_c/2\pi$, the Josephson energy. It is this nonlinear potential that is at the heart of experimental implementations of superconducting qubits.

2.3.1   Current-Voltage Characteristics

Figure 2.4a shows the current-voltage characteristic of an undamped Josephson junction. For applied currents less than the critical current, the junction is in the *supercurrent* state, with no voltage developing across the junction. When the bias current exceeds the critical current, the junction switches to the *normal* state, where a voltage can develop across it. When this voltage exceeds the superconducting gap voltage $V_g = 2\Delta/e$ there is sufficient energy to break apart Cooper pairs and the IV characteristic approaches that of a resistor. The tunneling resistance at a
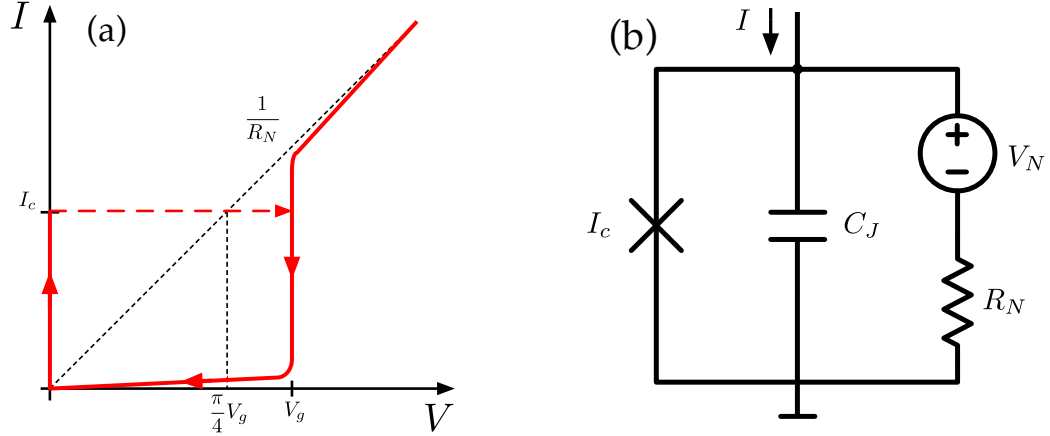
Figure 2.4: (a) Undamped Josephson junction IV curve, showing supercurrent and normal branches; the dashed arrow indicates the junction switching between these two branches as the current is increased past the critical current I_c. The junction has normal state resistance R_N, and gap voltage $V_g = 2\Delta/e$. The Ambegaokar-Baratoff relation is also represented. (b) RCSJ model equivalent circuit for a Josephson junction of critical current I_c, self-capacitance C_J, and normal state resistance R_N, which can either be a real external resistance or a representation of the junction's intrinsic normal state conductance. V_N is the noise voltage that develops across this resistance, useful in modeling the noise properties of junction-based circuits [122].

temperature T is given by the Ambegaokar-Baratoff relation [2, 141]:

$$R_N = \frac{\pi V_g}{4 I_c} \tanh\left(\frac{\Delta}{2 k_b T}\right) \tag{2.17}$$

The tunneling resistance R_N is exactly the normal state resistance of the junction. This makes it possible to estimate the critical current of a junction with a room-temperature measurement of its resistance using a four-wire probe station.

2.3.2 The RCSJ Model

A useful semi-classical model of the Josephson junction is the RCSJ model whose equivalent circuit pictured in Figure 2.4b. The junction is modeled as three components in parallel: a supercurrent obeying the first Josephson relation 2.13, a capacitance, and a resistance. The capacitance represents the self-capacitance of the junction electrodes; in this thesis, we assume a value of 50 fF/μm^2. The resistance can represent either quasiparticle tunneling as given by 2.17 or a physical external shunt resistance. Setting equal the external bias current I_b to the total current flowing through the junction, we write:

$$I_b = I_c \sin(\delta) + \frac{\Phi_0}{2\pi R_N}\dot{\delta} + C_J\frac{\Phi_0}{2\pi}\ddot{\delta} - \frac{V_N}{R_N} \tag{2.18}$$

where $V_N = \sqrt{4k_b T R_N}$ is the Johnson-Nyquist voltage noise across the resistor [122, 32][3]. Dropping the noise voltage term, this equation can be rearranged to yield an equation of motion for δ:

$$\ddot{\delta} = -\frac{1}{M}\frac{dU(\delta)}{dt} - \frac{\dot{\delta}}{R_N C_J} \tag{2.19}$$

Where we have defined $M = C(\Phi_0/2\pi)^2$ and the current biased junction potential energy is:

$$U(\delta) = -\frac{\Phi_0 I_c}{2\pi}\left(\cos(\delta) + \frac{I_b}{I_0}\delta\right) \tag{2.20}$$

---

[3]At low temeperatures, the true spectral density of the noise is quantum and has spectral density $S(\omega) \propto \omega$. [122]

The current biased JJ potential $U(\delta)$, plotted in Figure 2.5 is often known as the *tilted washboard* potential, due to its shape. It is a quasi-periodic potential whose overall slope is controlled by the normalized bias current $i_b \equiv I_b/I_c$, and whose minima are located at

$$\delta_0 = \arcsin(i_b) + 2\pi n, \qquad n \in \mathbb{Z} \tag{2.21}$$

The dynamics of the junction can be understood with a mechanical analogy: the
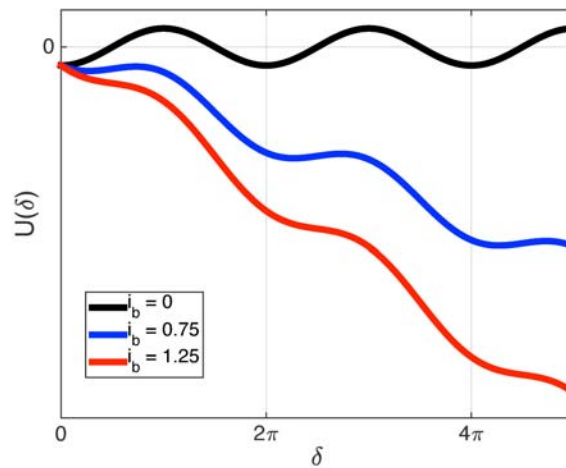
Figure 2.5: The tilted washboard potential of a current-biased Josephson junction, plotted for three different values of the reduced current bias $i_b \equiv I_b/I_c$.

phase can be thought of as a particle of mass M moving in the potential of Equation 2.20. As i_b is increased, the potential energy barrier at the minimum is reduced (vanishing when $i_b = 1$) and the particle can freely slide down the potential, accumulating phase at a finite voltage $V = \dot{\delta} \neq 0$. In the supercurrent state, the phase particle is trapped at a potential energy minimum and $\dot{\delta} = 0$. Damping in the junction acts like a drag force proportional to $1/R_N C_J$, and in its absence the junction will not retrap at a potential minimum until the bias current is returned

to $i_b = 0$. We can expand $U(\delta)$ around its minimum to get the small oscillation frequency of the junction phase in the supercurrent state:

$$\omega_p = 2^{1/4} \sqrt{\frac{2\pi I_c}{\Phi_0 C_J}} (1 - i_b)^{1/4} \tag{2.22}$$

This frequency, known as the *plasma frequency* is an important parameter that sets the overall energy scale of quantum phenomena associated with this potential. We will make use of these results repeatedly, and the quantum mechanical properties (energy levels, tunneling rates, etc...) of this potential are considered in detail in Appendix A.

Beyond developing an intuitive understanding of the dynamics of a junction, the RCSJ model is invaluable in modeling the dynamics of Josephson devices. For example, in [122] we use this model to write down the equation of motion for the two junction phases in a SLUG amplifier, and solve these equations numerically to investigate the gain, bandwidth and noise of this class of devices.
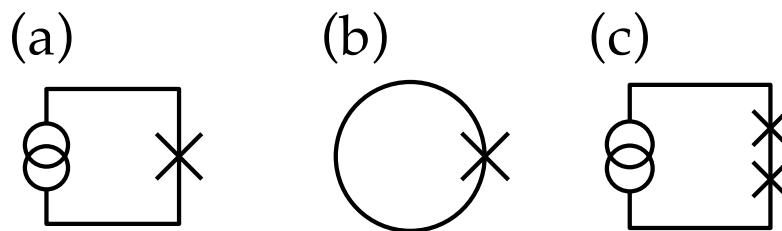
Figure 2.6: Schematic circuit diagrams of the three main qubit types: (a) phase qubit, (b) flux qubit, or (c) charge qubit

2.4   Superconducting Qubits

Superconducting qubits are all, at their core, a nonlinear resonator whose low-energy states define the computational basis which is acted upon. In this section, we will briefly describe the various ways in which such a nonlinear resonator can be built out of superconducting linear circuit elements and Josephson junctions. They differ primarily in the topology of the circuit, which in turn determines which degree of freedom is a good quantum number of the system: charge $\hat{q}$, flux $\hat{\phi}$ or junction phase $\hat{\delta}$. Schematic diagrams of the three different qubit types are shown in Figure 2.6. For a more thorough look at the different experimental possibilities, the reader is urged to consult the review article by Clarke and Wilhelm [31]. We will focus in this thesis on the transmon qubit, first described by the Yale group [81], which is a refinement of the Cooper pair box (CPB) charge qubit. This is the qubit used for the experiments described in this thesis, and it is the most commonly used variant in the wider superconducting qubit community[4].

2.4.1   Cooper Pair Box

The Cooper pair box [19, 131] is a simple circuit, shown in Figure 2.7, consisting of a superconducting island connected to ground via a Josephson junction. The island can be charged by applying a voltage V_g to an electrostatic gate that is capacitively coupled to the island through a small capacitance C_g. The total capacitance of the island to ground is $C_\Sigma = C_g + C_s$, where C_s is the self-capacitance of the junction

---

[4]Although very recently flux qubits have seen renewed interest, in part due to their greater anharmonicity [71].
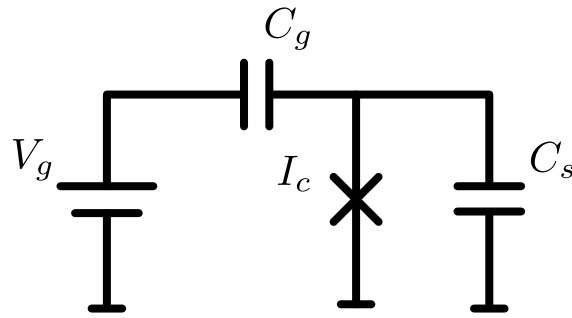
Figure 2.7: Schematic circuit of the Cooper pair box circuit. V_g and C_g are the gate voltage and capacitance, I_c is the junction critical current, and C_s is the total capacitance shunting the junction to ground, including its self-capacitance and any explicit external capacitance.

plus any extra capacitance due to the circuit configuration. At low temperatures, the only degree of freedom of this system is the number of excess Cooper pairs n on the island. We describe this quantity quantum-mechanically through the number operator $\hat{n}$, with $\hat{n}\,|n\rangle = n\,|n\rangle$. We can then write the electrostatic Hamiltonian as:

$$\hat{H}_{el} = 4E_C(\hat{n} - n_g)^2 \tag{2.23}$$

where $E_c = e^2/2C_\Sigma$ is the energy needed to add a single electron to the island and $n_g = C_g V_g/2e$ the gate-induced polarization charge (in units of Cooper pairs). The Josephson effect allows Cooper pairs to hop on and off the island, with Hamiltonian:

$$\hat{H}_J = \frac{E_J}{2} \sum_n (|n\rangle \langle n+1| + |n+1\rangle \langle n|) \tag{2.24}$$

Remembering that charge and phase are two conjugate variables (Equation 2.2), we can also write this term using Equation 2.16 and find for the total Hamiltonian:

$$\hat{H} = 4E_C(\hat{n} - n_g)^2 - E_J \cos\left(\hat{\delta}\right) \qquad (2.25)$$

Koch *et al.* [81] show how to exactly solve Schrödinger's equation for this Hamiltonian in terms of Mathieu functions. The first three eigenenergies are plotted as a function of gate charge for several values of the ratio E_J/E_C in Figure 2.8. The Cooper pair box, operating in the low E_J/E_C limit, shows a strong dependence of the transition energy E_{10} on gate charge n_g. This large charge dispersion is problematic, as the dominant dephasing mechanism is from $1/f$ noise due to local random charge fluctuations near the Cooper pair box . For this type of spectrum, the dephasing time is given by [81, 97]:

$$T_2 \sim \left|\frac{\partial E_{10}}{\partial n_g}\right|^{-1} \qquad (2.26)$$

Fortunately, the control offered by the electrostatic bias gate gives us an opportunity to reduce this charge dependence by operating at the "sweet spot" $n_g = 1/2$, where the charge dispersion goes to zero. The physical origin of this effect is easy to understand [145]: the point $n_g = 1/2$ is an avoided level crossing [5] where the ground and excited states are superpositions of the $(|0\rangle \pm |1\rangle)$ charge states. Since the two states have the same expected charge, they cannot be distinguished by a charge measurement or perturbed by charge noise. Biasing at this point leads

---

[5]The degeneracy is lifted by the presence of the junction.

to a significant improvement in qubit lifetime, but is inconvenient; the transmon, described in the next section, takes a different approach to reducing the CPBs sensitivity to this type of noise.
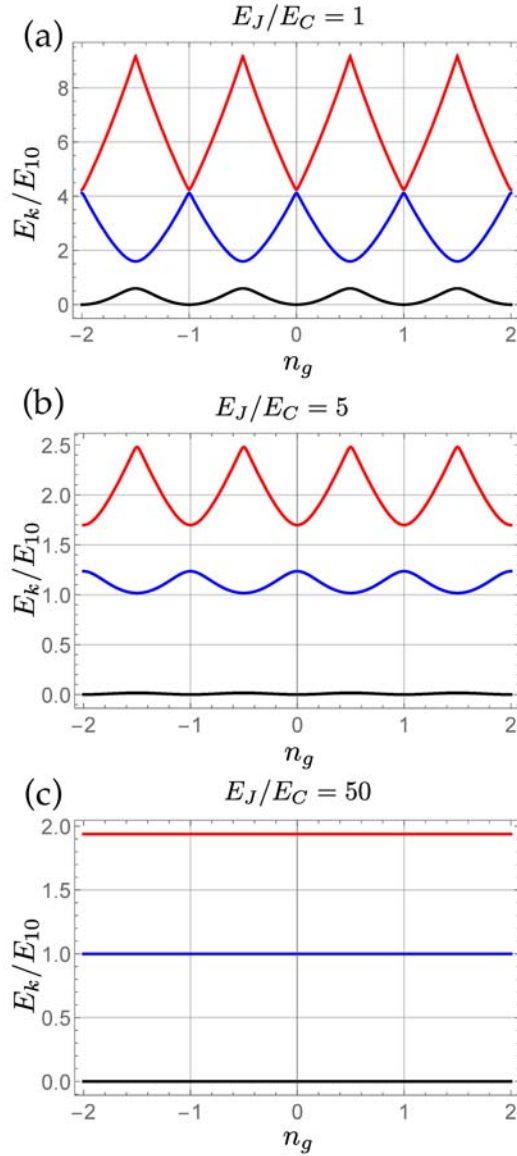
Figure 2.8: Energies E_k of the first three ($k = 0$, black, $k = 1$, blue, $k = 2$, red) eigenstates of the cooper pair box Hamiltonian for (a) $E_J/E_C = 1$, (b) $E_J/E_C = 5$ and (c) $E_J/E_C = 50$. The energies are normalized to E_{01}, the transition energy evaluated at the gate charge degeneracy point $n_g = 1/2$, and the zero point is chosen as the minimum of the $k = 0$ level. The transmon qubit operates in the $E_J/E_C \gg 1$ limit.

2.4.2 Transmon

The transmon qubit, or *transmission-line shunted plasma oscillation qubit*, first de-
scribed in [81], is a CPB operated in the regime where $E_J/E_C \gg 1$. Experimentally,
this is typically accomplished by shunting the junction in the circuit with a large
external capacitance. The advantage of this regime is obvious from Figure 2.8: the
charge dispersion is almost completely suppressed. This comes, however, at a cost:
the anharmonicity $\alpha \equiv E_{21} - E_{10}$ is also reduced. This could be problematic, as a
large anharmonicity is required in order for the first two qubit states to be selectively
addressed. However, a remarkable fact makes the transmon possible: while the
charge dispersion reduces exponentially, the anharmonicity is only suppressed
algebraically, and a trade-off can be made between the two. Koch *et al.* [81] show
that in the large E_J/E_C limit the cosine term in Equation 2.25 can be expanded,
and a perturbation analysis yields the following expression for the transmon level
energies:

$$E_k \approx -E_J + \sqrt{8E_C E_J}\left(k + \frac{1}{2}\right) - \frac{E_C}{4}(2k^2 + 2k + 1) \qquad (2.27)$$

The anharmonicity is given by $\alpha = -E_C$. For typical parameters such that $\omega_{10}/2\pi \sim$
$5\,\mathrm{GHz}$, the anharmonicity is $\alpha \sim 300\,\mathrm{MHz}$. Using qubit rotation pulses longer
than $1/\alpha \sim 3\,\mathrm{ns}$ in order to prevent spectral leakage at ω_{21} allows for many tens or
hundreds of coherent operations over a qubit lifetime.

As the name hints, the transmon is embedded in a transmission line, which
allows for both control of the qubit and state readout. This is, of course, exactly
the circuit QED scheme described in section 1.2. The transmon can be thought of

as having an effective dipole moment, and to maximize coupling it is placed at the voltage antinode of a microwave resonator. The Hamiltonian for this system is given by [15, 81]:

$$\hat{H} = 4E_C \left(\hat{n} - n_g\right)^2 - E_J \cos\hat{\delta} + \hbar\omega_r \hat{a}^\dagger \hat{a} + 2\beta e V_{\text{rms}}^0 \hat{n}(\hat{a} + \hat{a}^\dagger) \tag{2.28}$$

Here, $\omega_r = 1/\sqrt{L_r C_r}$ denotes the resonator frequency of the mode that has an antinode at the transmon's location, and $\{\hat{a}, \hat{a}^\dagger\}$ are the usual creation and annihilation operators for photons on the resonator. $V_{\text{rms}}^0 = \sqrt{\hbar\omega_r/2C_r}$ is the root-mean square voltage on the transmission line, and $\beta = C_g/C_\Sigma$ is the ratio of the coupling capacitance to the total capacitance. By re-writing this Hamiltonian in terms of the uncoupled transmon states $|j\rangle$, Koch *et al.* derive the generalized Jaynes-Cummings hamiltonian (cf. Equation 1.1) for the transmon:

$$\hat{H} = \hbar \sum_j \omega_j |j\rangle\langle j| + \hbar\omega_r \hat{a}^\dagger \hat{a} + \hbar \sum_{i,j} g_{ij} |i\rangle\langle j| (\hat{a} + \hat{a}^\dagger) \tag{2.29}$$

with couplings

$$\hbar g_{ij} = 2\beta e V_{\text{rms}}^0 \langle i|\hat{n}|j\rangle \tag{2.30}$$

In the large E_J/E_C limit, the coupling constants for neighboring states are well approximated by:

$$\hbar g_{j+1,j} \approx 2\beta e V_{\text{rms}}^0 \sqrt{\frac{j+1}{2}} \left(\frac{E_J}{8E_C}\right)^{1/4} = \sqrt{j+1}\,g_{10} \tag{2.31}$$

Furthermore, the coupling between non-neighboring states vanishes:

$$g_{j+k,j} = 0 \qquad \text{for} \qquad |k| > 1 \tag{2.32}$$

Split Junction Transmon
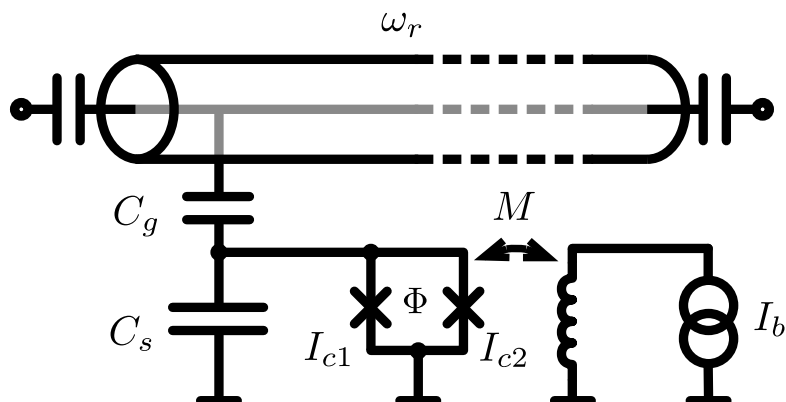
Figure 2.9: Circuit schematic for a transmon with split junctions allowing for a flux-tunable transmon energy. The two junctions with critical currents I_{c1} and I_{c2} are shunted with capacitance C_s to ground, and the superconducting island is coupled to a transmission line resonator with frequency ω_r with a coupling capacitor C_g. The flux Φ threading the junction SQUID loop can be modulated using a bias inductor with mutual M. This inductance can be either a macroscopic bias coil, or microfabricated on chip.

It is convenient to be able to tune the transition energy of the transmon qubit; the easiest way to accomplish this is to split the single junction of the Cooper pair box into a pair of parallel junctions [81, 64]. This creates the SQUID-like geometry shown in Figure 2.9, which allows an external bias inductance to control the total flux Φ through the ring formed by the two JJs. The two junctions will not necessarily

have the same critical current, and we denote the junction asymmetry as:

$$d = \frac{E_{J2} - E_{J1}}{E_{J2} + E_{J1}} \tag{2.33}$$

The flux quantization condition then allows us to rewrite the junction energy term in Equation 2.25 by making the substitution [81]:

$$E_J \to (E_{J1} + E_{J2}) cos\left(\frac{\pi\Phi}{\Phi_0}\right) \sqrt{1 + d^2 \tan^2\left(\frac{\pi\Phi}{\Phi_0}\right)} \tag{2.34}$$

Beyond an ability to tune the transmon energy spectrum, a split junction design offers a few other advantages. As demonstrated by Strand *et al.* [137], the extra degree of freedom allows for swapping of excitations between the qubit and resonator by modulating the external flux at the qubit-resonator detuning. Intentionally introducing an asymmetry in the critical currents of the two junctions can also reduce sensitivity to flux noise by reducing $\partial E_{10}/\partial\Phi$ [81, 67].

2.4.3 Transmon Readout

Of course, one of the main advantages of the transmon qubit is that it inherently reproduces the circuit QED architecture in superconducting electronics. The attached resonator enables both control of the qubit state using microwave pulses at the qubit transition frequency, and readout pulses that probe the cavity state [15, 81]. For quantum information, the transmon is operated in the so-called *dispersive* regime [15, 81, 16, 17], where the qubit-cavity detuning $\Delta = \omega_{10} - \omega_r$ satisfies $g_{01}/\Delta_0 \ll 1$. For simplicity, we rewrite the Jaynes-Cummings Hamiltonian of

Equation 2.29 as:

$$\hat{H}_{JC} = \hbar\omega_r \hat{a}^\dagger \hat{a} + \hbar\omega_{10}\frac{\hat{\sigma}_z}{2} + \hbar g \hat{I}_+ \tag{2.35}$$

where

$$\hat{I}_\pm = \hat{a}^\dagger \hat{\sigma}_- \pm \hat{a}\hat{\sigma}_+ \tag{2.36}$$

Since we are in the dispersive limit, we can use the small parameter $\lambda = g/\Delta$ to approximately diagonalize $\hat{H}_{JC}$ using the unitary transformation [16]:

$$\hat{V} = e^{\lambda \hat{I}_-} \tag{2.37}$$

Applying this transformation, we obtain the effective Hamiltonian for the dispersive regime:

$$
\begin{aligned}
\hat{H}_{eff} &= \hat{V}^\dagger \hat{H}_{JC} \hat{V} \\
&= \hbar\omega_r \hat{a}^\dagger \hat{a} + \left(\hbar\omega_{10} + 2g\lambda \left(\hat{a}^\dagger \hat{a} + \frac{1}{2} \right) \right) \frac{\hat{\sigma}_z}{2} + +\mathcal{O}(\lambda^2) \\
&= \hbar\omega_{10}\frac{\hat{\sigma}_z}{2} + (\hbar\omega_r + \hbar\chi\hat{\sigma}_z)\,\hat{a}^\dagger \hat{a} + \mathcal{O}(\lambda^2)
\end{aligned}
\tag{2.38}
$$

where cavity shift is $\chi = g^2/\Delta$. This linear approximation to the dispersive regime breaks down past the critical photon number $n_{crit} = 1/4\lambda$.

Because of the state-dependent cavity pull, a coherent drive near the cavity frequency will displace the resonator's state from vacuum to a final coherent state $|\alpha_{1,0}\rangle$. The goal of the readout circuitry is then to distinguish between these two states, usually through some form of homodyne detection, although this thesis presents an altogether different approach to readout. In [49], Gambetta *et al.* showed

that for a detector of efficiency[6] η , integration time $T_1 = 1/\gamma_1$, and resonator decay rate κ, the signal to noise ratio of the measurement is given by $\text{SNR} = \eta\kappa|\alpha_1 - \alpha_0|/\gamma_1$. The maximum value of SNR is reached for the choice $\kappa = 2\chi$, with $\text{SNR}_{max} = 4\eta\bar{n}\chi/\gamma_1$. These results are only valid for a true two-level system in the linear regime, and taking into account higher levels of the transmon and strong drive significantly modifies these expressions [13, 18]. As these effects are of great importance to a photon-counting readout, we discuss them in detail in appendix B.

---

[6]For an amplifier adding N quanta of noise to the system, $\eta \approx 1/(N+1)$ [27].

3 THE JOSEPHSON PHOTOMULTIPLIER: THEORY

The origins of the Josephson photomultiplier[1] can be found in a paper by Romero *et al.* [125] wherein they discuss several potential implementations of a microwave photon counter, including a current biased junction. This scheme was first implemented experimentally by Chen *et al.* [28] and used to study the statistics of coherent and thermal photon sources. The counter discussed in this thesis and used for qubit readout is a direct descendant of these earlier implementations.

The JPM is a conceptually simple device. At its core, it consists of a single junction that is current biased such that there are only two metastable states in the potential energy well near one of the minima of the Josephson junction potential of Figure 2.5. Since the higher energy level $|e\rangle$ is closer to the top of the barrier at the edge of the well, the rate of tunneling to the voltage continuum from this state is much larger than the ground state $|g\rangle$ tunneling rate. If the energy difference between the two states is equal to the frequency of radiation incident on the junction, there will be an enhancement in the tunneling rate corresponding to the absorption of a photon and excitation of the junction. It is this enhanced tunneling rate, and the large classical voltage pulse generated by the junction switching that acts as a photon detecting circuit. Practically, one brings the junction into resonance for a short period of time, and the presence of a switching event during the active time interval indicates the detection of a photon. Since tunneling rates are large, on the order of $1\,\mathrm{GHz}$, the active time can be as short as a few nanoseconds. These short

---

[1]The name originates with the McDermott lab, and is something of a misnomer as there is no true multiplication process like what occurs between the dynodes of an optical photomultiplier tube. It is, however, pithy and effective at conveying the purpose of the circuit.

times, as well as the inherent simplicity of the circuit make the JPM an attractive candidate for photon detection in cQED.

In this chapter, we will review the theoretical understanding of the JPM that we have achieved to this date. We will also describe how the performance of the JPM can be improved as well as benchmarked.

3.1 The Josephson Photomultiplier Concept

3.1.1 The Tilted Washboard

As discussed in the previous chapter, the potential energy of a Josephson junction of critical current I_c biased with current I_b takes the form:

$$U(\delta) = -\frac{\Phi_0 I_c}{2\pi}\left(\cos\delta + \frac{I_b}{I_0}\delta\right) \tag{3.1}$$

where δ is the phase across the junction. Due to its shape, this potential is often known as the *tilted washboard*. We consider the quantum mechanics of this potential in detail in appendix A, and will use several of those results in this chapter. For visual reference, the tilted washboard is diagrammed in Figure 3.1, showing a current bias with two states in the well. The junction bias and junction area set the number of levels in the well and the junction plasma frequency (which is close to but not exactly ω_{eg}) for a given current bias; these are plotted against the relative current bias $i_b = I_b/I_c$ in Figure 3.2.

For operation as a JPM, we want a junction whose plasma frequency is close to
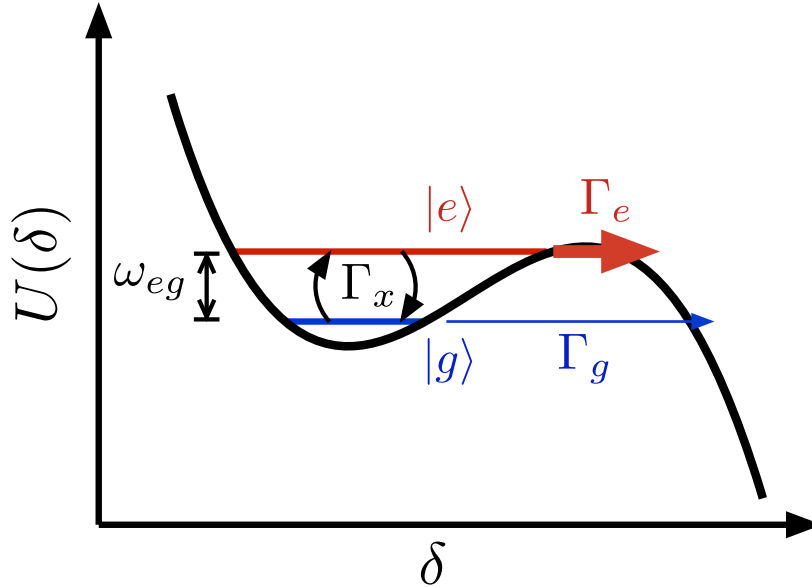
Figure 3.1: Diagram showing the JPM potential with two states in the well. The states are separated by energy $\hbar\omega_{eg}$ and tunnel to the voltage state with rates $\Gamma_{e,g}$. Γ_x is the rate of excitation between ground and excited states, akin to the Rabi frequency.

the frequency of incident microwave photons at a point where there are two levels in the potential well. As the figure shows, a Josepshon junction with reasonable area and critical current density satisfies both these requirements for frequencies that are relevant to cQED experiments. At these values of current bias, the ratio of excited to ground state tunneling rates is $\Gamma_e/\Gamma_g \sim 300$, with $\Gamma_g \sim 1-10\,\text{MHz}$. We therefore expect to be able to operate the JPM with a pulsed "on" time of tens to hundreds of nanoseconds while not accumulating too many dark counts where the junction switches from the ground state without absorbing a photon. The junction levels will be broadened by both the shallowness of the potential well as well as the strong coupling to the environment. We can estimate the width of the junction
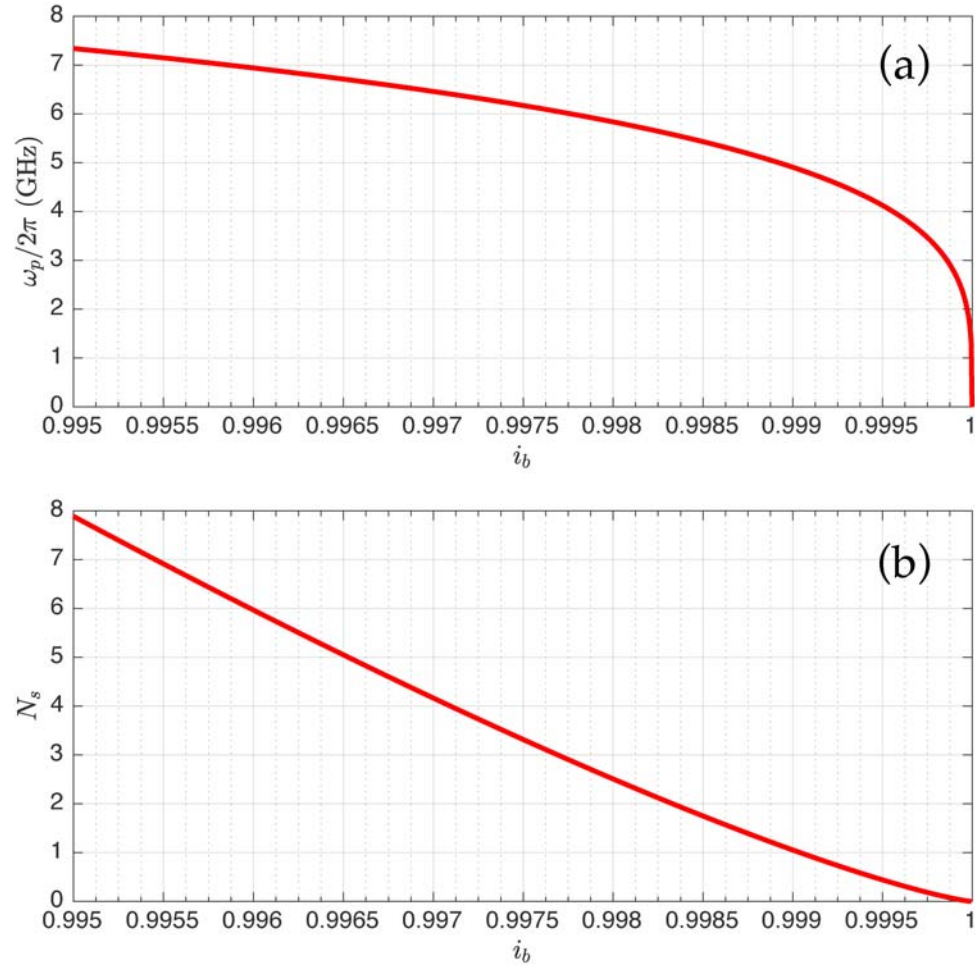
Figure 3.2: (a) JPM plasma frequency ω_p and (b) approximate number of states in the well N_s versus relative current bias i_b for a $500\,\mu\text{m}^2$ junction with $J_c = 35\,\text{A}/\text{cm}^2$.

resonance from the relation $T_1 \approx RC$. For an environmental impedance of order $50\,\Omega$, we expect $\Delta f = 1/T_1 \approx 800\,\text{MHz}$. This shows that the JPM is an intrinsically broadband device, with a quality factor $Q \sim 10$.

3.2 JPM Performance

The arrival rate for photons arriving at the JPM can be characterized as a Poisson process [146, 28]. For a flux of photons λ that is constant in time, the probability of n photons arriving is given by

$$P(n) = \frac{(\lambda t)^n}{n!}e^{-\lambda t} \tag{3.2}$$

However, since the JPM does not have any ability to resolve the number of photons absorbed by the junction during the time it is active, we are interested in the arrival probability of one or more photons:

$$P(n > 1) = \sum_{n}^{\infty} \frac{(\lambda t)^n}{n!}e^{-\lambda}$$
$$= 1 - e^{\lambda t} \tag{3.3}$$

Of course, the probability of no photons arriving at the junction is simply $e^{-\lambda t}$. For a non-constant flux of photons, the same calculation is valid but since we are now considering an inhomogeneous poisson process we need to make the substitution

$$\lambda t \to \Lambda(t) = \int_{-\infty}^{t} \lambda(\tau)d\tau \tag{3.4}$$

3.2.1 Quantum Efficiency

With these preliminaries, we can begin to understand how to characterize the performance of the JPM. There are two kinds of experiments we can perform on

the photon counter. For both, we will assume the JPM is turned on for a fixed amount of time t.The first is to measure switching probability with no photons, the dark probability P_d. The second is to measure the switching probability for a fixed incident photon flux, which we will refer to as the bright probability P_b. For a perfect detector which always switches given a photon and using Equation 3.3, these two quantities are related by:

$$P_b = (1 - e^{-\lambda t}) + e^{-\lambda t} P_d \tag{3.5}$$

An imperfect detector can be characterized through its quantum efficiency η: the fraction of photons which cause a detection event. This can be thought of as an absorber in front of an ideal detector that reduces the incident photon flux to $\eta\lambda$. Therefore, the bright probability for a real detector will be given by:

$$P_b = (1 - e^{-\eta\lambda t}) + e^{-\eta\lambda t} P_d \tag{3.6}$$

Or, solving for the quantum efficiency:

$$\eta = \frac{1}{\lambda t} \log\left(\frac{1 - P_d}{1 - P_b}\right) \tag{3.7}$$

If we know the number of photons which arrive at the junction, by measuring both the bright and dark switching probabilities we can determine the quantum efficiency of the counter. It is important to note that this measurement of the quantum efficiency cannot distinguish between the quantum efficiency that is

intrinsic to the detector and any photon loss that occurs before the detector (for example, because of loss in cabling). The measured quantum efficiency is the product of detector quantum efficiency and all other losses in the system:

$$\eta_{\text{meas.}} = \eta_{\text{det.}}\eta_{\text{cable}}\eta_{\text{isolator}}\eta_{\text{relay}}\cdots \tag{3.8}$$

3.2.2 Contrast

The quantum efficiency is a useful number that is a standard way of parametrizing the performance of a general-purpose photon detecting circuit. Typical numbers for optical detectors range from $\eta = 0.1$ for quantum dot-based detectors to $\eta = 0.9$ or greater for photomultiplier tubes or superconducting transition edge sensors [59]. For the specific case of superconducting qubit readout considered in this thesis, however, we are interested in the fidelity of the readout process. The overall readout fidelity F can be thought of as the probability of correctly identifying the state of the qubit [50]. This can be written as:

$$F = 1 - P(|1\rangle \,|\, |0\rangle) - P(|0\rangle \,|\, |1\rangle) \tag{3.9}$$

where $P(|1\rangle \,|\, |0\rangle)$ is the conditional probability for measuring the qubit in $|1\rangle$ when it was prepared to be in $|0\rangle$. Of course, this quantity depends on the accuracy of the qubit state preparation, the suppression of unwanted transitions between states either by thermal excitation or relaxation. The improvement of this overall system fidelity has been a major effort in the quest to build a universal quantum computer

[76]. Setting aside for now the problem of state preparation and the mapping from qubit state to photon number, which we discuss later, consider the case where a qubit in the ground state leads to no photons reaching the JPM, and a qubit in the excited state leads to many photons reaching the resonator. We will discuss how this can be approximated using a special readout cavity drive protocol in a later chapter; one can also imagine implementing this type of readout using a tunable coupler between the qubit and JPM [132, 153, 53]. In this case, the fidelity of the JPM readout is the difference between the bright and dark switching probabilities. We call this quantity the contrast:

$$C = P_d - P_b \tag{3.10}$$

and this is the key metric for determining the suitability of the JPM for qubit readout in a cQED architecture.

3.2.3 Optimizing Contrast

Let us assume that the dark switching probability is exponential in time, with time constant Γ_0. The contrast can therefore be written as:

$$C = e^{-\Gamma_0 t} \left(1 - e^{-\eta \lambda t}\right) \tag{3.11}$$
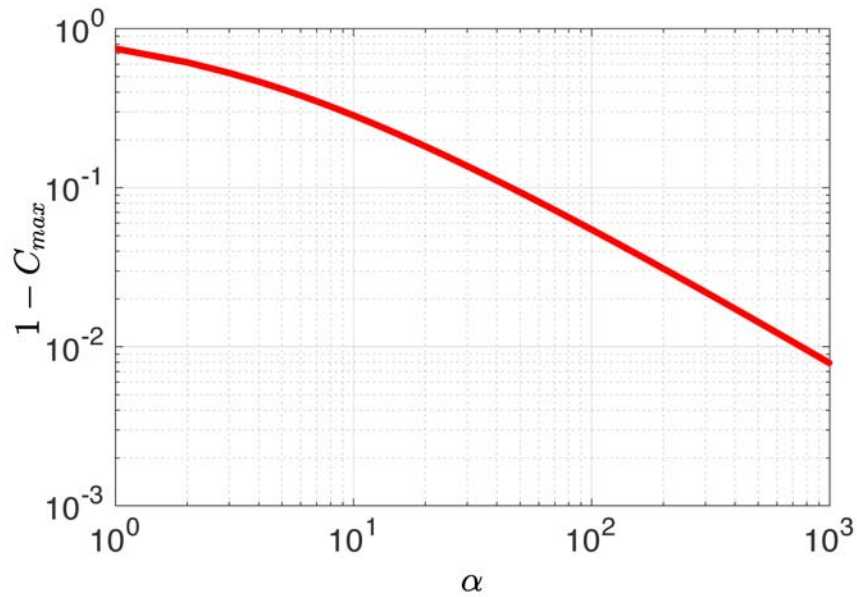
Figure 3.3: Maximum contrast *versus* figure of merit α.

Taking a derivative with respect to time, it is easy to see that there exists an optimal measurement duration for the JPM. Defining

$$\alpha \equiv \frac{\eta \lambda}{\Gamma_0} \tag{3.12}$$

this time is given by:

$$t_{\max} = \frac{1}{\Gamma_0} \frac{\log(\alpha + 1)}{\alpha} \tag{3.13}$$

where the maximum contrast is

$$C_{\max} = \alpha(\alpha + 1)^{-(1+\alpha)/\alpha} \tag{3.14}$$

For any JPM "on" time t, we have the relation $C(t) \leq C_{\max}$; the maximum contrast possible for a given α is plotted in Figure 3.3. Since $C_{\max}$ is a monotonically increasing function of α, it is a good figure of merit for the photon counter. This shows that there are three pathways to improving the performance of the JPM for qubit readout: increasing quantum efficiency, increasing the flux of photons that reaches the JPM during a measurement, or decreasing the dark count rate.

3.2.4 Noise Equivalent Power

The JPM is not a photon number resolving detector; in many ways, it is similar to optical avalanche photodiodes operating in Geiger mode [121]. To measure incident power, the JPM needs to make repeated measurements from which one can infer the photon number. To this end, and to facilitate comparison between the JPM and more traditional photon counters, in this section we calculate the noise equivalent power (NEP) of the device. NEP is a measure of photodetector sensitivity, and is defined as the power that gives a signal to noise ration of one in a given bandwidth [59].

We assume we take N repeated measurements of the JPM, with each measurement taking a time T. For small input powers, the probability of bright switching during a measurement is given by:

$$P_b = \eta \frac{P_{\text{in}} t}{\hbar \omega} \tag{3.15}$$

where the input power is defined by

$$P_{\text{in}} = \hbar\omega\lambda \tag{3.16}$$

It is important to note that as discussed above the JPM has some dead time T between measurements such that $t \neq T$. The number of bright switches is therefore $N_b = NP_b$ with fluctuation $\Delta N_b = \sqrt{NP_b}$. The total fluctuation is:

$$\Delta N = \sqrt{(\Delta N_b)^2 + (\Delta N_d)^2} \tag{3.17}$$

where $N_d = NP_d$ is the number of dark switches (*i.e.* switches with no radiation applied). The NEP is derived by calculating the input power necessary to produce ΔN switches in N measurements[2]:

$$\Delta N = \text{NEP}\frac{\eta t}{\hbar\omega}N \tag{3.18}$$

Solving for the noise power, and setting the contribution from signal shot noise equal to zero to find the minimum detectable power we find:

$$\text{NEP} = \frac{\hbar\omega}{\eta}\sqrt{\frac{P_d}{Nt^2}} \tag{3.19}$$

Note that $P_d \approx \Gamma_0 t$ and that the number of switching events can be related to the detection bandwidth $B = 1/2T$, so that the noise equivalent power per unit

---

[2]A signal to noise ratio of 1.

bandwidth is:

$$\text{NEP} = \frac{\hbar\omega}{\eta}\sqrt{\frac{2\Gamma_0}{t/T}} \qquad \left[\text{W/Hz}^{1/2}\right] \qquad (3.20)$$

For a reasonable set of parameters $\omega/2\pi = 5\,\text{GHz}$, $\eta = 0.05$, $\Gamma_0 = 1\,\text{MHz}$, $t = 100\,\text{ns}$ and $T = 1\,\text{ms}$, we calculate for the JPM a NEP of $9 \times 10^{-18}\,\text{W/Hz}^{1/2}$. This is similar performance to millimeter wave detectors operating in the Ka-band [123] or W band [163] and compares favorably with superconducting kinetic inductance detectors operating in the infrared [90].

3.3 JPM Input-Output Theory

3.3.1 Model Lagrangian
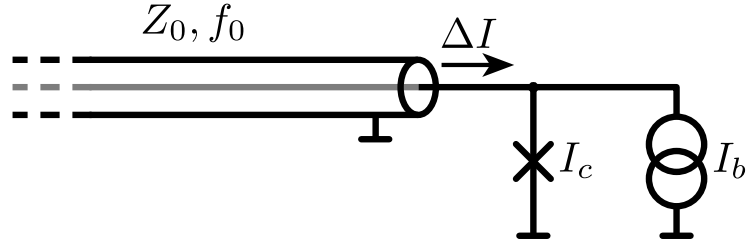
Figure 3.4: JPM coupled to transmission line for input-output theory analysis.

To better understand the optimization of the JPM, we now turn to studying the device using quantum input output theory. The material in this section was largely worked out by Marius Schöndorf [130]. As a model system, we consider a JPM directly connected to a semi-infinite transmission line of characteristic impedance Z_0, as diagrammed in Figure 3.4. The small current from the transmission line ΔI

couples to the phase of the junction, with a system Lagrangian:

$$\mathcal{L} = \mathcal{L}_{\text{TL}} + E_J \cos \delta + (I_b + \Delta_I) \left(\frac{\Phi_0}{2\pi} \right) \delta \tag{3.21}$$

where $\mathcal{L}_{\text{TL}}$ is the Lagrangian of the transmission line [72]. By following the quantization procedure outlined in section 2.1, we can rewrite the variables appearing in 3.21 in terms of the raising and lowering operators for the cavity field and the JPM states[3]:

$$\Delta I = \sqrt{\frac{\hbar \omega_0}{4\pi Z_0}} \left(\hat{a}^\dagger(\omega) + \hat{a}(\omega) \right) \tag{3.22}$$

$$\delta = \frac{1}{\sqrt{2}} \left(\frac{2E_C}{E_J} \right)^{1/4} \left(\hat{\sigma}^\dagger + \hat{\sigma} \right) \tag{3.23}$$

Using the rotating wave approximation [112], the interaction portion of the hamiltonian can be re-written as:

$$\mathcal{H}_{\text{int}} = \hbar g \int_{-\infty}^{\infty} d\omega \left(\hat{a}^\dagger(\omega) \hat{\sigma} + \hat{a}(\omega) \hat{\sigma}^\dagger \right) \tag{3.24}$$

3.3.2 Rates and Levels

We model the system as a harmonic oscillator (the transmission line) coupled to a two level system which can tunnel to a fictitious third "dark" state $|m\rangle$ that represents the junction switching to the voltage state. A similar model was considered numerically by Poudel *et al.* in [115], with the difference that they consider a

---

[3]In this section, we assume that the JPM only has two levels.
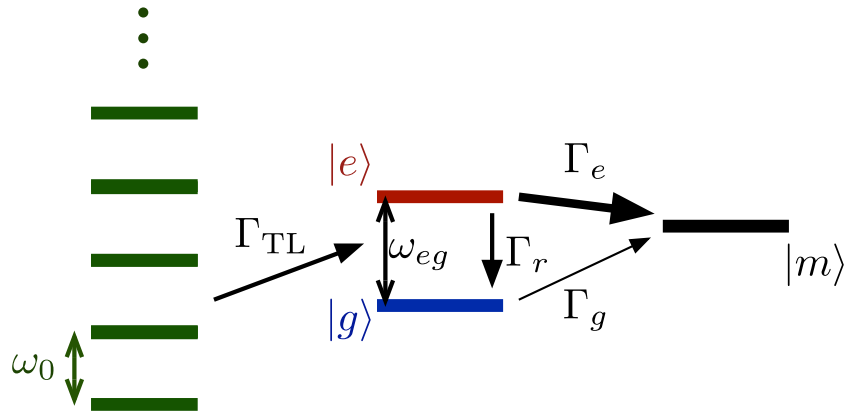
Figure 3.5: JPM levels and rates for the input output theory analysis.

junction capacitively coupled to a transmission line which populated with a fixed number of photons. What they call quantum efficiency is actually contrast, and although they use unrealistically long junction coherence times they report $C > 80\%$ for a single photon in the cavity.

There are four relevant rates in this problem:

- Γ_e and Γ_g, the tunneling rates to the voltage state

- Γ_{TL}, the excitation rate caused by incident microwaves

- Γ_r, the relaxation rate for the junction

The coupling between transmission line and JPM is

$$g = \sqrt{\frac{\omega_0 Z_J}{8\pi Z_0}} \tag{3.25}$$

where $Z_J = 1/\omega_p C_J$ is the junction impedance. This can be rewritten as the coupling

rate to the transmission line

$$
\begin{aligned}
\Gamma_{\mathrm{TL}} &= 2\pi g^2 \\
&= \frac{1}{4}\frac{\omega_0 Z_J}{Z_0} \\
&= \frac{1}{4}\frac{\omega_0}{\omega_p}\frac{\operatorname{Re} Y_0}{C_J}
\end{aligned}
\tag{3.26}
$$

with $Y_0 \equiv 1/Z_0$ the admittance of the transmission line. This last line is suggestive, as Γ_{TL} takes the same form as the effect of dissipation from an arbitrary impedance $Y(\omega)$ on a quantum system, which is given by [23, 37, 103]:

$$
\Gamma \propto \frac{\operatorname{Re} Y(\omega)}{C}
\tag{3.27}
$$

We can also use this expression to model the inelastic relaxation rate of the junction caused by its environment. The relevant admittance seen by the junction is that at its transition frequency:

$$
\Gamma_r = \frac{\operatorname{Re} Y(\omega_{eg})}{C_J}
\tag{3.28}
$$

We calculate the tunneling rates and JPM transition frequency using the complex scaling method discussed in appendix A.

3.3.3 Reflection Coefficient

By using the quantum Langevin equation [82], it is possible to write down the time derivatives of the JPM state operators:

$$\frac{\partial \hat{\sigma}}{\partial t} = -\left(i\omega_0 + \frac{\Gamma_{\text{TL}} + \Gamma_e}{2}\right)\hat{\sigma}(t) + \sqrt{\Gamma_{\text{TL}}}a_i(t)\hat{\sigma}_z(t) \tag{3.29}$$

$$\sigma(t) = \frac{\hat{a}_i(t) + \hat{a}_o(t)}{\sqrt{\Gamma_{\text{TL}}}} \tag{3.30}$$

The input and output operators $\hat{a}_i$ and $\hat{a}_o$ are defined by the relations:

$$\hat{a}_i = -\frac{i}{\sqrt{2\pi}}\int_{-\infty}^{\infty} d\omega e^{-i\omega t}\hat{a}(\omega) \tag{3.31}$$

$$\hat{a}_o = -\frac{i}{\sqrt{2\pi}}\int_{-\infty}^{\infty} d\omega e^{-i\omega(t-t_1)}\hat{a}(\omega), \qquad t_1 > t \tag{3.32}$$

Equation 3.29 is not in general solvable because of the nonlinear coupling between the qubit state and the photon field. Instead, we approximate $\hat{\sigma}_z$ by its expectation value

$$\hat{\sigma}_z \approx P_g - P_e \tag{3.33}$$

Using eq. (3.30) and eq. (3.33) in eq. (3.29), we derive the reflection coefficient for the junction which relates input and output modes:

$$R(\omega) = -\frac{\frac{\Gamma_{\text{TL}} + \Gamma_e}{2} - \Gamma_{\text{TL}}(P_g - P_e) - i(\omega - \omega_0)}{\frac{\Gamma_{\text{TL}} + \Gamma_e}{2} - i(\omega - \omega_0)} \tag{3.34}$$
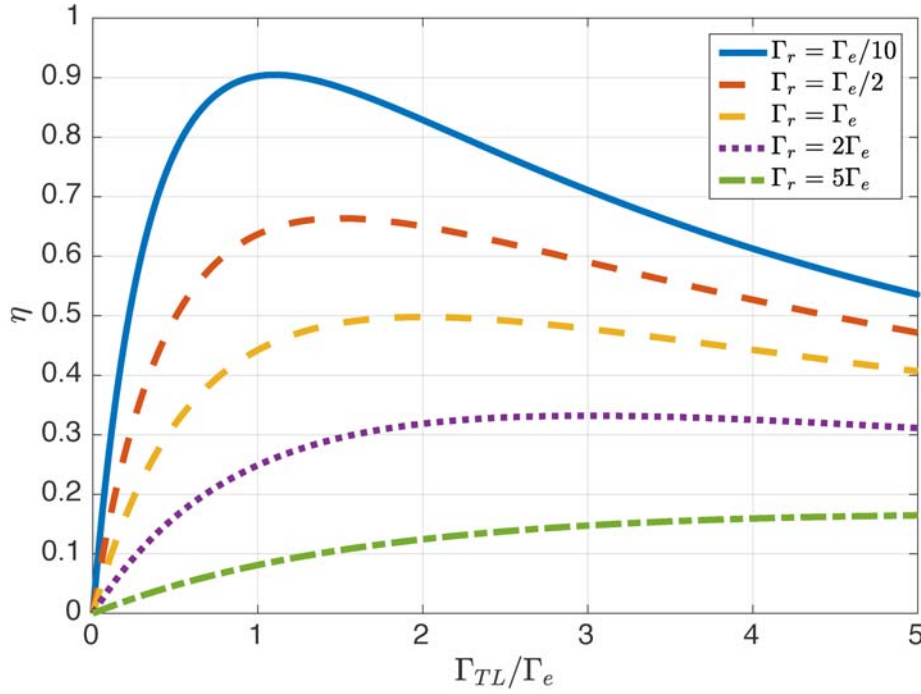
Figure 3.6: Calculated quantum efficiency η vs. coupling to transmission line for different junction relaxation rates with $\Gamma_e = \Gamma_g/300$.

3.3.4 Quantum Efficiency

Armed with the relation between input and output modes, we can calculate the time derivatives of all of the relevant state operators and derive rate equations for the system probabilities. Assuming an incident drive with $N_i = \hat{a}_i^\dagger \hat{a}_i$ photons, we can calculate the quantum efficiency from:

$$\eta = \frac{1}{N_i}\left(\Gamma_e P_e(N_i) + \Gamma_g P_g(N_i) - \Gamma_0 P_g(N_i = 0)\right) \tag{3.35}$$

The complete solution for a non-resonant drive and including inelastic relaxation reads:

$$\eta = \frac{\Gamma_{\text{TL}}\left(1 + \frac{\Gamma_g}{\Gamma_{\text{TL}}+\Gamma_e+\Gamma_r}\right)(\Gamma_e - \Gamma_g)}{\frac{1}{4}(\Gamma_{\text{TL}} + \Gamma_e + \Gamma_g + \Gamma_r)^2 + (\omega - \omega_0)^2} \tag{3.36}$$

This expression is plotted in Figure 3.6.

Setting the detuning $\omega - \omega_0 = 0$ this has a maximum for coupling to the transmission line at:

$$\Gamma_{\text{TL}}^{\text{max}} = \sqrt{(\Gamma_e + \Gamma_r)(\Gamma_e + \Gamma_g + \Gamma_r)} \tag{3.37}$$

We know that $\Gamma_e \gg \Gamma_g$, so this condition amounts to $\Gamma_{\text{TL}}^{\text{max}} = \Gamma_e + \Gamma_r$. Thinking of the tunneling to the voltage state from the excited state as being caused by a fictitious resistance $R_T = 1/\Gamma_e C_J$, this amounts to a *matching condition*:

$$\frac{1}{Z_{\text{TL}}C_J} = \Gamma_e + \Gamma_r \tag{3.38}$$

Since the coupling is set by the impedance of the input transmission line, this is a quantum mechanical equivalent of a condition for the maximum transfer of energy to the JPM.Perhaps unsurprisingly, to maximize the quantum efficiency of the detector we need to match the $50\,\Omega$ impedance of the transmission line to impedance of the junction, which we accomplish using a simple LC matching network. The calculated η for a particular value of Γ_g is plotted in Figure 3.7, which also shows the optimal input coupling rate. A complication arises in the fact that Γ_{TL} and Γ_r are not independent; they both are determined by the impedance of the matching network[4]. We choose an input matching network impedance that

---

[4]The additonal $50\,\Omega$ from the bias line appears in parallel and is negligible.

transforms the transmission line impedance to $Z_0 \approx 1\,\Omega$, which maximises efficiency. The rates for such a matching network input are plotted in Figure 3.8, with the quantum efficiency plotted in Figure 3.9. This shows that it should be possible to acheive quantum efficiencies on the order of 10% for dark rates of a few megahertz. Finally, we plot the expected contrast (bright switching minus dark switching) for a JPM active time of $100\,$ns during which 50 photons arrive at the junction in Figure 3.10. Based on the input-output theory formulated in this section, we expect to be able to achieve raw contrasts of greater than 90% for this type of drive.
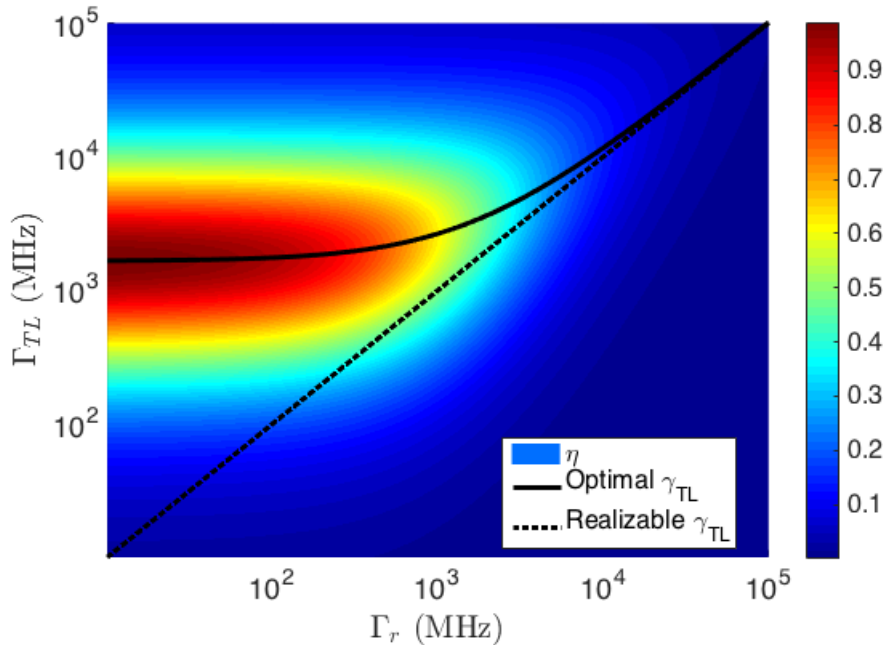
Figure 3.7: Calculated quantum efficiency η vs. relaxation rate and input coupling rate Γ_{TL} for $\omega_0/2\pi = 5\,$GHz, detuning $\Delta = 0$ and $\Gamma_g = 5\,$MHz. The optimum input coupling is shown as a solid line, while the realizable values of input coupling are shown as a dashed line.
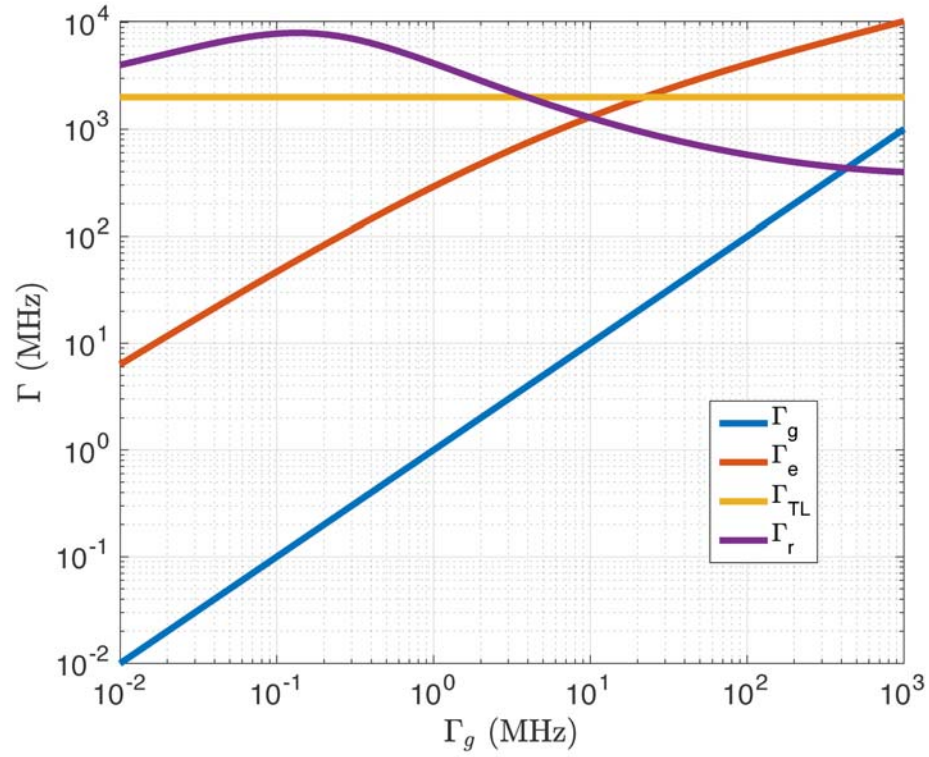
Figure 3.8: Plot of relevant JPM rates for a $500\,\mu m^2$ junction with $J_c = 35\,A/cm^2$. The JPM is driven at $5\,GHz$ through an LC matching network with $L = 200\,pH$ and $C = 5\,pF$.
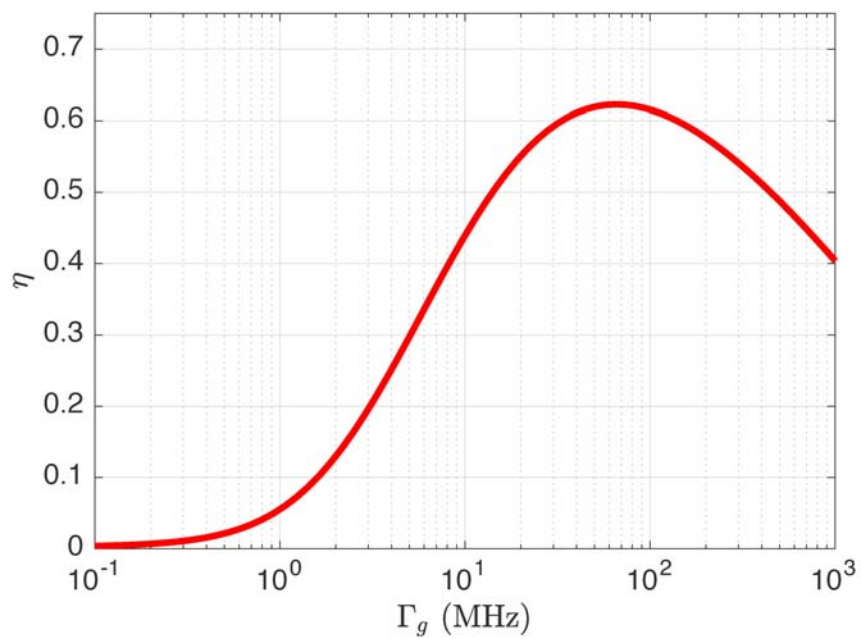
Figure 3.9: Plot of quantum efficiency η vs ground state tunneling rate Γ_g. Parameters are the same as for Figure 3.8
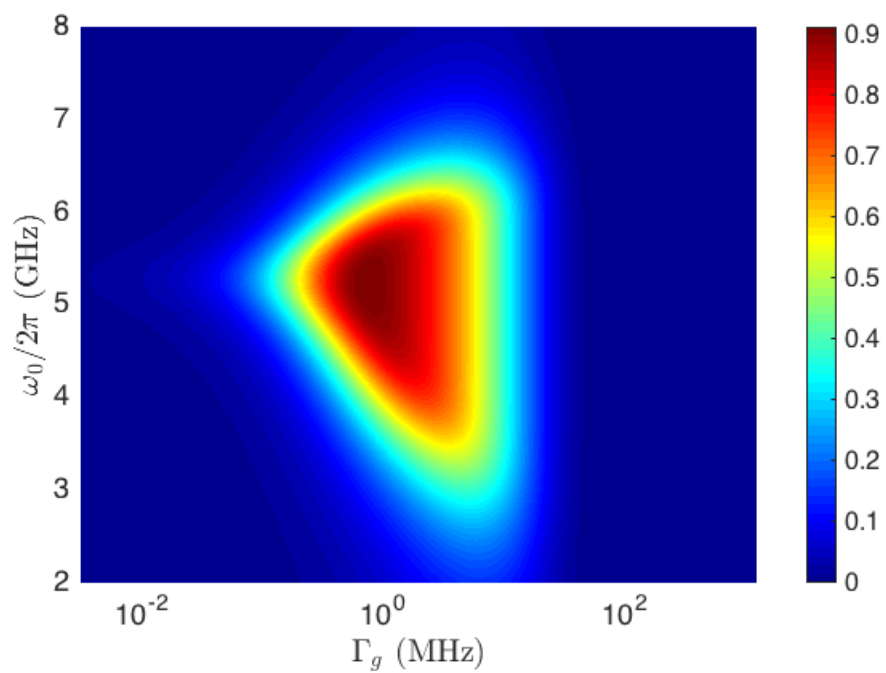
Figure 3.10: Plot of contrast $C = P_b - P_d$ vs. ground state tunneling rate Γ_g and input frequency $\omega/2\pi$. Parameters are the same as for Figure 3.8, for a JPM on time of $100\,\text{ns}$ and 50 incident photons.

4 JPM FABRICATION AND MEASUREMENT TECHNIQUES

One of the major advantages of the Josephson photomultiplier compared to the traditional microwave amplifiers described in the Introduction is the simplicity of its design. As an illustration of this fact, the SLUG amplifier's fabrication requires 8 rounds of photolithography [64, 66], compared to only 3 for the JPM design described in this thesis. This simple, single-junction design is also inherently compact, eliminating the need for large resonant structures such as those found in many types of parametric amplifiers; for instance, the TWPA amplifier [157, 96] needs several thousand sub-micron junctions and occupies the majority of a standard silicon die. A final advantage compared to amplifiers used for heterodyne measurement is the simplicity of the room-temperature electronics needed to read out the JPM. A simple voltage comparator[1] is all that is needed to detect the large transient caused by the junction switching to the voltage state. As we will discuss in the final chapter of this thesis, this also presents interesting opportunities for integration with cryogenic quantum control electronics.

In this chapter we will describe the fabrication process used to make the JPM using standard photolithographic thin-film techniques and the design choices we made when fabricating these devices. We will then describe the measurement set-up for JPM experiments, including the wiring of cryogenic refrigerators, the room-temperature electronics used to control and read-out the JPM, and our custom measurement software setup.

---

[1] Our collaborators at Syracuse University have even implemented this using discrete components read out with a cheap Arduino board connected via USB.

4.1 Thin Film Fabrication Techniques

The Josephson photomultipliers described in this thesis were fabricated using thin film microfabrication tools in both the McDermott Lab and at the Wisconsin Center for Applied Microelectronics (WCAM), the shared cleanroom at UW-Madison. In this section, we will describe the individual steps used in JPM fabrication.

4.1.1 Photolithography

The common thread that unites all of the thin film processing steps that we use to fabricate the JPM is photolithography using the Nikon i-line stepper at WCAM. This production-grade tool[2] uses a massive lens to do projection lithography using a quartz reticle. Features on the mask are drawn in chrome, and reduced in size 5x on the wafer where the light from a mercury vapor lamp exposes photoresist. We use *Megapost SPR 955-CM* resist, which allows us to write lines down to $0.5\,\mu m$ with overlay accuracy of better than $100\,nm$. The main advantage of using a stepper to do lithography instead of a contact mask system is that we can arrange many different variations of a circuit onto the same wafer by programming what features get exposed on an individual die.

After the wafer is cleaned using acetone and isopropanol, the resist is spun onto the wafer at $3500\,rpm$ for $30\,s$, leaving a $0.9\,\mu m$-thick film. Solvents in the resist are removed with a $95\,°C$ pre-bake for $1\,min$. The stepper exposes the resist

---

[2]Used, apparently, to expose Pentium I processors at Intel.

for approximately[3] $290\,\text{ms}$, and we perform a $1\,\text{min}$ post-exposure bake at $110\,°\text{C}$. Finally, the resist is developed by agitating the wafer in *Megaposit MF-24A* for $60\,\text{s}$. Since SPR-955 is a positive resist, areas that were exposed to light are removed by the developer. Care needs to be taken when developing resist over aluminum, as MF-24A etches it slowly.

4.1.2   Aluminum Deposition and Etch

To deposit the superconducting metal thin films used in all of the devices fabricated in the McDermott Lab, the primary system we use is the *Kurt J Lesker* sputtering system. This commercial tool is set up for DC sputtering using magnetron-type sputter sources, and is currently configured with both niobium and aluminum targets. The chamber also features an argon ion mill for surface cleaning and metal oxide removal *in situ*. The system is brought to high vacuum using a closed cycle refrigerator cryopump, typically achieving base pressures around 1×10^{-8} torr. Samples (pieces, 2" diameter wafers, or 3" wafers) are cleaned with dry nitrogen and clamped to an aluminum platen with an indium O-ring for heat-sinking. The heat load on the samples is relatively high, and the indium O-ring is vital to ensure the growth of high-quality films that are free of defects. The wafer chuck is inserted into the chamber using a load-lock and screwed into a rotating arm that provides sample rotation and repositioning, allowing the user to ion mill and deposit either kind of metal in a single use.

The first step before depositing an aluminum film is to clean the surface using

---

[3]The exact length of time is determined by the age of the stepper lamp, and must be calibrated.

the ion mill, which uses a physical etch process. This is important to both remove the thermal oxide layer on the silicon wafers before growing the bottom electrode of the JPM, and to clear the natural oxide layer that forms on aluminum when exposed to atmosphere. Removing this oxide allows for good metal to metal contact when growing junctions on top of the base aluminum. The mill ionizes argon gas using a hot cathode filament, and argon ions are accelerated using a grid system that is biased with a large voltage. On impact with the sample, the ions have sufficient energy to knock atoms off the surface. We operate the ion mill in the Lesker system at an argon pressure of 2×10^{-4} torr, a bias voltage of $800\,\mathrm{V}$ and a beam current of $20\,\mathrm{mA}$. These parameters result in a measured etch rate of $1\,\mathrm{nm/s}$ for aluminum and $1.5\,\mathrm{nm/s}$ for silicon oxide. The etch rate is important to take into account when designing features which rely on a certain thickness of material, for example overlap (parallel-plate) capacitors. We etch samples for $20\,\mathrm{s}$, which is enough of an over-etch to ensure complete oxide removal, although this does roughen the surface. While not an important consideration for the relatively simple JPM fabrication, this can be a concern for more complicated multi-layer devices such as SLUGs and qubits.

Once the surface is clean, we proceed to aluminum deposition using magnetron sputtering. In this process, energetic ions from a magnetically confined argon plasma dislodge aluminum atoms from the target, which then coat the sample. It is important to rotate the sample during sputtering to ensure uniform film thickness across the sample wafer. Since we are sputtering metals in the Lesker system, we can use a power regulated DC source to create the plasma[4]. The deposition is a

---

[4]Dielectric targets are susceptible to charge build-up, and must be sputtered using an RF source.

two-step process. First, the target is cleaned using a $200\,\mathrm{W}$ plasma for $2\,\mathrm{min}$, with a closed shutter placed right in front of the target. The plasma power is then reduced to $110\,\mathrm{W}$ and the shutter opened to begin sputtering. We use a constant argon pressure of $5\,\mathrm{mTorr}$, which results in slightly compressive films and a deposition rate of $10\,\mathrm{nm/min}$.

Once lithography has been performed on the aluminum film, it is wet etched using *Transene Type A* aluminum etchant. The etchant is heated to $50\,°\mathrm{C}$, which gives an etch rate of $10\,\mathrm{nm/s}$. As wet etching is isotropic, it must be closely monitored to prevent any undercutting where the aluminum underneath the resist is etched near the edge of features. While not as repeatable as a dry metal etch, wet etching is simple, robust, and produces a gentle edge slope which alleviates step-coverage issues. After etching, the resist is stripped by sonicating the wafer in an acetone bath.

4.1.3   Silicon Oxide Deposition

Chamber Pressure		$900\,\mathrm{mTorr}$
Temperature		$250\,°\mathrm{C}$
RF Power		$25\,\mathrm{W}$
Gas Flows	N_2O	$900\,\mathrm{sccm}$
	2% SiH_4 in N_2	$400\,\mathrm{sccm}$

Table 4.1: PT70 SiO_x deposition recipe.

The dielectric used in the JPM is a conventional silicon oxide (SiO_x) grown using plasma-enhanced chemical vapor deposition (PECVD) at WCAM. PECVD uses gas-phase chemical reactions catalyzed by an RF plasma whose products precipitate

on a sample to grow a thin film of material. The sample is heated to increase film quality by reducing surface roughness and pinhole formation. The PECVD process parameters for the *Plasmatherm PT70* system at WCAM are listed in Table 4.1. Using this recipe, the typical deposition rates are $30-40$ nm/min. Since the JPM matching network uses a large parallel-plate capacitor whose thickness must be conrolled to set the frequency of JPM operation, we monitor the deposition rate using bare silicon witness chips placed in the chamber alongside the sample wafer. The thickness of silicon oxide on the witness dies can then be measured extremely accurately using an optical reflectometer. After deposition and lithography, the oxide is etched using

Chamber Pressure		100 mTorr
RF Power		150 W
Gas Flows	CHF_3	50 sccm
	O_2	20 sccm

Table 4.2: SiO_x RIE recipe.

a reactive ion etch (RIE) in the WCAM *Unaxis 790* chamber. This processes uses a chemically reactive plasma containing fluorine to etch the sample. The recipe we use is listed in Table 4.2, and it etches silicon oxide at 30 nm/min. Aluminum acts as an excellent etch stop, so we typically over-etch by 50%. Lithography on SiO_x is nearly identical to that on metal with two important differences. Before resist is spun on, the wafer is coated with hexamethyldisilazane (HMDS) and baked in a vacuum. The HMDS promotes resist adhesion during subsequent processing steps. After the resist post-exposure bake, we bake the resist for an additional 3 min at $130\,°C$. This causes the resist to thermally flow, producing a 45-degree edge slope. The RIE etches the oxide at the same rate as the resist, so that this slope is transferred

to the dielectric. This, shown in Figure 4.1 helps prevent any step coverage problems for metal on top of the dielectric. Exposure to the reactive plasma polymerizes the resist; this makes it much harder to remove post-etch. Sonication in *Microposit 1165 remover* for 30 min followed by another 30 min sonication in acetone gives good results, although occasionally this must be repeated multiple times.
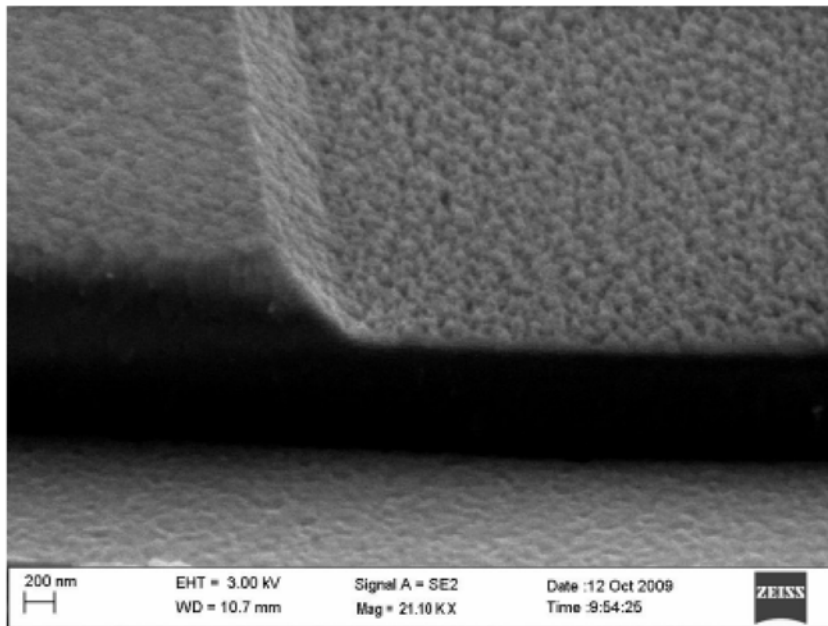
Figure 4.1: SEM image of SiO_x etch profile in the 790 RIE tool showing $45°$ slope. Image courtesy Umesh Patel.

4.1.4 Josephson Junction Growth

The junctions in the JPM are formed using an Al-AlO_x-Al stack. The bottom electrode is the base aluminum deposited before dielectric deposition and via etch, while the top electrode also forms the wiring traces to route the microwave input

and current bias to the junction. The oxide is grown in our Lesker sputtering system, and we again use the ion mill for $20\,\mathrm{s}$ to clean any native oxide off of the aluminum ground plane. A clean interface between metal and oxide is critical to achieving reliable and repeatable junction critical current density. Once the mill is complete, oxygen is flowed into the chamber at $1\,\mathrm{mTorr}$ for $2\,\mathrm{min}$ to seed the formation of the tunnel barrier. The cryopump gate valve is then closed and the chamber pressure is allowed to rise to the target value for junction oxidation, where it remains for $10\,\mathrm{min}$. Following the oxidation, the aluminum counter-electrode is grown using the procedure outlined above. Unfortunately, the junction growth is the most variable part of the fabrication process. The critical current density J_c (critical current per unit area) reached for a given chamber pressure depends on the chamber's history, so two wafers fabricated a few days apart may not have the same J_c. However, for two junction growths close together in time the critical current density scales inversely with the square root of the product of oxygen pressure and time (also referred to as the exposure) [79]. We therefore typically process two wafers in parallel, expose the junctions on one wafer and measure their critical current density using Equation 2.17, and then use that data to correct the exposure of the second wafer to reach the target J_c. For the JPM target critical current density of $35\,\mathrm{A/cm^2}$, the oxygen pressure in the chamber is approximately $300\,\mathrm{mTorr}$.

4.1.5 JPM Fabrication

The JPM fabrication process consists of three layers processed in WCAM and the McDermott Lab using the techniques described above: the base electrode, the
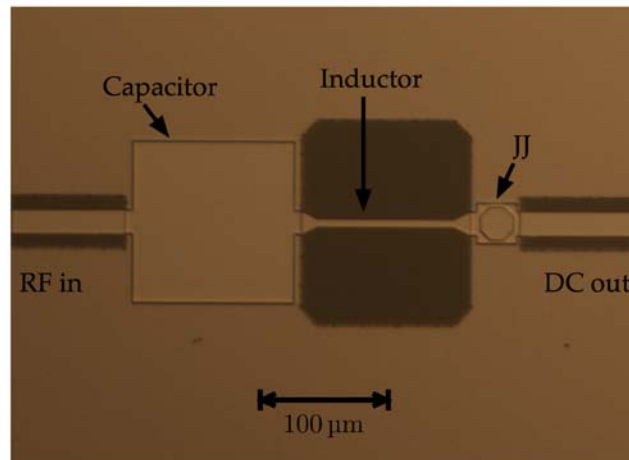
Figure 4.2: Micrograph of a JPM chip showing the matching network capacitor and inductor, and junction (JJ), as well as input and output coplanar waveguide lines.

dielectric, and the counter (or top) electrode. A micrograph of the completed chip showing the important features of the device can be seen in Figure 4.2.

Substrate and Base Electrode

The JPM described in this thesis are fabricated on standard commercial $3\,\text{in}$ diameter oxidized silicon wafers. The thermal oxide ($150\,\text{nm}$ thick) ensures electrical isolation between different parts of the device. As the JPM is a relatively low-Q device, there is no need to use the high quality intrinsic silicon wafers that are used for qubit fabrication [63]. After an ion mill cleaning, the base aluminum is sputtered to a thickness of $100\,\text{nm}$ and wet-etched.

This base layer acts as the chip ground as it is wire-bonded to the aluminum sample box which acts as a superconducting shield. At high frequencies the return current paths flowing on the chip have non-negligible inductance, especially since in superconductors current flow is located at the edge of metals [140]. We take great

pains to minimize this return inductance, as it can be a significant contribution to designed inductances. Additionally, cuts in the ground plane such as the slot formed by the coplanar waveguide input and output lines, or around wire bond pads, can lead to unwanted microwave resonances on the chip (so-called chip modes). To minimize these effects, the two halves of the ground plane are tied together using crossovers that pass underneath the coplanar waveguide center (CPW) trace.

Dielectric and Vias

The silicon oxide dielectric is grown to be $120\,\mathrm{nm}$ thick and etched using the CHF_3 RIE described above. The matching network capacitor to ground is of the parallel plate type, with the SiO_x having a dielectric constant $\epsilon_r = 3.9$. The design of the capacitors takes into account the $20\,\mathrm{nm}$ extra etch that will be caused by the ion mill step before the junction is grown. The JPM via is octagonal, and in this step additional test junction vias are opened in test structures near the edge of the die for room-temperature junction resistance measurement. The dielectric covers the whole chip, so it must also be etched away over the ground plane near the edge of the die so that ground wirebonds can be made. These open areas will form large parasitic vias in the subsequent step, but they are so large that their critical current will never be exceeded and they will never switch to the voltage state.

Junction and Counter-Electrode

The final thin-film processing step is the growth of the Josephson junction and the deposition of the $100\,$nm thick counter electrode (CE). This is the layer that carries the input and output signals to and from the JPMs through $50\,\Omega$ coplanar waveguide transmission lines. One particularity of our JPM design is that the CPWs' center trace is formed in the CE layer, making it not strictly coplanar. However, as the dielectric thickness is much smaller than the lateral dimensions of the coplanar waveguide ($18\,$µm center trace and $10\,$µm gaps) this is not a significant correction. On the other hand, the distributed capacitance of the crossovers has to be taken into account and corrected for when choosing the CPW dimensions.

The other crucial feature made in the CE layer is the series inductor in the input matching network. This is formed using a thinner $3\,$µm trace over a cavity in the ground plane. There are three contributions to this inductance that must be taken into account. The first is the geometric inductance of the thin trace, which can be calculated using the standard expressions for CPW with a large ground plane gap [135]. For the JPM geometry, this is $1\,$pH/µm. There is also a contribution from the kinetic inductance of the superconducting trace. This inductance can be approximated using the expression:

$$L_K = \mu_0 \lambda^2 \frac{\ell}{wt} \tag{4.1}$$

where $\lambda = 100\,$nm is the penetration depth, ℓ is the length of the trace and w and t are the width and thickness of the trace. For the JPM, this expression shows that

the kinetic inductance is $L_K \sim 4 \times 10^{-4}\,\mathrm{pH/\mu m}$, small enough to be disregarded. The final contribution comes from the return current that flows around the outside of the inductor cavity. This inductance is in series with the explicit inductor, and is not negligible. Since the geometry is complex it would be difficult to calculate this inductance explicitly, so we simulate it using the *FastHenry3* package [74]. Calculated total inductance per unit length as a function of cavity aspect ratio (length divided by width) is plotted in Figure 4.3. As expected, for large aspect ratio cavities we recover the CPW expression, but for shorter cavities the contribution is significant. The cavities used for the JPM are nearly square, and the total inductance is approximately $1.5\,\mathrm{pH/\mu m}$.
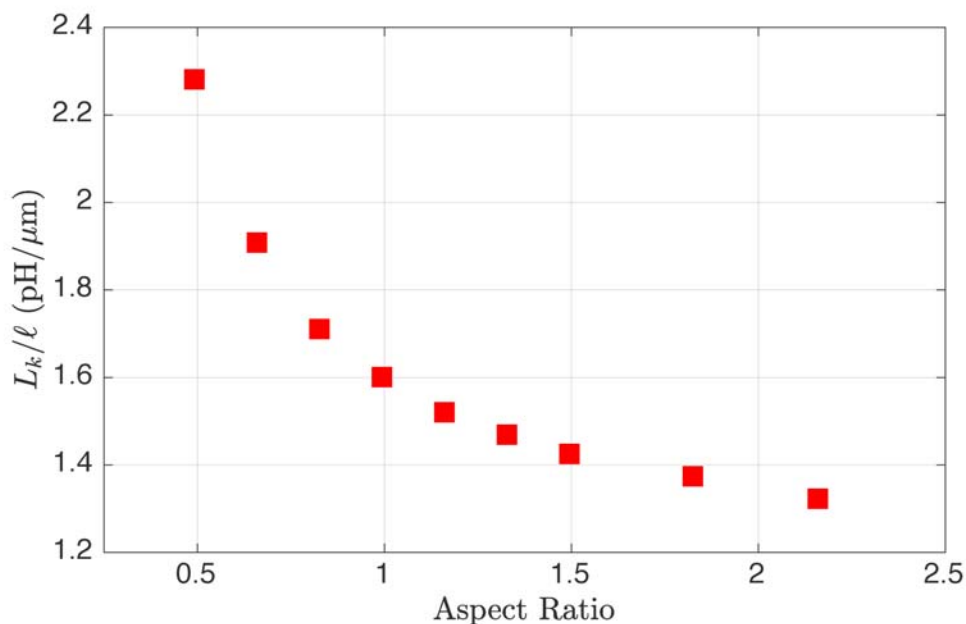
Figure 4.3: Simulated inductance per unit length *versus* ground plane cavity aspect ratio.

Dicing and Packaging

Once the devices are probed and found to have a satisfactory critical current density, the final step before measurement is to dice the wafer into single dies and package the individual JPMs. We use a high speed diamond blade dicing saw to singulate the dies, which are 6.25 mm on a side. It is important to cover the wafer in photoresist and bake it before dicing to protect the devices from the fine silicon dust produced by the saw.

Figure 4.4: JPM wirebonded in aluminum sample box.

Before packaging dies, the photoresist is washed off by gentle sonication in acetone followed by a rinse with isopropanol. They are then mounted in aluminum sample boxes, and the chip ground plane is wedge bonded to the box ground around all 4 sides with approximately 100 20 mil 1% Si-Al wire bonds. The input and output lines are bonded to copper traces that are soldered to non-magnetic brass SMA bulkhead connectors. To reduce any RF mismatch between the printed

circuit board traces and the chip, they are recessed and level with the box ground plane. The chip is thermalized through gold wirebonds that are made from the copper printed circuit board traces to the input and output pads; since they are normal metal, they have high thermal conductivity unlike the aluminum bonds which superconduct below $1\,\mathrm{K}$. A bonded sample can be seen in Figure 4.4. This is the same technique we use to mount transmon chips, with the difference that we do not thermalize the chips through gold bonds as gold cannot be wedge bonded to aluminum at room temperature.

4.2   JPM Design Choices

The target frequency for JPM operation was chosen as $5\,\mathrm{GHz}$, a good compromise between achievable junction plasma frequency ω_p and transmon readout resonator frequency. We chose to work with large junctions; as noted in the discussion in the preceding chapter, we want the inelastic relaxation rate of junction to be on the same order as the tunneling rate from the first excited state. This rate is set by $\Gamma_{in} = 1/Z_0 C_J$, where $Z_0 \approx 50\,\Omega$ is the environmental impedance of the junction[5]. The capacitance C_J of a junction is set by its area, which for our process is roughly $50\,\mathrm{fF/\mu m^2}$. Therefore, we chose a junction area of $500\,\mathrm{\mu m^2}$ giving a capacitance of $5\,\mathrm{pF}$. Using Equation 2.22 to determine ω_p, the required critical current density is $\sim 40\,\mathrm{A/cm^2}$. From the relation

$$\omega_p = \frac{1}{\sqrt{L_J C_J}} \tag{4.2}$$

[5]Specifically, this is the dissipation due to the output bias line.

the junction inductance is $40\,\mathrm{pH}$.
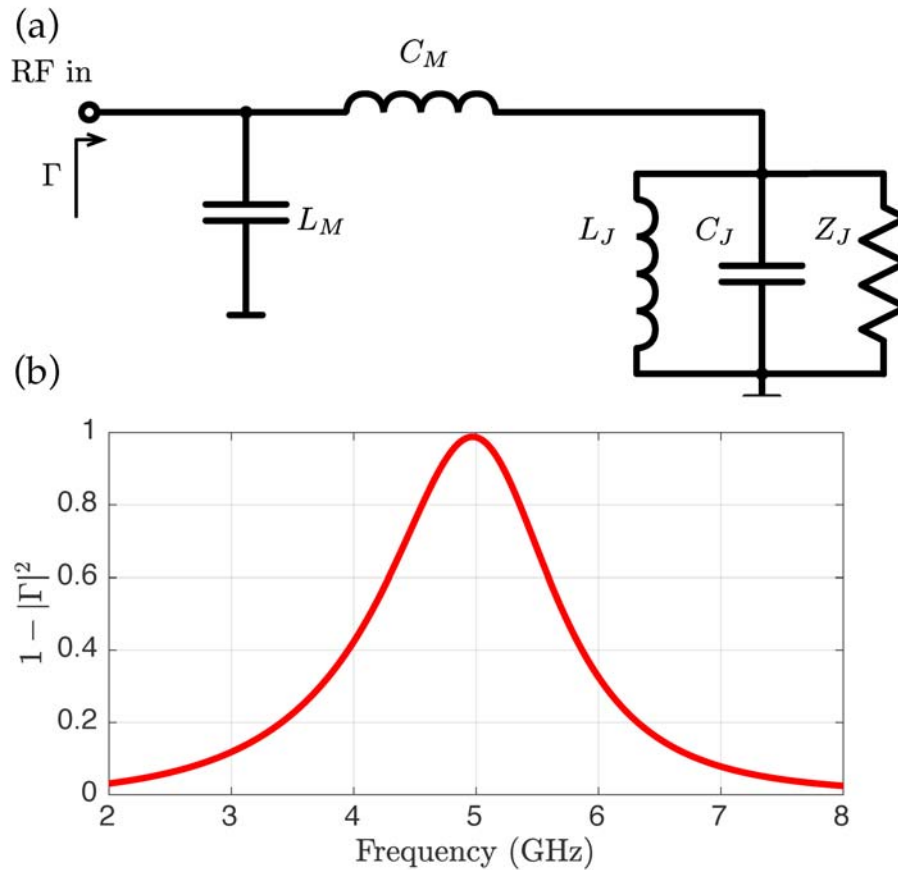
Figure 4.5: (a) Classical equivalent circuit for the JPM input matching network used to calculate the input reflection coefficient Γ. (b) Calculated mismatch loss $1 - |\Gamma|^2$ for the junction and matching network parameters from the text.

Having set the junction parameters, we must set the input matching network parameters. The tunneling rates at a plasma frequency of $5\,\mathrm{GHz}$ yield an equivalent junction resistance on the order of $Z_J \approx 1\,\Omega$. We consider the classical equivalent circuit drawn in Figure 4.5a. Since we are matching to the $50\,\Omega$ source impedance at the input, the quality factor of the network will be $Q \approx 7$, which is well suited to a

single pole LC circuit [117]. A standard calculation [117, 11] shows that the desired parameters for the matching network capacitance and inductance are $C_M = 5\,\text{pF}$ and $L_M = 200\,\text{pH}$. A useful way to characterize the performance of the matching network is by computing the mismatch loss of the circuit, defined as

$$\text{ML} = 1 - |\Gamma|^2 \tag{4.3}$$

where Γ is the reflection coefficient at the input of the circuit. This quantity characterizes the fraction of input power that is dissipated in the circuit, as opposed to being reflected at the input. Since in this simple model of the JPM power dissipated in the fictitious tunneling resistance of the junction is equivalent to photons being absorbed and detected, we want $\text{ML} \sim 1$. For the above parameters, this quantity is plotted in Figure 4.5b.

4.2.1 Matching Network Characterization
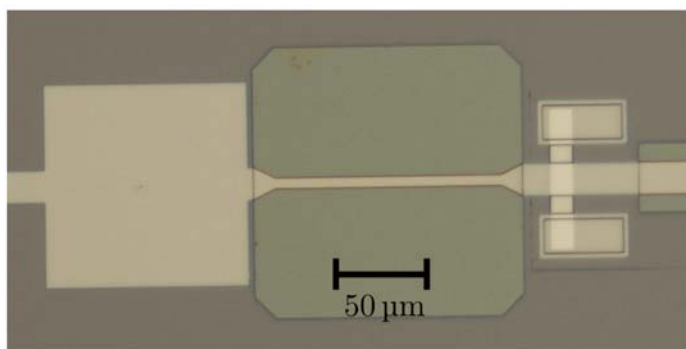
Figure 4.6: Micrograph of a matching network test chip, with the JPM junction replaced with a normal metal Pd resistor.

To validate the above model, we chose to test the performance of the matching network using a mock-up of the junction. This consisted of a matching network circuit of identical layout to that used in the JPM, with the junction replaced by a thin normal-metal resistor. The $30\,\mathrm{nm}$ thick palladium resistor, grown in our electron-beam evaporator after an ion mill step to ensure good metallic contact, has a resistance of $1\,\Omega$, matching the junction tunneling resistance. A micrograph of this test structure is shown in Figure 4.6. The test chip was made using niobium instead of aluminum for the ground plane and counter-electrode. Niobium has a critical temperature $T_c \approx 9\,\mathrm{K}$ [140], so we were able to measure the reflection coefficient of the circuit using a simple dip probe set-up in liquid helium at $4\,\mathrm{K}$. The results of this measurement are shown in Figure 4.7, and are compared to the expected ML based on the design value of capacitance and inductance. It is clear that the response frequency and minimum reflection coefficient of the fabricated circuit correspond closely to the expected value, reassuring us that there are no other large parasitics that could degrade the microwave transmission at the input of the JPM.
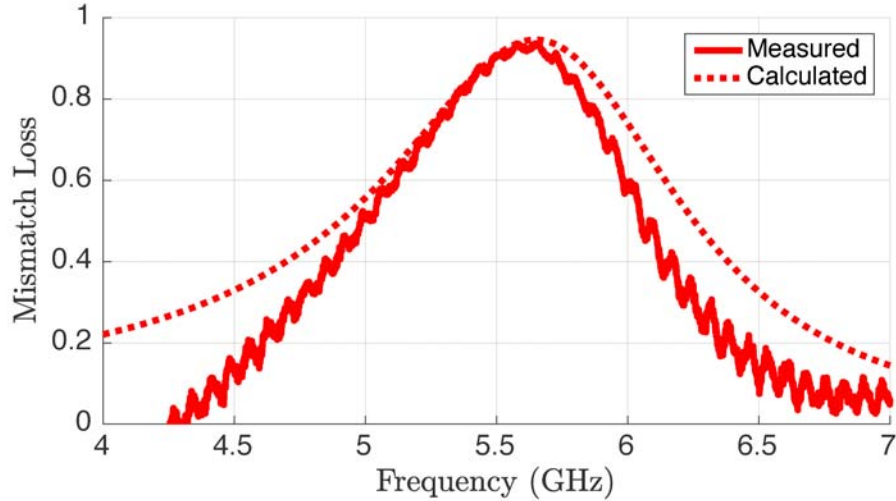
Figure 4.7: Comparison of measured and calculated mismatch loss for a JPM input matching network with the junction replaced by a $1\,\Omega$ Pd resistor. The measured circuit parameters are $C_M = 4\,\mathrm{pF}$ and $L_M = 200\,\mathrm{pH}$. The $125\,\mathrm{MHz}$ ripples in the measured data correspond to the length of cable between the network analyzer and the dip probe; there is likely a small amount of mismatch in an SMA connector that results in a standing wave that is not perfectly calibrated out.

4.3   Measurement Setup

We use two types of cryogenic systems to characterize the JPMs and qubits described in this thesis. The first, used primarily for screening of transmons and photon counters, is an adiabatic demagnetization refrigerator (ADR). These systems use a cryogen-free pulse tube cooler to cool down to $4\,\mathrm{K}$, followed by magnetic refrigeration to cool down to $50 - 100\,\mathrm{mK}$ [60]. ADRs are fast to cool to but only provide a limited time at base temperature, so they are well suited to measurements that need a fast turn around time. The second is a dilution refrigerator (DR), which uses the heat of mixing of a ^{3}He-^{4}He mixture to provide continuous cooling power at millikelvin temperatures [155]. Our workhorse, used for the qubit readout

experiments, is the *Leiden Cryogenics* dilution refrigerator, a dry fridge[6] which offers $600\,\mu$W of cooling power at $120\,$mK and typically achieves a base temperature of $12\,$mK.

4.3.1   Cold Wiring

The qubits and JPMs are heatsunk to the cold stage of the refrigerator, and connected to the outside world through heavily attenuated and filtered microwave and DC control lines. Considerable care needs to be taken when wiring an experiment into either an ADR or DR to avoid heat leaks through wiring and excessive thermal radiation from warmer stages of the fridge. This requires extensive heat-sinking of wiring at all intermediate temperature stages, as well as the heat-sinking of attenuators, filters, and all other components in the signal chain. This is especially crucial for qubit experiments, as infrared radiation is able to break quasiparticle pairs in the superconducting metal on the device chip which lead to excess $|1\rangle$ state population [154]. We mitigated this problem by clamping all cold attenuators, and inserting commercial K&L Microwave $12\,$GHz low-pass filters before and after the qubit in the measurement chain. Additonally, to suppress noise due to magnetic fields and prevent the critical current of the relatively large area JPM junction from being suppressed due to magnetic fields, the JPM and qubit boxes are enclosed in high-permeability mu-metal magnetic shielding. A schematic of the wiring is show in Figure 4.8.

Microwave drive lines are heavily attenuated at both the $4\,$K stage and the

---

[6]This eliminates the need for repetitive and annoying cryogen transfers.
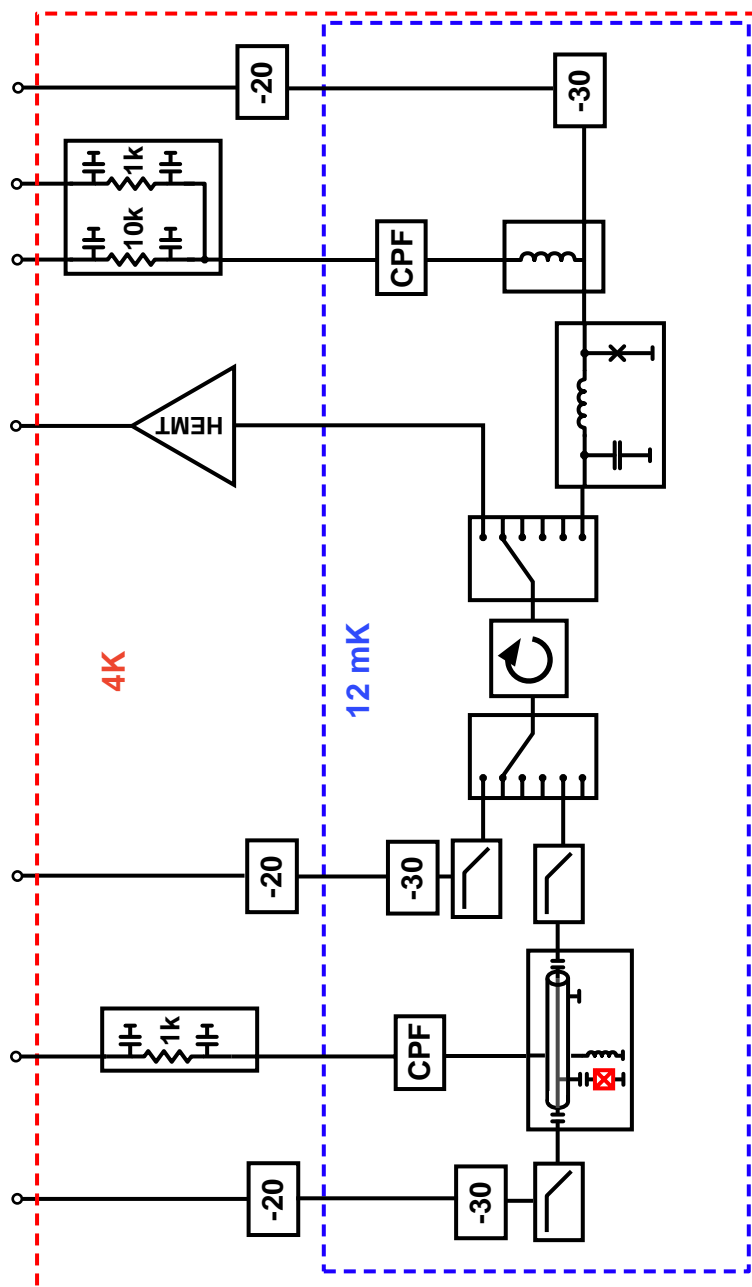
Figure 4.8: Fridge wiring diagram for the JPM-qubit readout experiment. Dashed lines represent the temperature of the fridge stages and components for the Leiden DR. Numbers in boxes correspond to attenuation in dB. Boxes marked CPF are copper powder filters.

base temperature stage using commercial SMA attenuators. The output noise temperature of a microwave attenuator of attenuation A at physical temperature T_a with input noise T_{in} is given by [116]:

$$T_{out} = \frac{T_{in} + T_a}{A} \qquad (4.4)$$

Therefore, with $50\,\mathrm{dB}$ of total attenuation, the $300\,\mathrm{K}$ noise from the room temperature electronics will be attenuated to $3\,\mathrm{mK}$ at the qubit input. DC bias lines are filtered using a lowpass LC filter at the $4\,\mathrm{K}$ stage made by inserting a wirewound axial resistor into a brass block[7], which also acts as a current source for the low-impedance JPM bias and qubit flux bias. These lines are further attenuated using a copper powder filter (CPF) [14] to thermalize the lines and prevent any microwave feedthrough to the JPM or qubit from the bias circuitry. For the JPM, since the fast DACs used to quickly pulse the junction potential into resonance with the microwave field cannot source enough current to properly bias the junction, the fast pulse current bias is summed with a slower DC bias using a homemade bias tee. The qubit and the JPMs are connected through two 6-position microwave relays, which allow for different devices to be connected without having to open the fridge. This also allows us to separately characterize the JPMs using an input calibration microwave line, and characterize the qubits using a heterodyne measurement with a cryogenic high electron mobility transistor (HEMT) amplifier, which has $30\,\mathrm{dB}$ of gain.

---

[7]The capacitance comes from the coaxial capacitance between the resistor and the channel drilled into the brass, which is at ground.

4.3.2 Room-Temperature Electronics

The room temperature electronics which control and read out the experiment are diagrammed in Figure 4.9. The cornerstone of the measurement set-up is a custom electronics rack based on circuits developed by the Martinis group at UCSB [3, 77]. The microwave portion of the rack consists of two two-channel 14-bit, $1\,\text{GHz}$ digital to analog converters (DACs) for arbitrary waveform generation, and a dual channel 8-bit $250\,\text{MHz}$ analog to digital converter (ADC) for heterodyne qubit measurement. For JPM control, the DACs also provide the fast current pulse that sets the washboard potential slope. Because they cannot source a sufficient amount of current to get to 90% of I_c, we also use a slower DAC that operates on microsecond timescales to pre-bias the JPM. The JPM itself is read out using a zero-referenced comparator circuit which has a pre-amplifier with a gain of 1000. All of these elements can share trigger information to synchronize their operation, and are controlled and read back over an ethernet interface. For qubit operations, the control and readout signals are modulated using I/Q quadrature mixers. This allows us to control the duration, shape and amplitude of these pulses with nanosecond precision. A microwave signal is applied to the LO port of the mixers, while the DAC controls the voltage at the I and Q ports, giving an output signal [116]:

$$V_{\text{RF}}(t) = I(t)\sin\left(\omega_{\text{LO}}t\right) + Q(t)\cos\left(\omega_{\text{LO}}t\right) \tag{4.5}$$
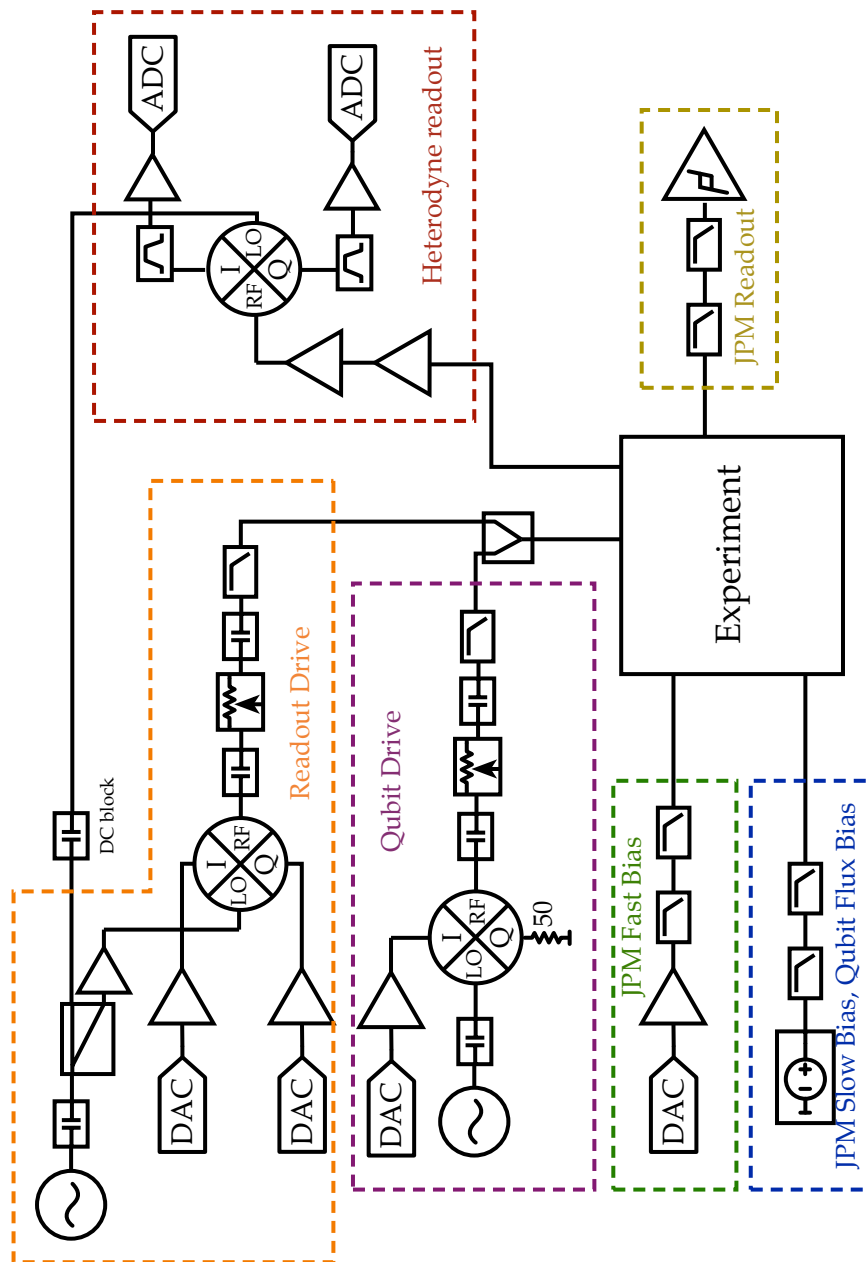
Figure 4.9: Diagram of the room temperature electronics used to control the qubit, and read it out using both heterodyne and JPM techniques.

By applying low frequency sine and cosine signals at a sideband frequency f_{SB} to the quadrature ports, an output signal at $f_{LO} - f_{SB}$ will be generated[8]. The output signal is read out using homodyne detection using the same LO oscillator as the readout drive. The amplified signal from the fridge is downconverted by a mixer, and the two quadrature components digitized by the ADC. The ADC is able to either record $I(t)$ and $Q(t)$ for later demodulation in software, or use its onboard FPGA to demodulate and pick out the signal at the sideband frequency. The qubit drive signal is generated in a similar fashion, and teed into the qubit readout resonator input port using a $3\,\text{dB}$ commercial Wilkinson power divider at room temperature. For convenience, we use USB-controlled LabBrick attenuators to set the appropriate readout and qubit control microwave powers. While convenient, we have noticed that these attenuators generate a considerable amount of digital switching noise, so it is important to use a copious amount of DC blocks and low pass filters in the microwave signal chain, especially before and after the attenuators. In general, since the JPM is a DC device, one must take great care to hunt down and eliminate any ground loops in the measurement set-up, as well as heavily filter control lines and short those which are not in use.

4.3.3   Measurement Software

The data acquisition software used to read out the electronics controlling the qubit and JPM is diagrammed in Figure 4.10. The centerpiece is custom code written in the Python language that accepts input from the user in the form of a Python

---

[8]With some leak through at $f_{LO} + f_{SB}$ and f_{LO} which can be filtered out.
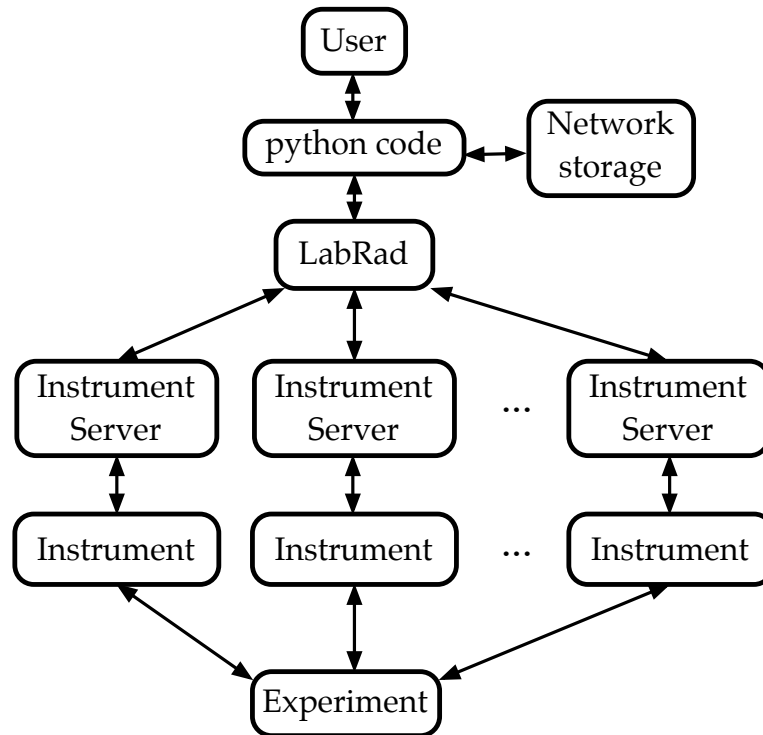
Figure 4.10: Schematic of the measurement control and data-acquisition software. Arrows indicate flow of controls and data.

script that specifies the type of measurement that is to be conducted, automatically assigns variables to the appropriate instrument, and organizes and saves sweep data to the UW-Madison network attached storage for later analysis. Our hardware interface has been greatly simplified by standardizing on the *LabRAD* protocol, which uses a distributed, asynchronous framework for instrument control and data acquisition. More information about LabRAD can be found in Markus Ansmann's thesis [3] or on the LabRAD github page[9].

The simple, binary output of the JPM-qubit measurement results made manual

---

[9]`https://github.com/labrad`

optimization of the readout parameters tedious, especially as we often had to adjust both JPM and qubit parameters at the same time. For example, to optimize the JPM readout fidelity requires the fine tuning of 9 parameters. Two describe the state of the JPM: the junction bias current and the amount of time it is left in the active, shallow-well state. Seven more describe the readout process itself: the duration, amplitude and frequency of the readout cavity drive and qubit π pulses, and the relative delay between the JPM bias pulse and the cavity readout. To avoid lengthy scans over all of these parameters, many of which depend on each other, we turned to the methods of numerical optimization to more efficiently sample the experimental parameter space. We used the Covariance Matrix Adaptation Evolution Strategy (CMA-ES) algorithm to optimize for maximum readout contrast in our measurement. CMA-ES is an advantageous algorithm as it is fast, robust against noise, and requires no knowledge of the underlying function that is being optimized or its derivatives. While a description of this evolutionary algorithm is beyond the scope of this work, the reader is referred to the tutorial by Hansen [61]. It remains to be seen whether for the JPM readout optimization using CMA-ES is the best algorithm out of the class of derivative-free optimization algorithms for multivariate noisy functions.

5 THE JOSEPHSON PHOTOMULTIPLIER: EXPERIMENT

Now we turn to our experimental characterization of the JPMs fabricated using the techniques presented in the preceding chapter. The devices studied all have $500\,\mu m^2$ junctions with critical current density $J_c \approx 40\,A/cm^2$. They have an input LC matching network with inductance $L = 200\,pH$ and capacitance $C = 4.5\,pF$. Devices were measured at $12\,mK$, the base temperature of our dry dilution refrigerator.

5.1   Voltage-Current Characteristic
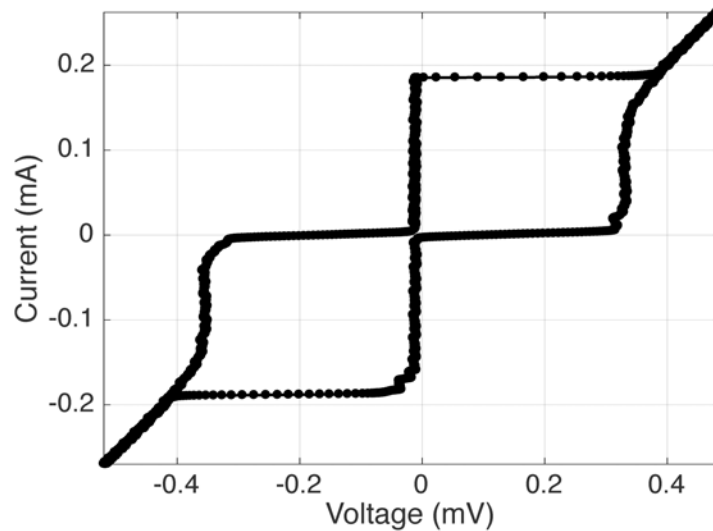
Figure 5.1: IV curve for a JPM cooled to $12\,mK$. Ground resistance due to wiring has been subtracted off.

The first step in characterizing a JPM is to measure its current-voltage (IV)

curve when cooled to well below the $1\,\mathrm{K}$, the transition temperature of aluminum. We do this via a three-wire measurement through the two bias resistors that are teed together at the $4\,\mathrm{K}$ stage of the refrigerator. A typical IV curve is plotted in Figure 5.1, showing the characteristic structure of a Josephson junction IV with both supercurrent and normal branches. The critical current of the junction can be computed from the slope of the normal branch and the relation

$$I_c = \frac{\pi}{4}\frac{2\Delta}{e}\frac{1}{R_N} \tag{5.1}$$

which for this junction gives a critical current of $I_c = 195\,\mathrm{\mu A}$ or a critical current density of $J_c = 39\,\mathrm{A/cm^2}$. Note also that the sub-gap resistance is large, indicating a high-quality tunnel barrier.

5.2 Microwave Measurements

5.2.1 Bias Pulse Sequence

After checking that the junction has survived the fabrication process, and has the correct critical current density, the next step in bringing up the JPM measurement is determining the correct bias amplitudes for both the fast and slow bias. The pulse sequence that is used in JPM operation is shown in Figure 5.2. Using the slow bias line, we first pulse the JPM bias current to a value $I_\mathrm{B} \approx 0.9 I_c$ for a duration $t_\mathrm{B} = 100\,\mathrm{\mu s}$. This is a purely technical necessity, as the DAC that supplies the fast bias cannot source enough current to bias the junction to the correct level. After this pre-
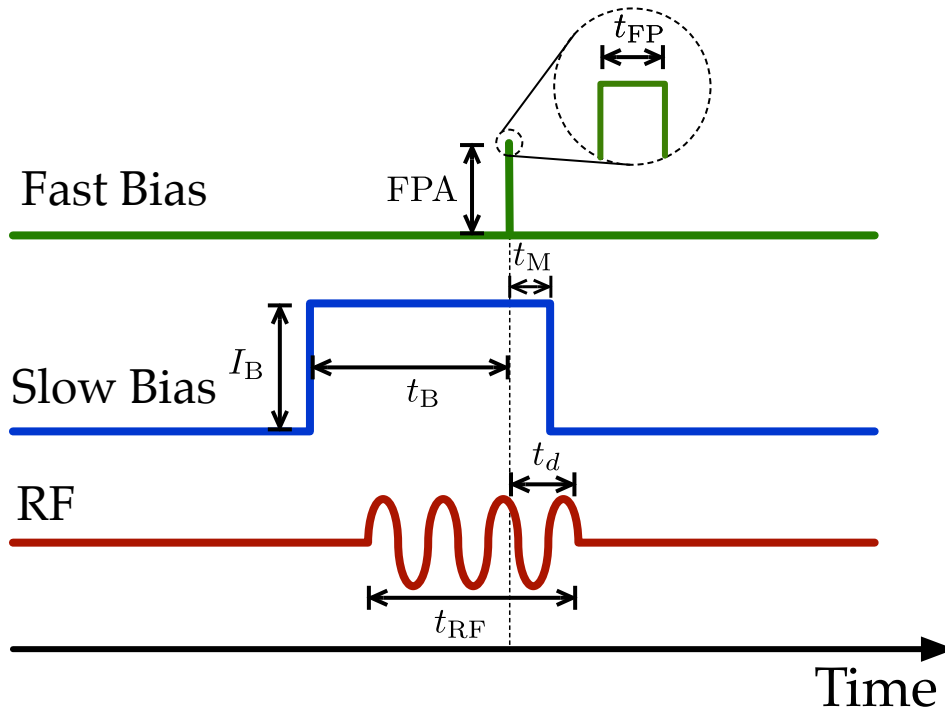
Figure 5.2: Timing diagram for bias pulses used in JPM operation, showing the fast bias, slow bias, and RF drive lines. This diagram shows a pulsed RF measurement; the same JPM bias pulse sequence is used during a CW microwave measurement.

biasing, the fast bias sends down a short current pulse of duration $t_{\text{FP}} \approx 10 - 100\,\text{ns}$ of amplitude FPA (Fast Pulse Amplitude) which brings the JPM into resonance with the incident microwave field. During this pulse and for a period of time $t_{\text{M}} = 5\,\mu\text{s}$ following it, the comparator circuitry measures the junction voltage for a JPM switching event. The slow bias current is then brought back to 0 to reset the junction, and we wait a time $t_{\text{init}} \sim 500\,\mu\text{s}$ before the next measurement. For a pulsed RF measurement, we can also vary the duration of the RF pulse and the delay between the RF pulse and the fast pulse. Alternatively, we can also perform a continuous wave microwave measurement where the junction is continuously

irradiated by incident photons.

5.2.2 S-Curves

Since the amount by which the fast pulse is attenuated as it travels to the junction is not perfectly known, we set the fast pulse amplitude by measuring switching probability as a function of fast pulse amplitude with no applied RF drive. We call the resulting curve, plotted in Figure 5.3a, the *S-curve* for the junction. We use these curves to set a bias which gives a dark switching probability of around 10%, which corresponds to dark tunneling rates $\Gamma_d \approx P_d/t_{\text{FP}} \sim 5\,\text{MHz}$ for $t_{\text{FP}} = 20\,\text{ns}$, a reasonable operating point. This setting is typically stable from day to day, although we have found we need to recalibrate it occasionally, especially if we make any modifications to the room temperature electronics. These changes are likely caused by small changes in DC offsets in the measurement set-up. We have found that the JPM switching probability is especially sensitive to these, and they must be ruthlessly eliminated.
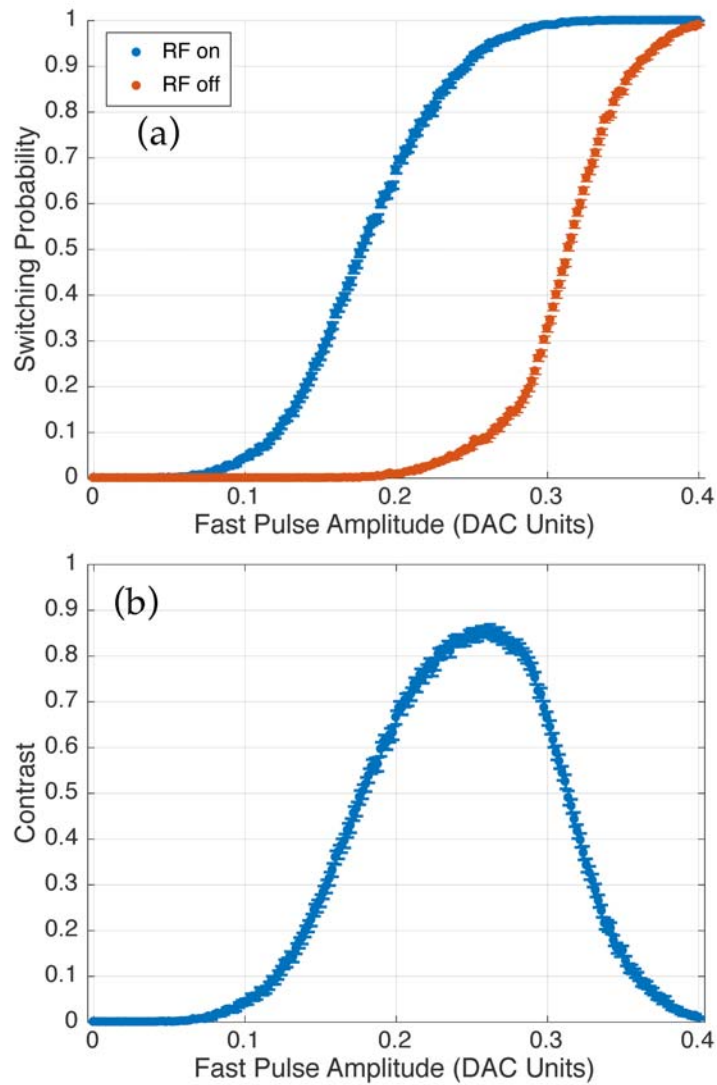
Figure 5.3: (a) S-curves of switching probability vs. fast pulse amplitude for a JPM with $t_{FP} = 20$ ns when either irradiated on-resonance with a power corresponding to approximately 10^4 photons arriving at the JPM during the measurement interval (blue points) or with no RF drive (red points). Each point represents 4020 repetitions of the experiment. (b) Contrast calculated from the data in (a).

5.2.3 Error on JPM Measurements

A quick note on the calculation of errors for measurements with the JPM. Since the result of a JPM measurement is binary, either a switch or no switch, the errors can be calculated from the binomial distribution. Since the number of repetitions is large (typically $N \approx 2000$ or more), it is appropriate to approximate the error with the normal distribution [139] and we write for the standard deviation:

$$\sigma = \sqrt{\frac{P(1-P)}{N}} \tag{5.2}$$

where P is the measured switching probability. Following the usual rules for propagation of uncertainty, the errors in contrast and quantum efficiency are given by:

$$\sigma_C = \sqrt{\sigma_b^2 + \sigma_d^2} \tag{5.3}$$

$$\sigma_\eta^2 = \frac{1}{n_{\text{photon}}} \left(\frac{\sigma_b^2}{(1-P_b)^2} + \frac{\sigma_d^2}{(1-P_d)^2} \right) \tag{5.4}$$

The error bars for the results plotted in this thesis represent a 95% confidence interval from 1.96σ.

5.2.4 Initialization Time

We find that the time between experimental repetitions, which we term the "initialization time" t_{init} has a large effect on the measured switching probability. The effect of increasing increasing initialization on measured dark switching probability
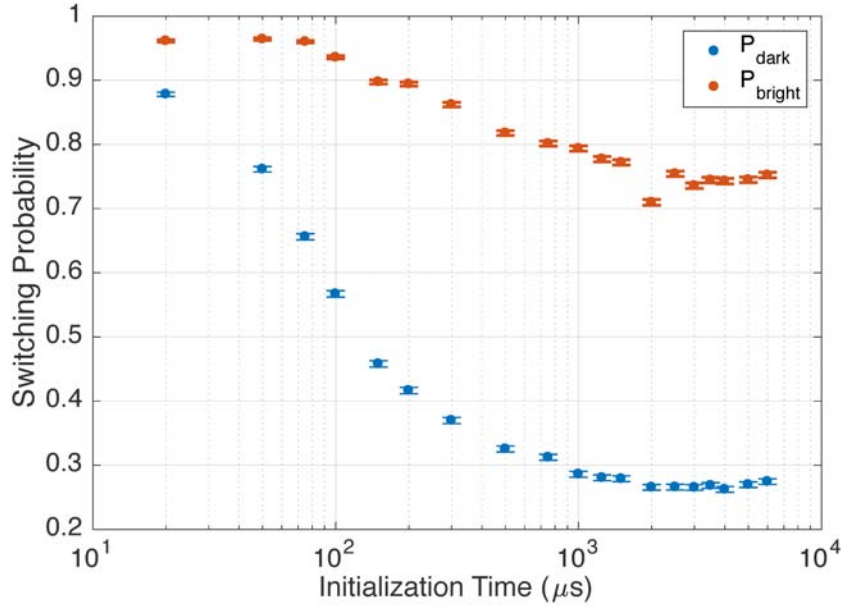
Figure 5.4: Dark switching probability for a JPM with varying initialization times with both applied microwave drive and no applied microwave drive. Each point represents 10020 repetitions.

is shown in Figure 5.4. The switching probability decays roughly exponentially with increasing time between experiments with a time constant $\tau_b^{-1} \approx 500\,\mu s$ and $\tau_d^{-1} \approx 120\,\mu s$. This is clear evidence that one junction switching event can enhance the probability that the junction switches during the following repetitions. The long timescales involved suggest that quasiparticles generated during the switching event are affecting the JPM junction, as they have been measured to have lifetimes on the order of milliseconds [99, 91, 149]. Practically, we operate the JPM with an initialization time $t_{\text{init}} > 1\,ms$ to ensure successive measurements are independent. This $1\,kHz$ repetition rate could be improved by adding normal metal quasiparticle traps near the Josephson junction [85].

5.2.5 RF Response

Once a good operating point for the JPM fast pulse amplitude has been deter-
mined by measuring the dark S-curve, we can begin to measure its response to a
microwave drive. Typically we begin by applying a continuous drive instead of
modulating the RF to simplify the initial experiments, although this is not a vital
point. The effect of applying an RF drive can be seen in Figure 5.3a. We see a clear
enhancement of the switching probability, caused by the resonant activation of
the junction state. The corresponding contrast is plotted in Figure 5.3b, reaching
values of over 80%. These measurements, performed through the calibration line,
do not benefit from an accurate calibration of the photon power that is delivered to
the junction. While we can account for explicit loss from the attenuation we have
deliberately inserted into the signal path, as well as that added by other microwave
components the loss due to the normal metal coaxial cable in the fridge cannot be
characterized. Additionally, we do not know the loss from microwave disconti-
nuities, such as that caused by the aluminum wirebond onto the chip [109]. It is
well known that wirebonds add approximately $1\,\mathrm{nH/mm}$ of excess inductance. At
$5\,\mathrm{GHz}$, this corresponds to $30\,\Omega$ or a reflection coefficient $|\Gamma| = 0.3$. Despite this, we
simply use the known attenuation and room temperature drive power to estimate
the photon number at the junction from:

$$n_{\mathrm{JPM}} = \frac{P}{\hbar\omega} t_{\mathrm{FP}} \tag{5.5}$$

Based on a total attenuation of $100\,\mathrm{dB}$, a room temperature drive of $13\,\mathrm{dBm}$ and a fast pulse time of $20\,\mathrm{ns}$, we estimate that 10^4 photons are arriving at the JPM during the time it is active.

The response versus both frequency and bias for a different device is plotted in Figure 5.5a, for a similar photon number and $t_{\mathrm{FP}} = 10\,\mathrm{ns}$. We see a broad response centered around $5\,\mathrm{GHz}$, which gets broader as the fast pulse amplitude is increased towards the critical current. This is due to the $|g\rangle$ to $|e\rangle$ transition being broadened as the JPM excited state approaches the top of the potential well barrier. As a comparison, we calculate the junction quantum efficiency using the input output theory descrited in section 3.3 and from it the contrast using the equation:

$$C = e^{-\Gamma_g t_{\mathrm{FP}}} \left(1 - e^{-\eta n_{\mathrm{JPM}}} \right) \tag{5.6}$$

This contrast is plotted in Figure 5.5b, and is in qualitative agreement with the measured contrast. One significant difference is the presence of notches spaced by approximately $100\,\mathrm{MHz}$ in the experimental contrast data. These are likely due to standing waves in the microwave cabling, due to impedance mismatches. This illustrates the JPM's extreme sensitivity to input impedance mentioned in section 3.3.4. While we take every precaution to minimize any potential source of mismatch as well as the total length of cable, some level of standing waves is inevitable unless an attenuator is placed directly on the input connector on the JPM box. This is not a realistic solution as we cannot afford to lose any photons between the measured qubit and the JPM.
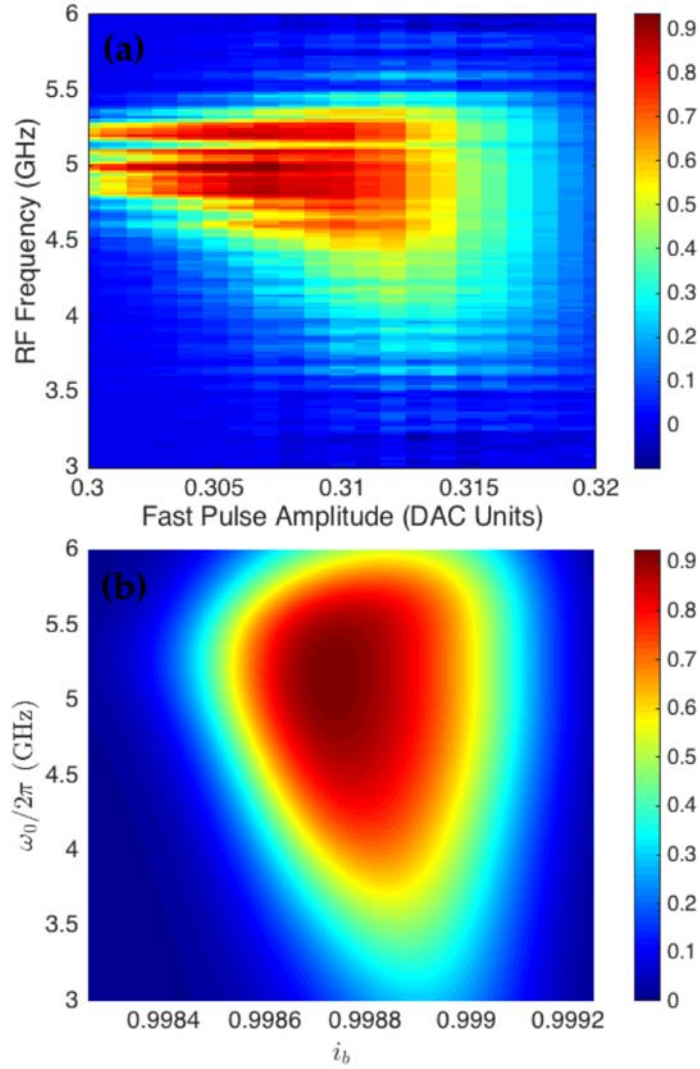
Figure 5.5: (a) Plot of JPM contrast versus both fast pulse amplitude and applied RF frequency during a CW measurement. Fast pulse time is $10\,\mathrm{ns}$ and the applied microwave power corresponds to $\sim 10^4$ photons during the measurement time. Each point corresponds to 1020 experiment repetitions. (b) Calculated contrast using the input-output theory described in section 3.3.

5.2.6 Cavity Drive
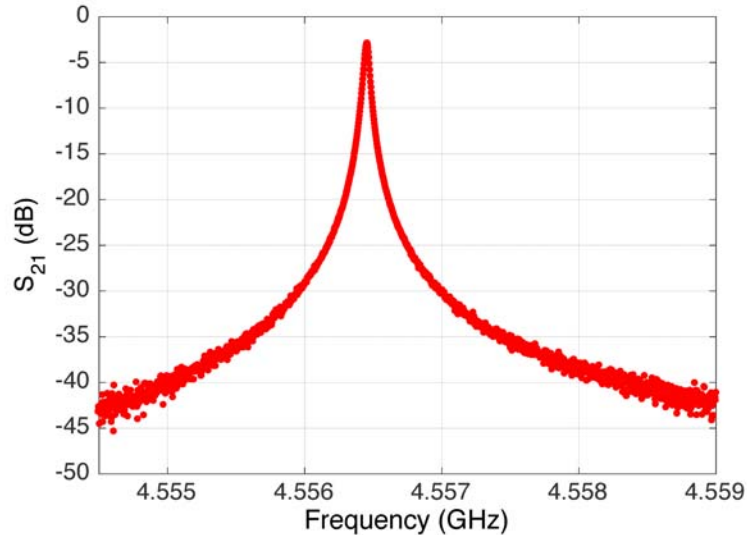
Figure 5.6: Transmission through high quality Nb on intrinsic silicon CPW cavity, measured using a HEMT amplifier at $4\,\mathrm{K}$.

As a precursor to the JPM qubit readout experiments descrited in the next chapter, we decided to drive the JPM through a linear, high-quality microwave cavity instead of a transmon readout resonator. The cavity was a $\lambda/2$ coplanar waveguide resonator with equal input and output interdigitated capacitors. It was fabricated on a high-quality intrinsic silicon substrate from dry etched thin film niobium. To prevent reduction in the resonator's intrinsic quality factor Q_i by magnetic vortices [136, 113] or quasiparticles generated by infrared radiation, it was measured in a mu-metal can coated with an IR-absorbing material [105, 98]. The S_{21} transmission spectrum of the resonator is shown in Figure 5.6. The measured center frequency is $f_0 = 4.5565\,\mathrm{GHz}$ with width $\Delta f = 45\,\mathrm{kHz}$ for a loaded $Q = 1 \times 10^5$. We extract a coupling [54] $Q_c = 1.4 \times 10^5$ and a $Q_i = 3.5 \times 10^5$. The evolution of

this cavity occupation as a function of drive frequency is straightforward; for more details, see appendix B. For a drive of strength a_0 and length t_d, the amplitude of coherent state formed inside the cavity is given by

$$\alpha(\Delta = 0) = -\frac{ia_0}{2}t_d \tag{5.7}$$

for zero detuning $\Delta = \omega_0 - \omega_d$. For non-zero-detuning, the cavity state is

$$\alpha(\Delta) = -\frac{a_0}{2\Delta}\left(e^{i\Delta t_d} - 1\right) \tag{5.8}$$

We measure the cavity state by driving the cavity for a variable time at different drive detunings, and turning on the JPM measurement at the end of the cavity drive. The resulting switching probability is plotted in Figure 5.7. The photons in the cavity leak out towards the JPM at a rate $n_{JPM} = n_{cav}\kappa$, where $n_{cav} = |\alpha|^2$ and $\kappa \equiv 2\pi\Delta f$. The JPM switching probability is therefore a direct probe of the size of the coherent state in the cavity. As we expect from eq. (5.8), the number of photons oscillate sinusoidal at a frequency equal to the cavity-drive detuning. It should be noted that this data was taken with a photon counter that did not have an input matching network. Along with the small κ, which limits the rate at which photons escape from the resonator, we used a large amplitude drive which put on the order of 10^4 photons in the cavity.
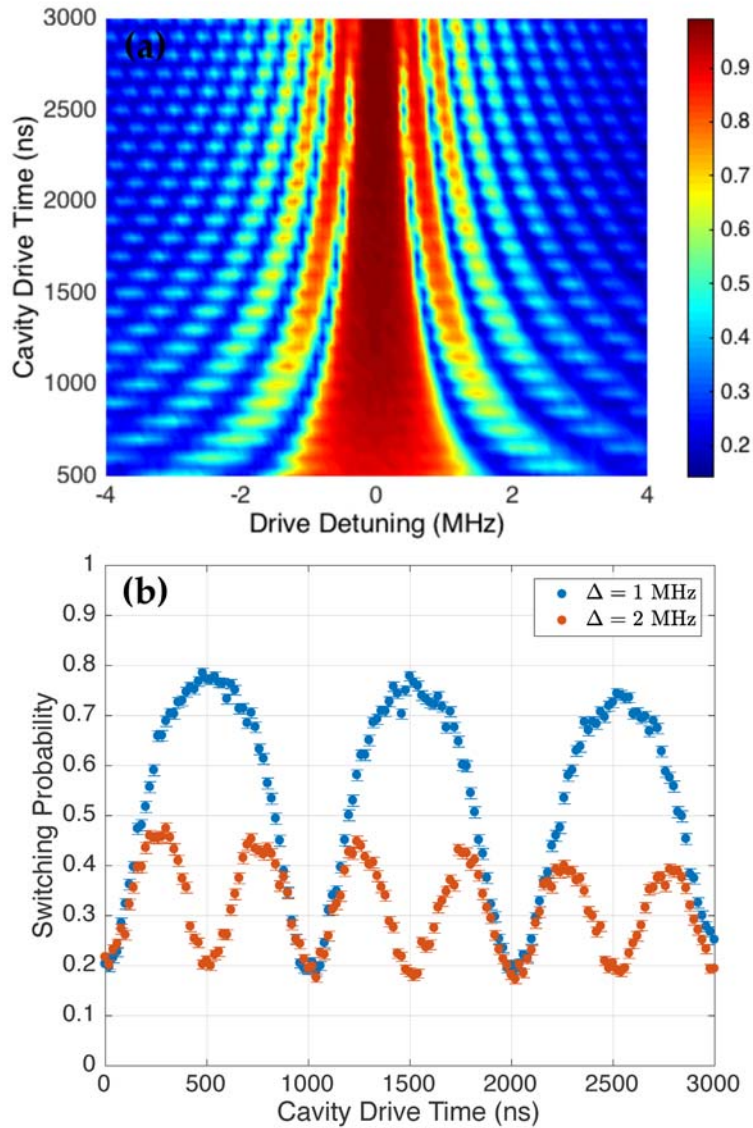
Figure 5.7: (a) JPM switching probability as a function of cavity drive time and cavity drive detuning. JPM Fast pulse time is $10\,\text{ns}$ at a bias level corresponding to $P_d = 0.1$. (b) 1-D cuts through (a) for different values of the detuning.

5.3 Calibrating Photon Number

In order to accurately estimate the quantum efficiency of the photon counter and properly benchmark its performance, we need a calibrated source of photons as close as possible to the JPM. Fortunately, the transmon qubits we are measuring provide just such a calibrated source. The Jaynes-Cummings Hamiltonian, eq. (2.38) which descrites the qubit-resonator circuit has an interaction term

$$\hat{H}_{\text{int}} = \hbar\chi\hat{\sigma}_z\hat{a}^\dagger\hat{a} \tag{5.9}$$

This term can be interpreted as a cavity-state dependent shift of the qubit frequency [16, 17], similar to the atomic Stark shift. By measuring this Stark shift for different drive powers, we can map from room RF pulse amplitude to cavity occupation. A separate measurement of the cavity width (or photon decay rate) κ gives us everything we need to know to calculate the photon flux at the JPM. This technique is similar to that used in [96] to measure the quantum efficiency of a traveling wave amplifier.

5.3.1 Stark Shift Measurement

The pulse sequence used for the Stark shift calibration is shown in Figure 5.8. A long (longer than the cavity decay time to ensure it is in the steady state) pulse is first applied at the resonator frequency in order to populate the cavity. After this pulse, we perform a qubit spectroscopy measurement (see section 6.3.2 for more details) in order to measure the Stark-shifted qubit transition frequency f_{01}.
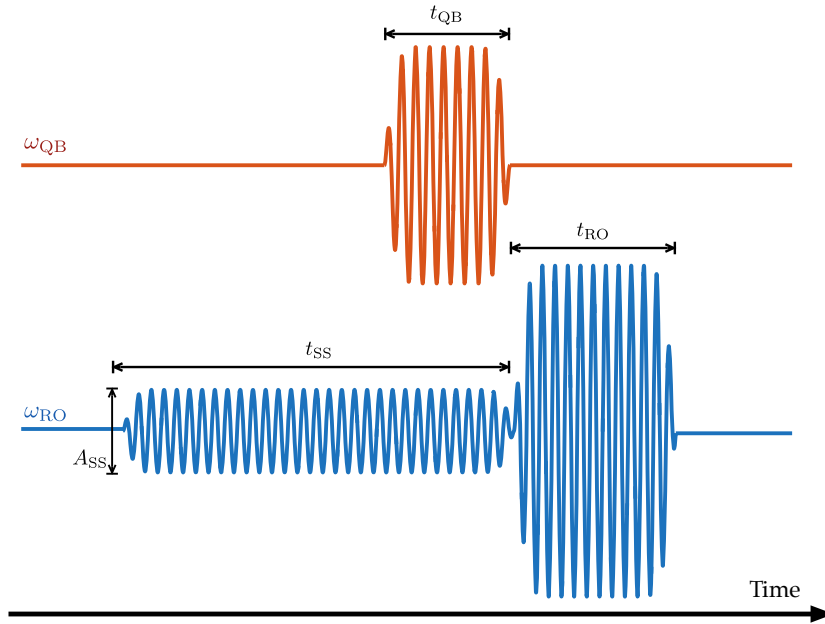
Figure 5.8: Diagram of the Stark shift measurement pulses applied at the cavity readout ω_{RO} and qubit drive ω_{QB} frequencies.

Once the Stark shift $\Delta f_{10} = f_{10}(A_{\mathrm{SS}}) - f_{10}(A_{\mathrm{SS}} = 0)$ has been extracted, we use the theory of Boissoneault *et al.* [18] to extract the cavity occupation. We model the qubit as a three level system, with a design anharmonicity $\alpha = -300\,\mathrm{MHz}$. From the measured low-power qubit chi shift χ_0 and the qubit-cavity detuning Δ_0, we can calculate the two Stark and Kerr coefficients [64]:

$$
\begin{aligned}
S_0 &= -\chi_0 + \frac{1}{4}(-\chi_0\lambda_1^2 + 3\chi_1\lambda_0^2) - g_0^{(2)}\lambda_0^{(2)} \\
S_1 &= \chi_0(1 - \lambda_1^2) - \chi_1(1 - \lambda_0^2) - 2\chi_0\lambda_0^2 \\
K_0 &= \frac{1}{4}(\chi_0\lambda_1^2 - 3\chi_1\lambda_0^2) - g_0^{(2)}\lambda_0^{(2)} \\
K_1 &= (\chi_1 - \chi_0)(\lambda_1^2 + \lambda_0^2)
\end{aligned}
\tag{5.10}
$$
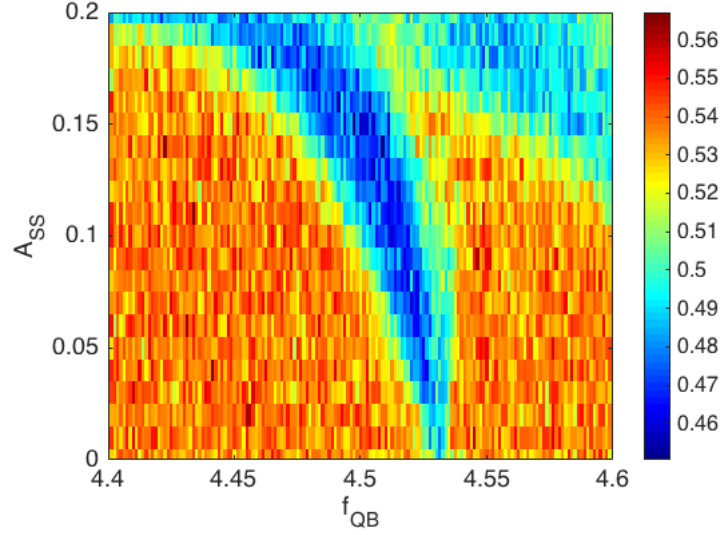
Figure 5.9: Switching probability vs. f_{QB} and A_{SS}, expressed in the output value of the DAC used to gate the readout IQ mixer, for qubit sample MW072.

where $\lambda_i = -g_{i+1,i}/\Delta_i$, $\chi_i = g_{i+1,i}^2/\Delta_i$, $g_0^{(2)} = \lambda_0\lambda_1(\Delta_1 - \Delta_0)$ and $\lambda^{(2)} = -g_0^{(2)}/(\Delta_0 + \Delta_1)$. With these coefficients, the shift in the qubit transition frequency is given by:

$$\Delta f_{10}/2\pi = (S_1 - S_0)n_{\mathrm{cav}} + (K_1 - K_0)n_{\mathrm{cav}}^2 \tag{5.11}$$

Since the voltage at the IQ mixer quadrature port controls the amplitude of the wave, fit the Stark shift using:

$$n_{\mathrm{cav}} = \beta A_{SS}^2 \tag{5.12}$$

where β is the unknown relation between the readout drive amplitude and cavity population. The fit for two different qubits (MW072 and MH060)[1] is presented in Figure 5.10, showing good agreement with the theory. This analysis does incorrectly

---

[1]Syracuse University die naming convention.
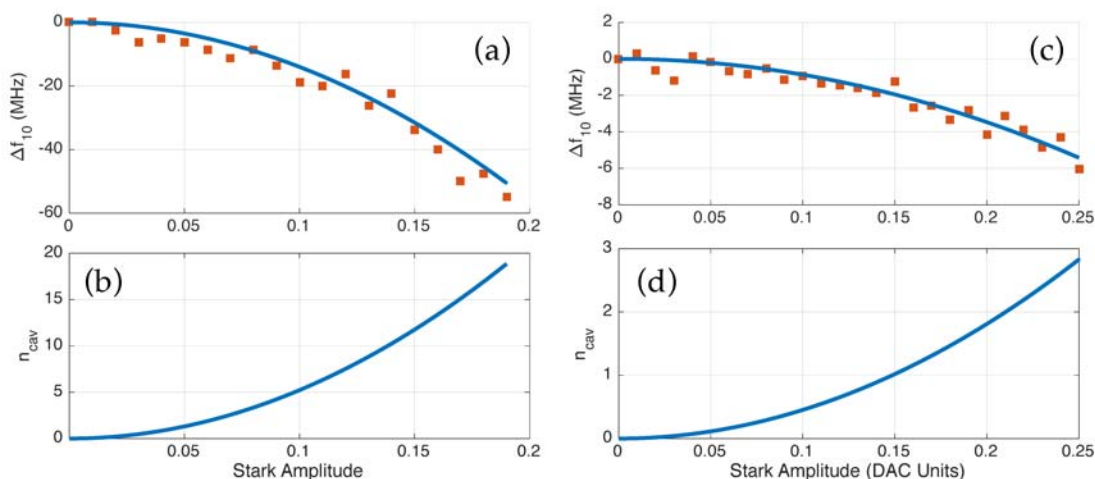
Figure 5.10: (a-b) Fit of Stark shifted qubit frequency Δf_{10} versus Stark shift amplitude A_{SS} and extracted cavity photon occupation for qubit MW072. The fit gives $\beta = 540$. (c-d) Fit of Stark shift Δf_{10} versus A_{SS} and extracted cavity photon occupation for qubit MH060. The fit gives $\beta = 46$.

assume that the dressed readout cavity frequency does not shift with power as the photon number increases. In reality, the dressed state of the cavity approaches the bare frequency as the cavity occupation approaches the critical photon number [18, 13]. This situation is analyzed further in appendix B.

5.3.2 Cavity Ringdown

The final piece of information needed to perform an *in-situ* calibration of the number of photons reaching the JPM during a measurement is the cavity κ. For the asymmetrically coupled cavities of the measured transmons, $\kappa_{\text{in}} \ll \kappa_{\text{out}} \approx \kappa$,

and the photon flux at the JPM is given by:

$$\lambda = n_{\mathrm{cav}}\kappa \tag{5.13}$$

While in principle we could measure κ using a HEMT amplifier and a microwave transmission measurement, it is better to directly measure κ using the JPM. This is because the readout resonator's output coupling is dependent on the impedance of the circuit at the output, and there is no guarantee that this will be the same between the two measurements. To measure κ, we simply drive the readout cavity until it
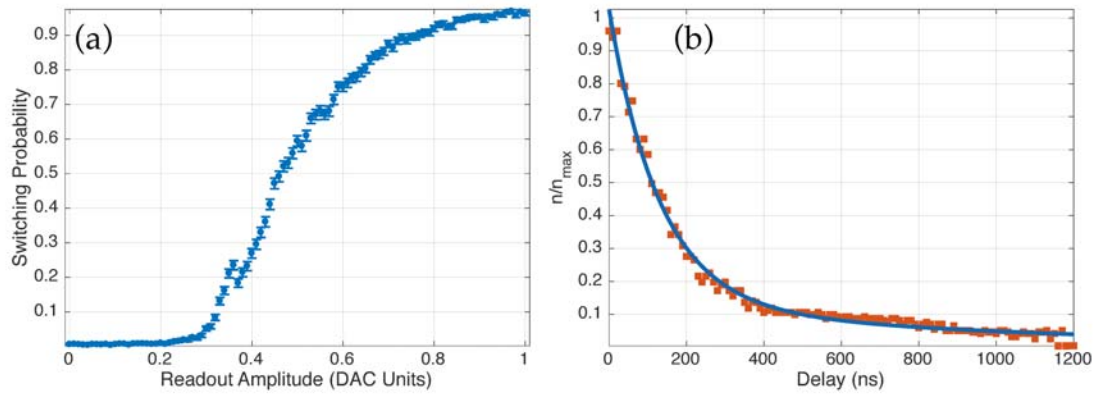
Figure 5.11: (a) Measured P_b as a function of readout drive amplitude. (b) Normalized extracted photon number as a function of measurement delay (red squares) fit to an exponential (blue line), giving $\kappa = 7.6\,\mathrm{MHz}$

reaches a steady state photon population, and measure the switching probability as a function of the time between the end of the cavity drive and the measurement. A correction must be made for the nonlinear response of the JPM to input drive, as shown in Figure 5.11a. Using the P_b vs. amplitude data and the Stark shift calibration, we fit the computed photon number to a decaying exponential to

determine κ in Figure 5.11. Although the cavity state is not constant during the JPM active time, $\lambda t_{\text{FP}} \ll 1$ so the simple exponential assumption is justified.

5.4   Quantum Efficiency Measurement

Using the calibrated photon flux from the previous measurement, we can measure the quantum efficiency by measuring the bright and dark switching probabilities. We measure the bright switching probability after applying a saturating pulse to the readout cavity to ensure it is in the steady state, and continue to drive the cavity during the JPM bias to ensure a constant flux of photons at the JPM. We plot quantum efficiency versus both fast pulse time and fast pulse amplitude in Figure 5.12, calculated using Equation 3.7. The area in the upper right of the plot is where we assign $\eta = 0$ because the junction always switches regardless of the applied microwave drive. This measurement was performed at the qubit readout resonator frequency of $4.9889\,\text{GHz}$, and a photon flux of $\lambda = 1\,\text{ns}^{-1}$. To facilitate comparison with the theory of chapter 3 we fit the measured dark rate to an exponential and plot η versus time and dark rate in Figure 5.13. We see large regions of parameter space where quantum efficiency is at the few percent level, for reasonable values of both t_{FP} and Γ_d. We see a region of larger quantum efficiency for junction biases with very shallow wells, where $\eta > 0.1$. It should be noted however that this is not a region of practical interest as the dark rate is too high, which would degrade contrast to unusable levels.
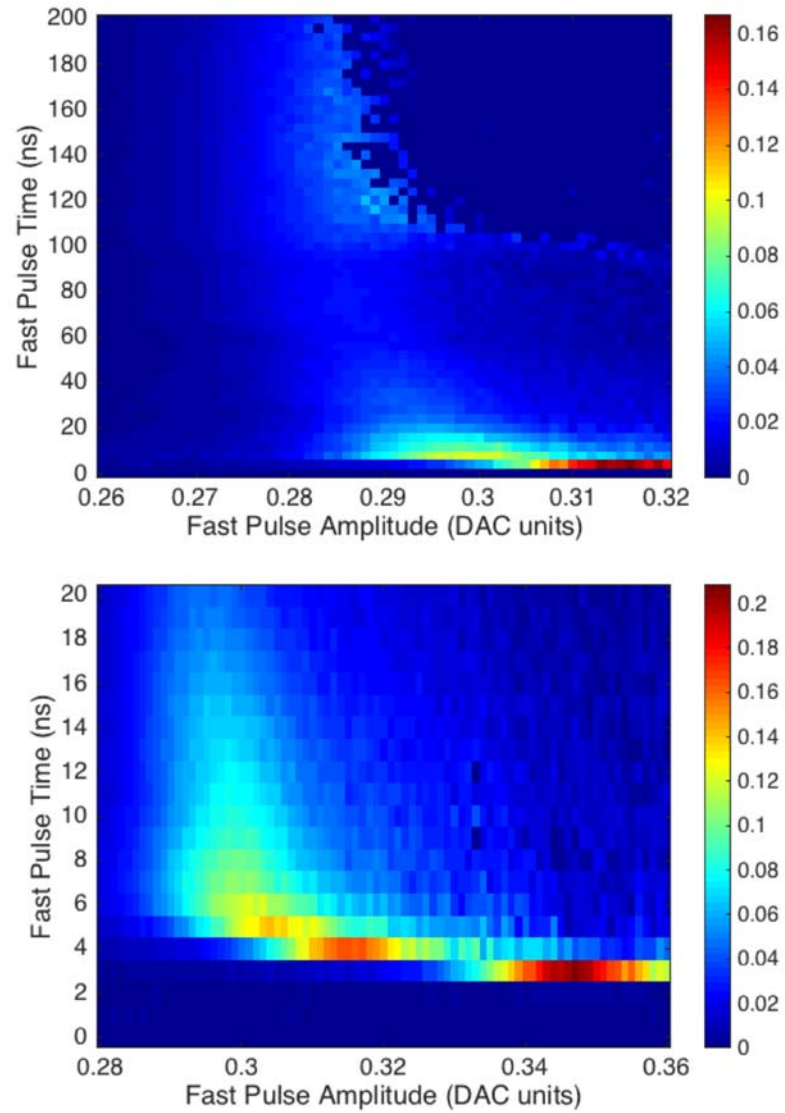
Figure 5.12: Measured quantum efficiency η as a function of fast pulse amplitude and fast pulse time. Photon flux is $\lambda = 1\,\text{GHz}$, and each point represents 8000 repetitions.
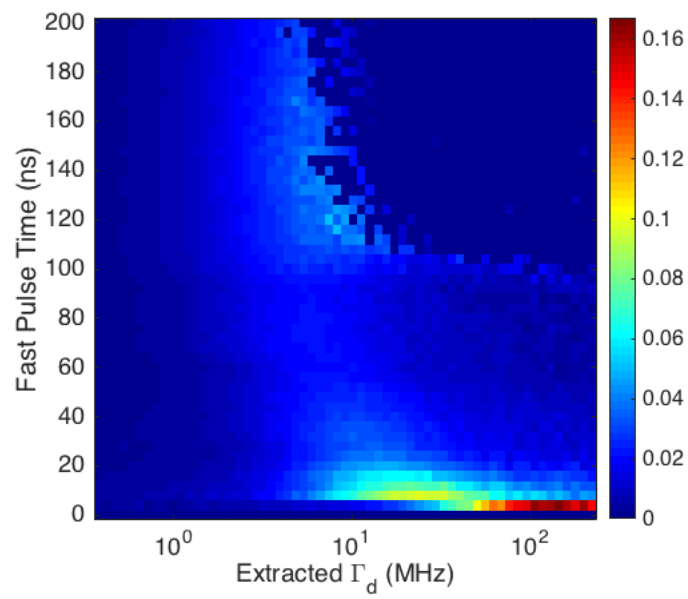
Figure 5.13: Measured quantum efficiency η as a function of fast pulse time and fitted dark switching rate Γ_d. Same measurement as Figure 5.12a.

5.4.1 JPM Figure of Merit
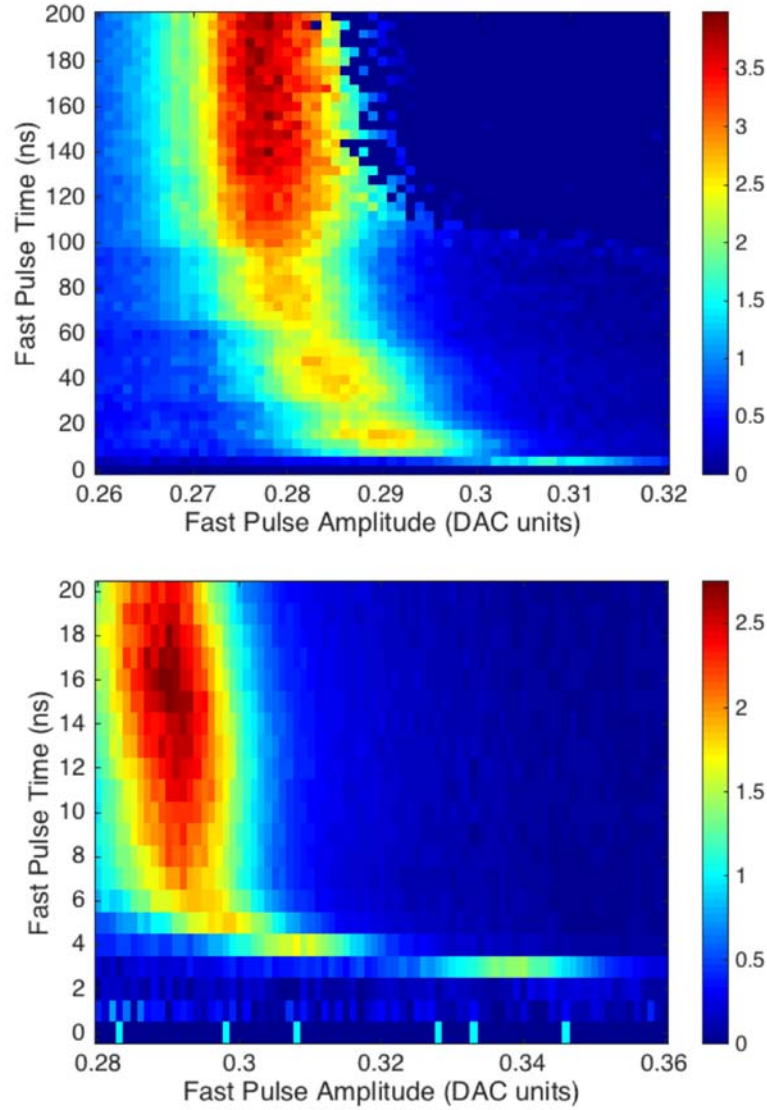
Figure 5.14: Measured α as a function of fast pulse amplitude and fast pulse time. Same measurement as fig. 5.12a.

To better illustrate this, we next plot the JPM figure of merit $\alpha = \eta\lambda/\Gamma_d$, discussed in subsection 3.2.3. Surprisingly, α can be calculated without knowledge of the

number of photons present during the measurement:

$$\alpha = \frac{1}{\log{(1 - P_d)}} \log{\left(\frac{1 - P_b}{1 - P_d}\right)} \tag{5.14}$$

We plot α as a function of fast pulse time and fast pulse amplitude in Figure 5.14. As expected, this makes the tradeoff between quantum efficiency and dark rate apparent: the optimal dark rate is near $4\,\mathrm{MHz}$. This is not surprising, as this was the range of parameters for which the input matching network was designed. The figure of merit plateaus at around $\alpha = 4$. We can use this value to estimate the achievable contrast and thus fidelity in a qubit measurement. Assuming a critical photon number of $n_{\mathrm{crit}} = 100$ and an output coupling $\kappa = 20\,\mathrm{MHz}$, both reasonable values for a transmon design, we calculate a maximum achievable contrast of 53% at an optimal time of $100\,\mathrm{ns}$. As we shall see, this is reasonably close to the values we achieve in the qubit readout experiment.

5.4.2 Comparison to Theory

Finally, we compare these results to the input-output theory model developed in section 3.3. Rates and JPM transition energies are calculated with the complex scaling method of appendix A. The measured η is considerably less than the theoretical prediction assuming no extra sources of loss between the cavity and junction. The agreement is much better if we assume there is some loss between the cavity and junction. This is not unreasonable, as there is a significant amount of cabling and other microwave hardware (coaxial relays, microwave isolator) in between the
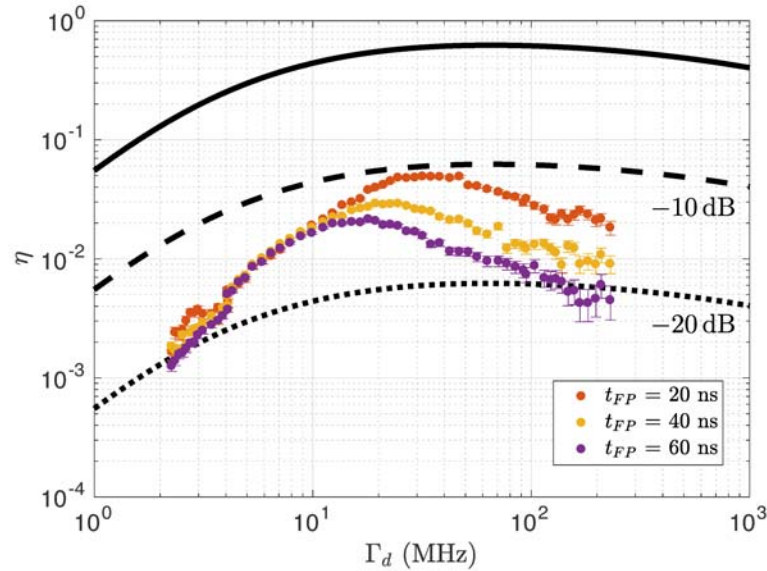
Figure 5.15: Measured quantum efficiency for three different values of $t_{\rm FP}$ compared to that calculated from input-output theory. The solid line is the quantum efficiency with no additional loss; dashed lines are quantum efficiency with $10\,\rm dB$ and $20\,\rm dB$ of loss between the cavity and JPM.

two chips. Room temperature measurements of this loss show a total attenuation of $2.7\,\rm dB$; additional loss could come from poor microwave transitions in the sample box wire bonds and microwave connectors. The input-output theory also does not correctly capture the shape of the measured quantum efficiency curve. This is likely due to the fact that it is a simple model that only considers a steady-state switching rate for the junction and does not incorporate several effects which are probably relevant. These include the increase in tunneling rate caused by dissipative elements connected to the junction as well as the broadening and eventual disappearance of the junction excited state as the tunneling rate is increased. Furthermore, it also does not take into account any thermal population of the junction excited state,

which is likely to play a role in enhancing the dark tunneling rate.

6   QUBIT MEASUREMENT WITH THE JPM

In this chapter, we discuss our efforts to read out a transmon qubit with the Josephson photomultiplier. We will not describe the readout of a transmon using conventional heterodyne techniques, as this is a well-studied system. For more details, the reader is encouraged to consult David Hover's thesis [64]. We do, however, present an analysis of the qubit readout resonator response as a function of drive power in appendix B. The experimental set-up is pictured in Figure 4.8. It should be emphasized that for the data presented in this chapter we do include a microwave isolator between the qubit and JPM. For these preliminary experiments, we wanted to ensure that the classical backaction on the qubit which comes from the JPM switches to the voltage state was minimized. The isolator provides $18\,\mathrm{dB}$ of isolation between the two chips, and also has the advantage of being a good $50\,\Omega$ termination for the qubit. All measurements were done at the base temperature of our dry dilution refrigerator, at a temperature $T_{\mathrm{mix}} \approx 12\,\mathrm{mK}$.

6.1   Qubit Design

The transmon qubits we use in this experiment are of a standard design, pictured in Figure 6.1. They are made by our collaborators at Syracuse University at the Cornell Nanofabrication Facility. The qubit design is similar to the one described in [137] and [30]. The qubit ground plane, capacitor, and readout resonator are fabricated from thin film niobium sputtered on a high-resistivity intrinsic silicon wafer. The qubit self-capacitance comes from two large floating electrodes which
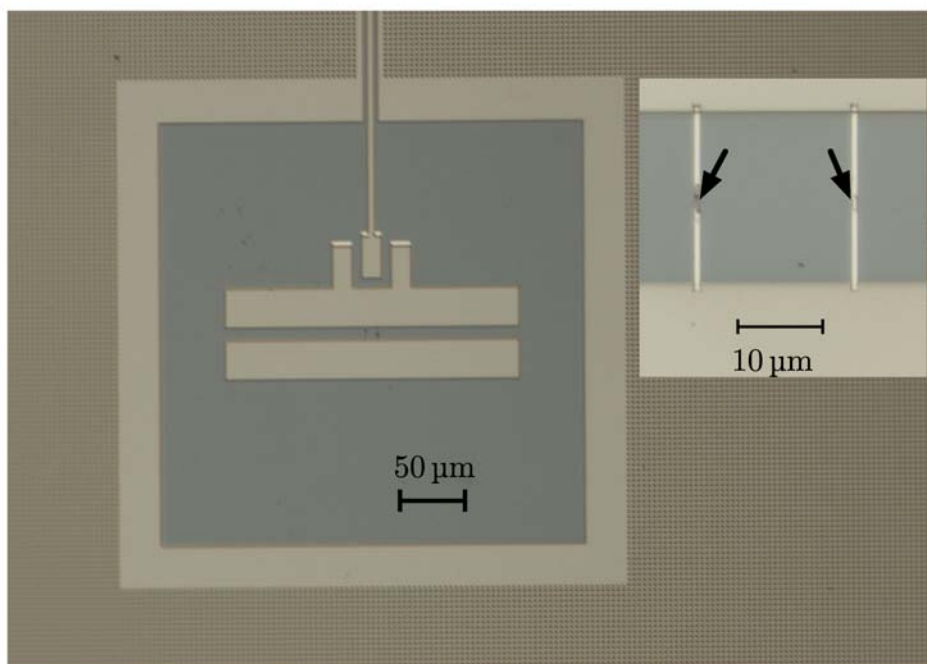
Figure 6.1: Micrograph of qubit design used for the measurements in this chapter, showing the two electrodes that are capacitively coupled to the readout resonator. Inset: The two aluminum Josephson junctions (indicated by arrows) that form the qubit SQUID loop.

are capacitively coupled to the voltage antinode of a $5\,\mathrm{GHz}$ $\lambda/2$ coplanar waveguide readout resonator. One particularity of this design is that the coupling to the resonator is asymmetric: to ensure that most of the photons in the cavity leak out towards the JPM the output coupling capacitor $C_\mathrm{out} \approx 7\,\mathrm{fF}$ is larger than the input coupling capacitor $C_\mathrm{in} \approx 2\,\mathrm{fF}$. The sub-micron qubit junctions are Al-AlO$_x$-Al, and fabricated with a Dolan-bridge technique using e-beam lithography [44, 48]. The two junctions are in a SQUID geometry with a 2:1 asymmetry that reduces sensitivity to flux noise and doubles the number of flux-bias sweet spots [137, 150]. The design parameters for the qubit are $E_C = 300\,\mathrm{MHz}$ and $E_J/E_C \approx 40$ so that

the qubit frequency $\omega_{01}/2\pi \approx 4\,\mathrm{GHz}$. The qubit we will focus on in this chapter has designation MH060.

Flux tuning of the qubits is provided by an external flux bias coil, mounted in the lid of the sample box. The coil is made from 50 turns of 36AWG copper magnet wire wrapped around the teflon insulation of a flange mount SMA connector, with a diameter of $4.1\,\mathrm{mm}$ and a length of $6\,\mathrm{mm}$. The end of the coil is located approximately $1\,\mathrm{mm}$ over the center of the qubit chip. Using standard formulae for the field outside of a solenoid [69], we estimate a mutual inductance of $1.3\,\mathrm{pH}$ between the bias coil and the SQUID loop. As the coil has a DC resistance of less than $1\,\Omega$, we use an external $1\,\mathrm{k}\Omega$ resistor at $4\,\mathrm{K}$ as a current source which is further filtered using a copper powder filter mounted at the dilution refrigerator cold stage.

6.2   Photon Counting cQED Readout

The theory of photon counter based readout with the JPM has been investigated by Govia in *et al.* [56, 58]. The basic idea is simple: we generate a cavity pointer state whose amplitude depends on the state of the qubit. In the case where the cavity linewidth is small, this is easy; we need to drive at one of the dispersed cavity frequencies. The amplitude of the on-resonant state eq. (6.1) will grow linearly in time, while the amplitude of the off-resonant Equation 6.2 state will describe a
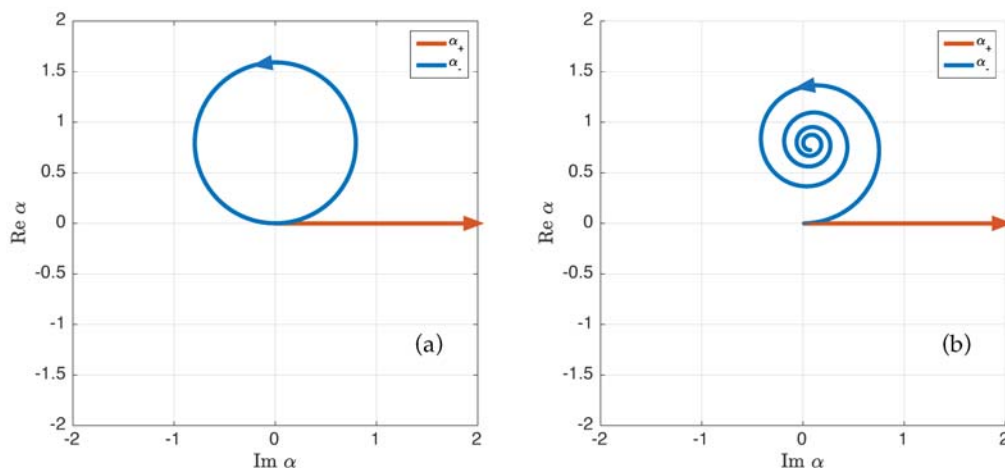
Figure 6.2: (a) Cavity pointer state evolution for $\kappa = 0$ in the cavity frame. (b) Cavity pointer state evolution for $\kappa = 5\,\mathrm{MHz}$ in the cavity frame. For both plots, $\epsilon = 10\,\mathrm{MHz}$, $\Delta/2\pi = 500\,\mathrm{MHz}$ and $\chi/2\pi = 2\,\mathrm{MHz}$.

circle in the IQ plane:

$$\alpha_{|0\rangle} = -\frac{\epsilon}{4\chi}\left(e^{2i\chi t_m} - 1\right) \tag{6.1}$$

$$\alpha_{|1\rangle} = -\frac{i\epsilon}{2}t_d \tag{6.2}$$

where ϵ is the drive strength. The trajectory of the states in the IQ plane (rotating at the cavity frame) is plotted in Figure 6.2a. To return the off-resonant cavity state to vacuum we wait a time $t_d = \pi/\chi$. As shown in Figure 6.2b, the situation is complicated by photons leaking out of the cavity at a rate κ. Instead of describing a circle in the IQ plane, the off-resonant state spirals towards a point away from the origin. This degrades the contrast between the two pointer states. To restore contrast we could apply a strong, fast reset pulse to the cavity to drive the off-resonant state

back to the origin. Another potential solution is to implement a tunable output coupler that can turn off the output during the drive [132, 153]. The qubit pointer state generation process is described in more detain in Appendix B, where we also show that for maximum contrast we should operate in the regime $\kappa = 4\chi$. This readout protocol can also be extended to two and four qubit parity measurements, which are useful for measuring stabilizers in the surface code [57].

6.3 Dispersive Measurement

Once the JPM bias has been chosen using the method of subsection 5.2.2, we are ready to begin the qubit measurement. In this section, we will go through the process of measuring a transmon qubit in the dispersive limit. We first take spectroscopy data on the qubit cavity as a function of readout drive power and qubit flux bias. We then do spectroscopy on the qubit to find its transition frequency, and using this knowledge we can perform rotations on the qubit to initialize it into a known state, which allows us to measure the fidelity of the JPM measurement.

6.3.1 Cavity Spectroscopy

The first step in characterizing the transmon is to spectroscopically probe the readout resonator in order to determine the dispersive shift of the cavity. For cavity photon populations $\bar{n} < n_{\text{crit}}$, the qubit in the ground state shifts the bare resonance of the cavity ω_r:

$$\omega_r - \omega^{|0\rangle} = \frac{g_{10}^2}{\Delta_0} \tag{6.3}$$
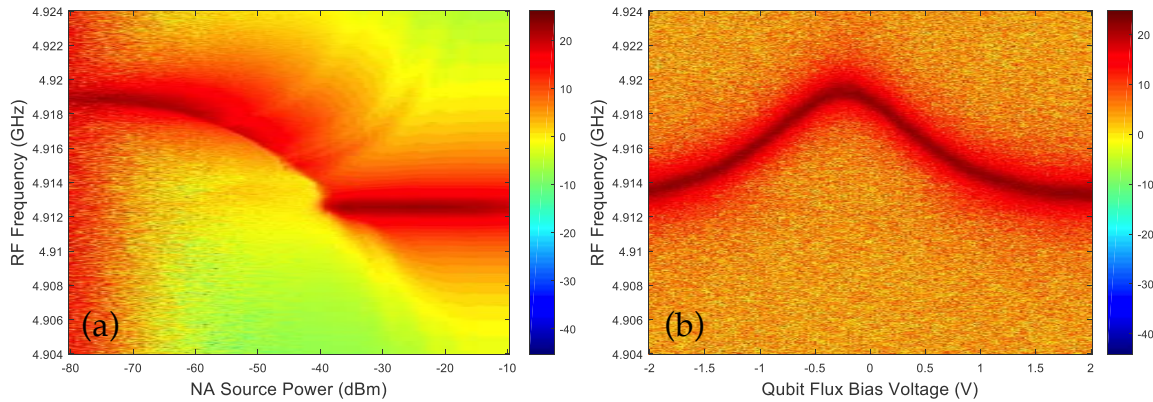
Figure 6.3: Response of the qubit readout cavity when measured with a vector network analyzer (NA). (a) Readout cavity frequency as a function of applied readout power. (b) Readout cavity frequency as a function of qubit flux bias, at a network analyzer power of $P_{\mathrm{NA}} = -65\,\mathrm{dBm}$.

where $\omega^{|0\rangle}$ is the cavity frequency when the qubit is in the $|0\rangle$ state, g_{10} is the qubit-cavity coupling, and $\Delta_0 = \omega_{10} - \omega_r$ is the cavity-qubit detuning. This relation is only approximate as the cavity pull is modified by the presence of higher qubit levels beyond the $N = 2$ approximation; however, for sufficiently low powers the true shift χ is well approximated by χ_0. At large cavity populations $\bar{n} \gg n_{\mathrm{crit}}$ the qubit-cavity coupling becomes highly nonlinear and the readout resonator behaves as if there were no qubit [18, 120]. By measuring the cavity frequency at high and low powers we can therefore extract χ_0. For convenience, and as a simple test of the health of the qubit, we perform this measurement by connecting the qubit to the HEMT amplifier at $4\,\mathrm{K}$ and measuring S_{21} using a vector network analyzer (VNA). Figure 6.3a shows the result of this so-called "punch-out" spectroscopy, with a measured $\chi_0/2\pi = 5.1\,\mathrm{MHz}$. From the direction in which the cavity shifts as we reduce the readout power, we can tell that $\Delta_0 < 0$, which is helpful for qubit

spectroscopy. We can repeat this measurement using the JPM, varying the readout power using the programmable attenuators on the resonator readout line. The cavity response measured with the JPM is plotted in Figure 6.4a, where for clarity the switching probability is normalized to its maximum for each measured power. As we expect, as we reduce the number of photons in the cavity, the JPM contrast is reduced. We can also measure the response of the cavity as a function of qubit flux bias, which is plotted Figure 6.3b. The flux bias tunes the Josephson energy E_J and therefore the frequency of the qubit.
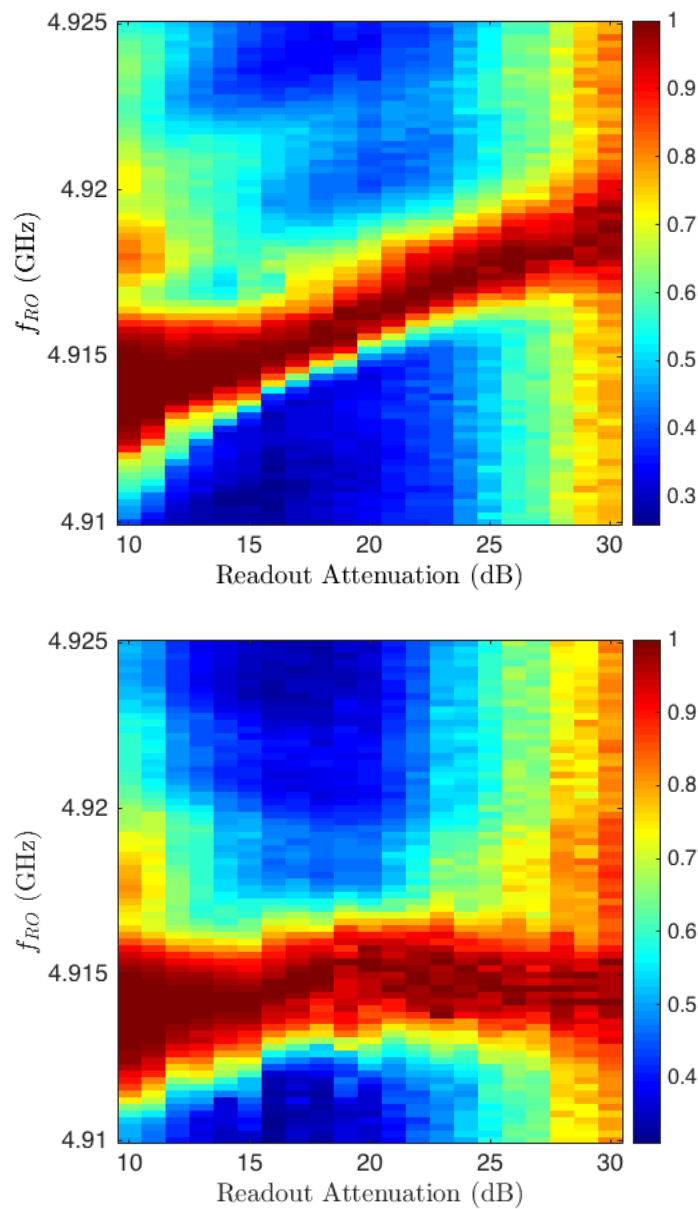
Figure 6.4: Cavity response as a function of readout drive power measured with the JPM with (a) no qubit drive pulse (b) a qubit π-pulse. For clarity, the switching probability for each power is normalized to the maximum probability at that power. Each point represents 5040 repetitions.

6.3.2 Qubit Spectroscopy
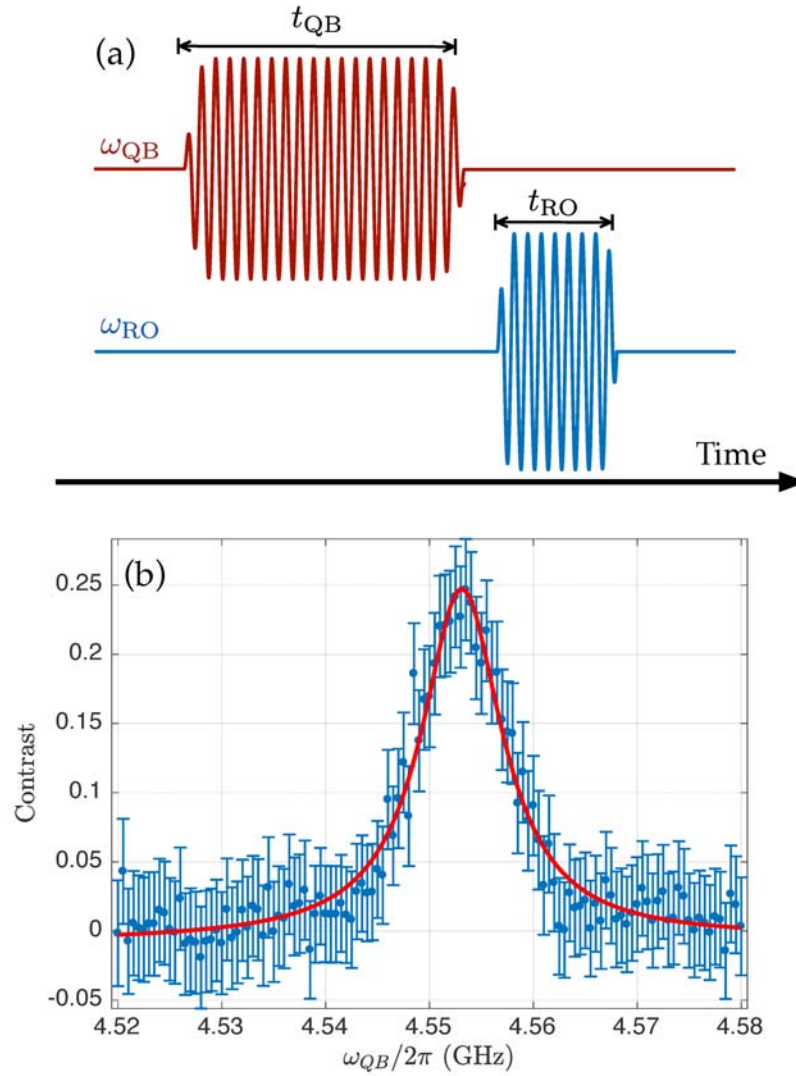
Figure 6.5: (a) Sequence diagram for qubit spectroscopy measurement. ω_{RO} is the readout pulse and ω_{QB} is the qubit rotation pulse. (b) Measured JPM contrast as a function of qubit frequency. The red line is a fit to a Lorentzian.

Once we have determined the power at which the cavity shows a dispersive shift, we next find the qubit transition frequency. We set the readout frequency

such that $\omega_{\mathrm{RO}} = \omega_r + \chi_0$ (drive on the $|0\rangle$ state resonance), and the readout power such that $\bar{n} \ll n_{\mathrm{crit}}$ while still maintaining reasonable contrast. We then monitor the switching probability as we sweep the qubit drive pulse's frequency. The pulse sequence for this measurement is shown in Figure 6.5a. We choose the length of the qubit spectroscopy tone $t_{\mathrm{QB}} > T_1 \sim 1\,\mu\mathrm{s}$ so that the pulse saturates the $|0\rangle$ to $|1\rangle$ transition and drives the qubit to the mixed state $|0\rangle + |1\rangle$. We choose a measurement time $t_{\mathrm{RO}} < T_1$ short enough to avoid energy relaxation in the qubit but long enough to allow for appreciable contrast. Because this transmon design does not feature a separate qubit drive line on the chip (like, for example, the devices studied in [8]), the qubit pulse is significantly attenuated by the readout cavity. Practically, this means we must use a drive 10 to 20 dB larger than the readout pulse.

In Figure 6.5b we plot the measured contrast as a function of qubit drive frequency, which shows a clear enhancement at the qubit f_{10}. Fitting a Lorentizan to this peak, we extract $f_{10} = 4.5531\,\mathrm{GHz}$. The width of the spectroscopic qubit peak is rather large: $\Delta f_{10} = 9.4\,\mathrm{MHz}$. This indicates that our qubit is subject to a considerable amount of relaxation, which we measure through a direct measurement of the relaxation rate in subsection 6.3.4; the qubit lifetime is $T_1 \propto 1/\Delta f_{10}$. Once the qubit transition has been located, we can repeat the readout cavity spectroscopy of section 6.3.1 while also applying a qubit rotation pulse. We plot the results of this spectroscopic scan in Figure 6.4b. Immediately apparent is the fact that that $\omega^{|1\rangle} \neq \omega_r - \chi_0$; this occurs because the cavity pull also depends on the energies of the higher levels of the transmon. The difference in cavity frequency for the two qubit state preparations, seen in Figure 6.6, is twice the dispersive shift χ. From
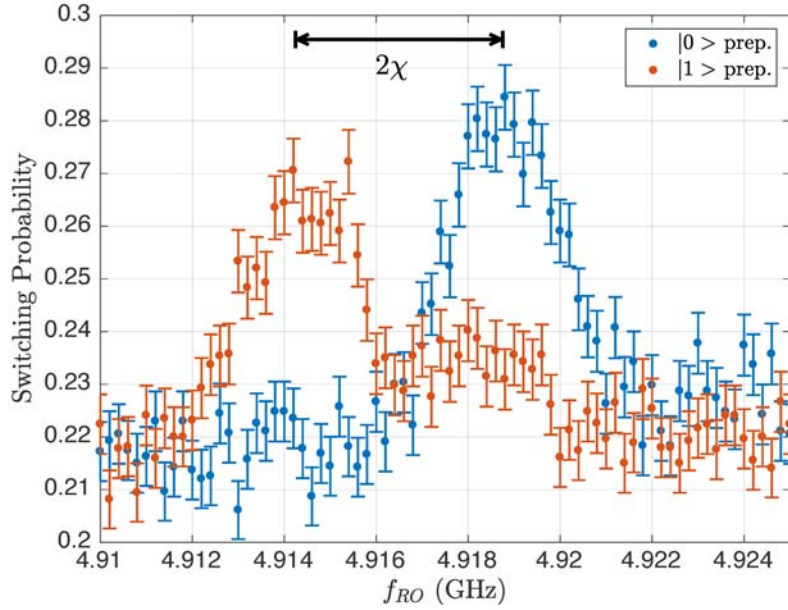
Figure 6.6: Readout cavity spectroscopy for qubit preparation in the $|0\rangle$ and $|1\rangle$ states.

this, we can also calculate the qubit dipole coupling constant g_{10}:

$$g_{10} = \sqrt{\chi \Delta_0} = 28\,\text{MHz} \tag{6.4}$$

which is consistent with the designed transmon gate capacitance. The measured χ also enters the calculation of the Stark shift, the data for which is plotted in . This also gives us a way to calculate the critical photon number: $n_{\text{crit}} = \Delta_0^2/4g_{10}^2 = 42$.

6.3.3 Rabi Oscillations

Driving the qubit at its transition frequency f_{10} induces rotations around the x or y-axes of the Bloch sphere (c.f. Figure 1.1). By varying the duration of the qubit
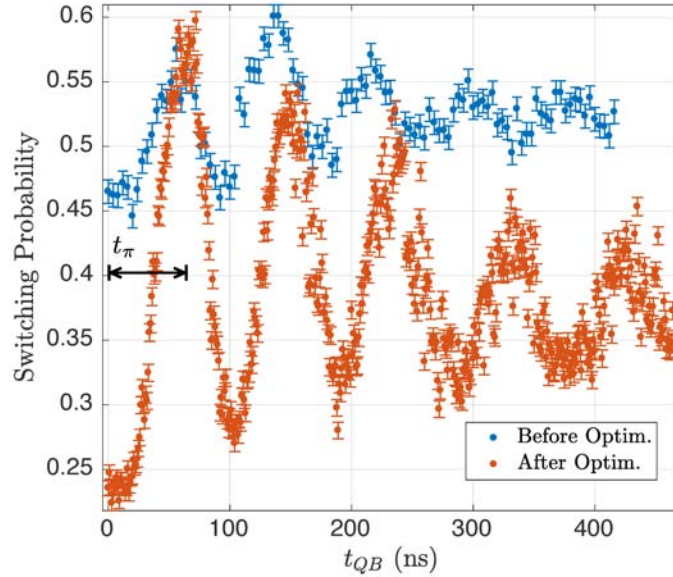
Figure 6.7: Rabi oscillation data measured both before and after we run the CMA-ES optimization on the measurement parameters. Data taken at a power corresponding to $\bar{n} = 13$ photons, with 5010 repetitions per point.

spectroscopy pulse, we can induce Rabi oscillations as the qubit state rotates from ground to excited and back again. We use these Rabi oscillations to calibrate the pulse length that will flip the qubit state from $|0\rangle$ to $|1\rangle$. Such a pulse is known as a π-pulse, since it is equivalent to a $180°$ rotation. As the drive pulse amplitude is increased, the frequency of the Rabi oscillations will increase. The speed of the π-pulse is limited by the anharmonicity of the qubit, with a minimum length $t_\pi \sim 2\pi/\alpha$ as we do not want to drive $|1\rangle \to |2\rangle$ transitions. t_π should also be kept much shorter than T_1 in order to prevent the qubit from decaying during the rotation.

Parameter Optimization

Measurement Parameters	
Qubit drive time	t_{QB}
Qubit drive amplitude	A_{QB}
Qubit frequency	f_{QB}
Qubit sideband frequency $f_{\mathrm{SB,RO}}$	
Readout time	t_{RO}
Readout amplitude	A_{RO}
Readout frequency	f_{RO}
Readout sideband frequency $f_{\mathrm{SB,RO}}$	
QB drive to readout delay	t_{QD}
Readout to JPM delay	t_{JD}
Fast Pulse Amplitude	FPA
Fast Pulse Time	t_{FP}

Table 6.1: CMA-ES Optimization Parameters

A major practical difficulty in carrying out the JPM-based qubit readout is the large number of parameters that must be adjusted in order to maximize the readout contrast. The large dimensionality of the parameter space makes it impractical to hand-tune all parameters. For this reason, we decided to use numerical optimization techniques to find the best operating point for both the qubit and JPM. We use the CMA-ES algorithm (c.f. section 4.3.3), and perform an on-line optimization on the contrast, which we define as the difference in switching probability with and without a π-pulse applied to the qubit. The effect of this optimization can be seen in Figure 6.7: we increase the visibility of the Rabi oscillations from 13% to 35%.
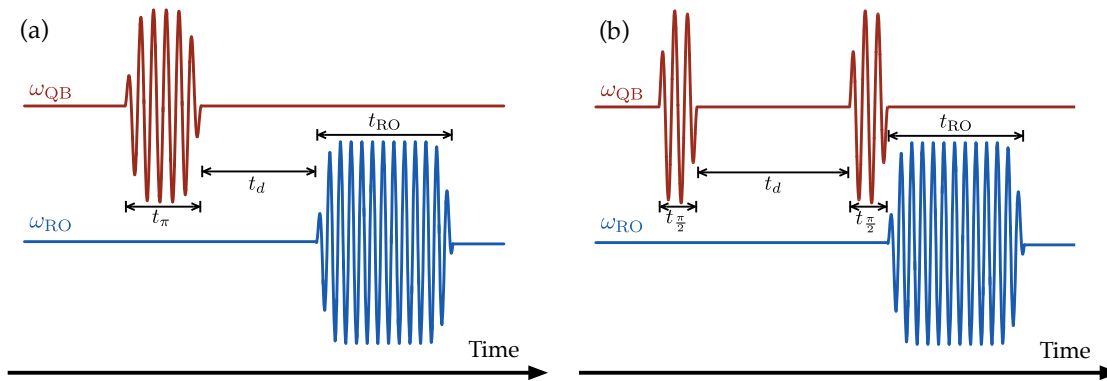
Figure 6.8: (a) Pulse sequence for a qubit T_1 measurement. (b) Pulse sequence for a qubit T_2 measurement.

6.3.4 Qubit Decoherence

It is also obvious from looking at the data in Figure 6.7 that the visibility envelope of the Rabi oscillations is decaying on a time scale of around $1\,\mu s$. Along with the broad qubit spectroscopy line, this is a second indication that the qubit we are measuring has a short coherence time. We confirm this by measuring the extent to which the qubit is subject to decoherence. Decoherence is the catch-all term that refers to all of the extraneous environmental couplings that cause the state of the qubit to drift away from its desired value. It can be thought of as a series of small perturbations to the direction of the vector on the Bloch sphere. For example, flux noise in the SQUID loop causes fluctuations in E_J and thus ω_{10} [22, 128], which is equivalent to a rotation around the z-axis. There are many other sources: hot quasiparticles [91, 26], edge and surface defects [111, 42], and dielectric loss [118, 114].

Decoherence can take two forms: relaxation and dephasing. Borrowing notation

used in NMR spectroscopy, these can be characterized by two exponential decay times T_1 and T_2. Relaxation describes processes by which the $|1\rangle$ state relaxes to the ground state $|0\rangle$, with a lifetime of T_1. T_2 is the lifetime of a state prepared on the equator of the Bloch sphere. These states are affected by both relaxation and dephasing, with an overall lifetime of

$$\frac{1}{T_2} = \frac{1}{2T_1} + \frac{1}{T_\phi} \tag{6.5}$$

We measure qubit T_1 using the pulse sequence shown in Figure 6.8a. The qubit is prepared in the $|1\rangle$ state using a calibarated π-pulse, and we wait a variable delay time t_d before measuring the state of the qubit. The result is plotted in Figure 6.9a, along with a fit to a decaying exponential from which we extract $T_1 = 760\,\text{ns}$. T_2 is measured using the pulse sequence shown in Figure 6.8b, with the data and exponential fit plotted in Figure 6.9b. The qubit is rotated onto the equator of the Bloch sphere using a $\pi/2$ pulse (length $t_{\frac{\pi}{2}} = t_\pi/2$) where it is allowed to dephase freely for a time T_2 for a time t_d. A second $pi/2$ pulse moves the state back to the z-axis for measurement. The envelope of the measured qubit state will decay with time constant T_2; any oscillations indicate a detuning of the original control pulse from ω_{10}. From an exponential fit to the data, we extract a $T_2 = 50\,\text{ns}$.

Both this T_1 and T_2 are disappointing. Similar devices, measured by our collaborators at Syracuse University have shown T_1 times in excess of $15\,\mu\text{s}$. This type of 2D transmon can have lifetimes in excess of $50\,\mu\text{s}$, as measured by the UCSB/Google group [8] and the IBM group [30]. Related 3-dimensional transmon

architectures have achieved coherence times approaching $100\,\mu s$ [124]. These low coherence times make qubit measurements tedious, as they are comparable to the JPM measurement time. As we will discuss, this also results in a significant loss of fidelity.

Where could these degraded T_1 times come from? One obvious candidate is that the junction switching to the voltage state is populating the readout resonator with photons. However, we have found that the low T_1 is not improved when increasing the repetition rate between experiments, and not significantly different when measured with a HEMT amplifier and heterodyne readout. One likely source of loss is insufficient infrared shielding of the qubit input and output ports; dedicated IR filters made using ECCOSORB, a broadband absorbing resin, have been shown to have a significant impact [10]. The design of the qubit chip itself could be an issue as well: the floating design of the qubit capacitance, as well as the lack of microwave crossovers on the chip lead to the possibility of chip modes interacting with the qubit. This could be solved through the use of microfabricated crossovers [29]. It is also probable that the off-chip flux bias coil is a problem. The coil could be poorly thermalized and as it is not superconducting; running a current through it will heat the chip. An on-chip flux bias line [137] should solve these issues. We hope that by making these improvements we will be able to increase the qubit coherence time to a reasonable level.
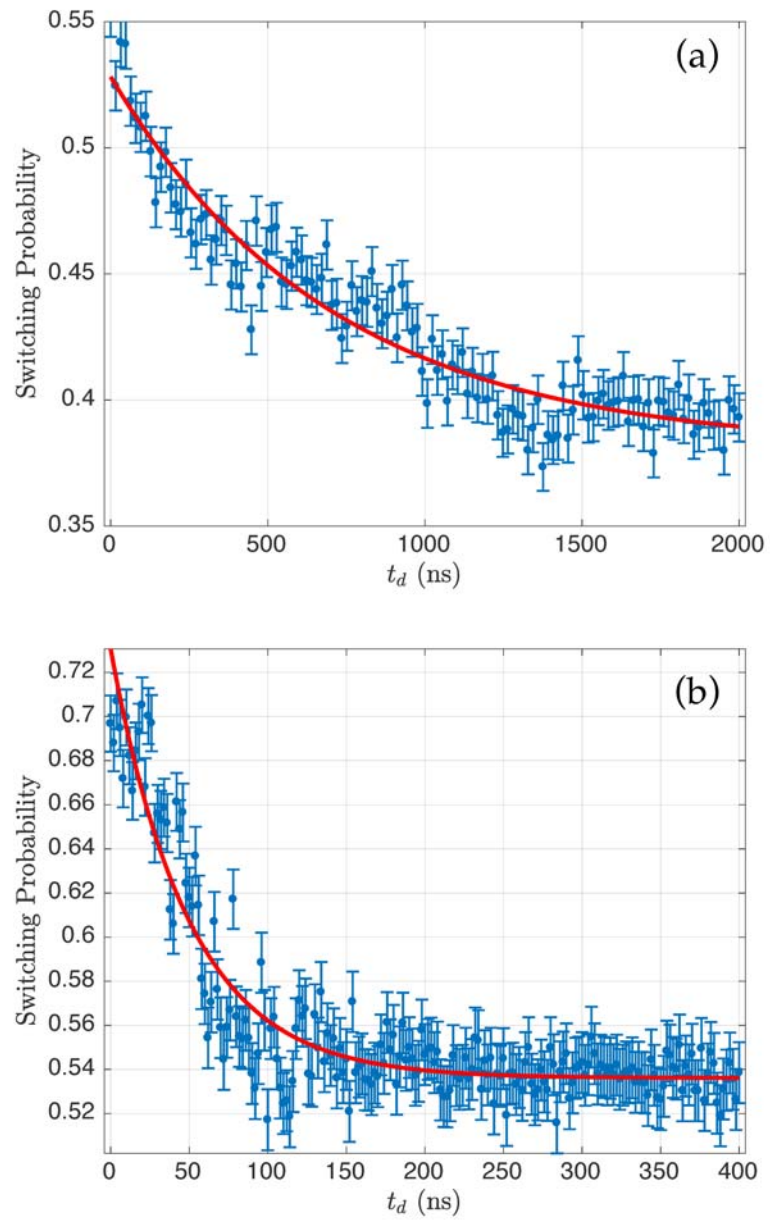
Figure 6.9: (a) Qubit T_1 measurement and exponential fit. (b) Qubit T_2 measurement and exponential fit.

6.4   Bright State Measurement
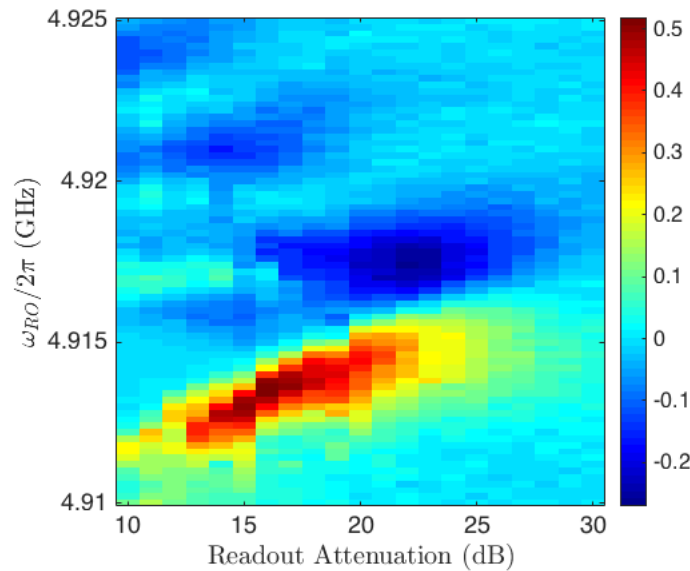
Figure 6.10: $|1\rangle$-$|0\rangle$ contrast as a function of readout cavity drive power and frequency. We perform the "bright state" readout at an attenuation of $16\,\mathrm{dB}$.

In order to increase the JPM measurement contrast and thus fidelity from the 35% observed in the dispersive regime, we decided to exploit the nonlinearity of the Jaynes-Cummings Hamiltonian. As was first observed by the Yale group [120], for $\bar{n} > n_{\mathrm{crit}}$ the transmission through the cavity can have a highly transmitting "bright state" depending on the qubit state. We review the theoretical understanding of this regime in appendix B. While this measurement is not QND, it is highly advantageous for the JPM measurement as the contrast is extremely dependent on the number of photons which reach the cavity and therefore the cavity population. The power needed to perform this bright state readout can be found by measuring the contrast between $|1\rangle$ and $|0\rangle$ state preparations as a function of power. The
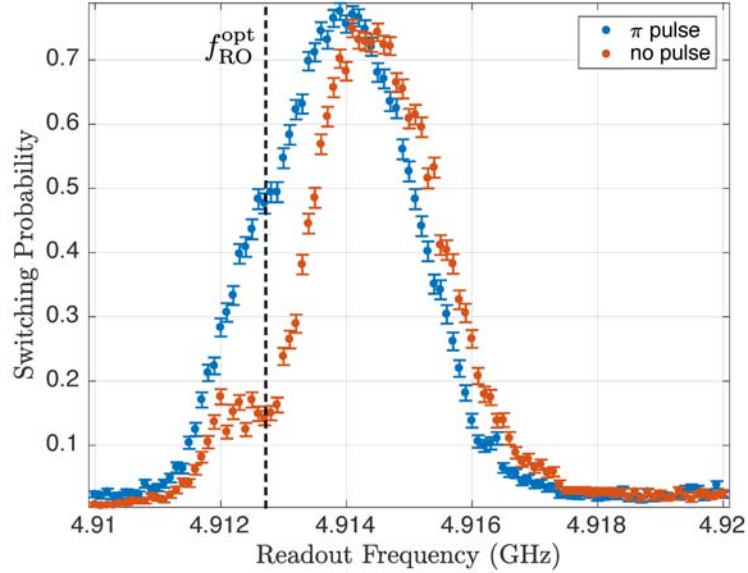
Figure 6.11: JPM switching probability for $|1\rangle$ and $|0\rangle$ state preparations as a function of readout frequency. Dashed line shows optimal readout frequency $f_{\mathrm{RO}}^{\mathrm{opt}} = 4.9127\,\mathrm{GHz}$.

results of this measurement are plotted in Figure 6.10. We measure a maximum contrast at an attenuation of $16\,\mathrm{dB}$; from the Stark shift calibration this corresponds to $\bar{n} = 56$ photons in the cavity. Switching probability as a function of readout pulse frequency is plotted in Figure 6.11; the maximum contrast is obtained at $f_{\mathrm{RO}}^{\mathrm{opt}} = 4.9127\,\mathrm{GHz}$. Due to the large linewidth of the cavity, the bright state appears as a side-lobe of the resonance.

6.4.1 Rabi Oscillations

The bringup of the qubit proceeds along largely the same lines as the procedure described in section 6.3. We again use the CMA-ES optimizer to do an on-line
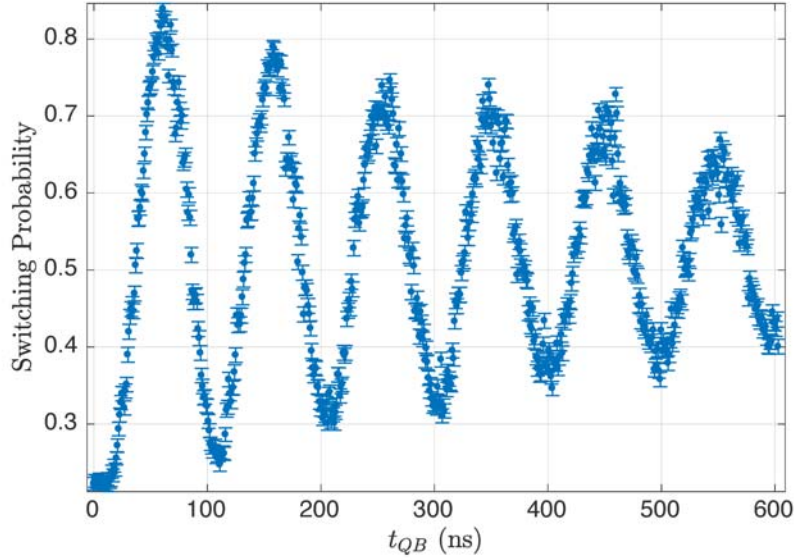
Figure 6.12: Rabi oscillation data taken using a bright state measurement, with $\bar{n} = 56$.

optimization of JPM measurement, qubit drive, and readout parameters to maximize the contrast difference between $|0\rangle$ and $|1\rangle$ state preparations. Rabi oscillation data after the optimization finds a maximum is plotted in Figure 6.12. The Rabi oscillation visibility has increased by almost a factor of 2 to 62%. Since the JPM readout parameters are nearly identical to those used for the measurement in the dispersive limit, we attribute this increase entirely to the larger photon population in the cavity. This is the same mechanism by which a large signal to noise ratio increase is observed in heterodyne measurement, as for example in [120]. For JPM readout experiments in which the QND-ness of the measurement is not important, the cavity and qubit parameters should be chosen in order to maximize the bright state contrast, as discussed in appendix B.

6.5 Readout Fidelity with the JPM

6.5.1 Measured Fidelity

To better understand the achieved readout fidelity, we compare the switching probability and contrast as a function of JPM fast pulse amplitude in Figure 6.13a[1]. It is important to note that the contrast plotted here is not the difference between qubit state preparations but the raw contrast between a measurement of the qubit and the dark switching (no readout drive) probability

$$C_{\text{raw}} = P_{\text{bright}} - P_{\text{dark}} \tag{6.6}$$

The measurement fidelity of the JPM readout is not defined by this contrast but rather the contrast between $|0\rangle$ and $|1\rangle$ qubit preparations:

$$C_F = P_{|1\rangle} - P_{|0\rangle} \tag{6.7}$$

This contrast is also the overall visibility of the Rabi oscillations. We observe a maximum measurement fidelity of 35% in the dispersive limit at $\bar{n} = 12$ photons and 62% in the bright state at $\bar{n} = 56$ photons. These fidelities are the so-called "raw" fidelity of the measurement, and do not take into account infidelity arising from errors in state preparation. It is a common practice in the literature to report "corrected" fidelities which adjust for the effect of qubit state error and infidelity

---

[1]This data has a slightly lower visibility than what is presented in Figure 6.12, likely due to a drift in T_1.

from other sources [64].
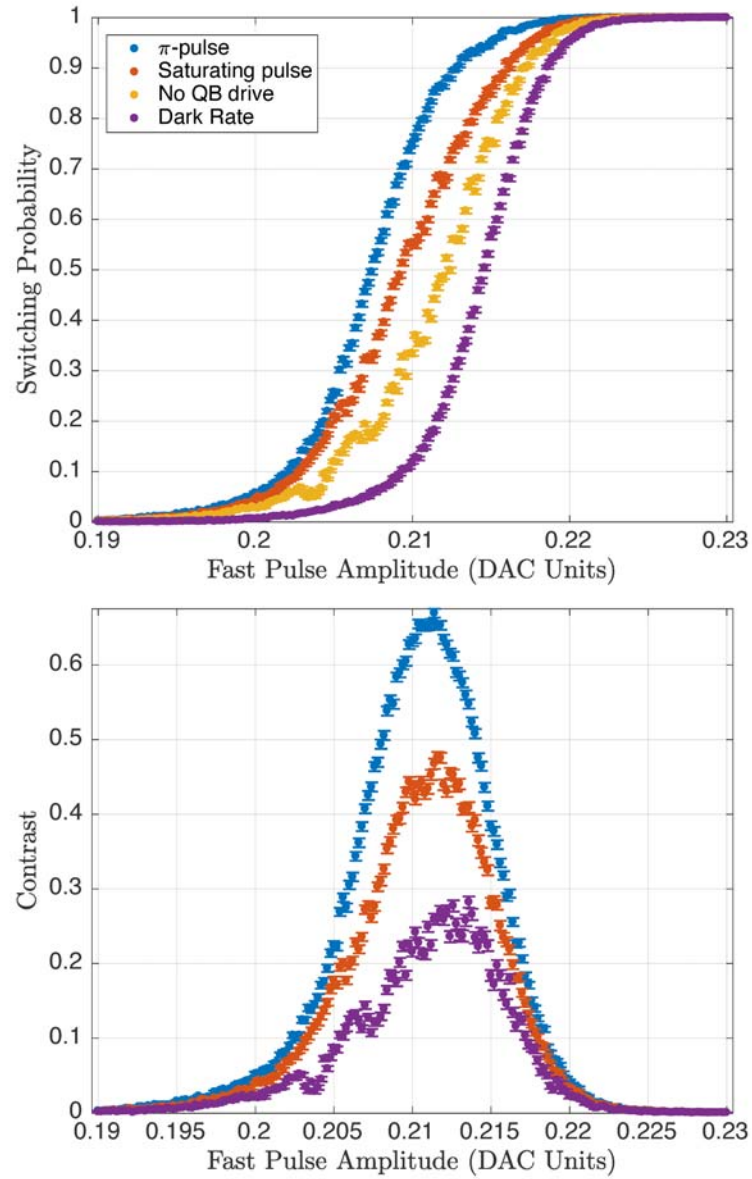
Figure 6.13: (a) Switching probability and (b) raw contrast for different qubit drive pulses.

6.5.2 Increasing Fidelity

What are the origins of infidelity in the JPM measurement? The first identifiable source of infidelity is the relaxation of the qubit during measurement. As shown in [50], a finite T_1 will reduce the fidelity of a photon counting measurement by a factor $\exp(t_{\mathrm{means}}/2T_1)$. Even though the readout resonator drive pulses we use in these measurements are fairly short, with $t_{\mathrm{RO}} = 320\,\mathrm{ns}$, they are still a significant fraction of T_1, causing a significant loss of fidelity. Furthermore, the short T_1 makes it likely that there is a significant excess thermal occupation of the $|1\rangle$ state and higher states, which will be misidentified during state preparation. Here the JPM is at a disadvantage: while it is easy to measure these excess populations with a heterodyne readout [71], the binary output of the photon counter requires a more involved protocol. One possibility would be to use Rabi oscillations on the ω_{21} transition, as proposed in [52]. As a first step, we can check that

$$\frac{P_{|1\rangle} - P_{\mathrm{sat}}}{P_{\mathrm{sat}} - P_{|0\rangle}} \approx 0.5 \tag{6.8}$$

which is true for the data presented in Figure 6.13b, indicating that the excess population is not enormous.

The largest source of infidelity can immediately be identified by comparing the dark switching probability and the switching probability of the $|0\rangle$ state preparation. As explained in section 6.2, the finite cavity κ means that there is a significant population of photons in the cavity after the measurement drive even when the qubit is in the ground state. Options for mitigating this effect include a smarter
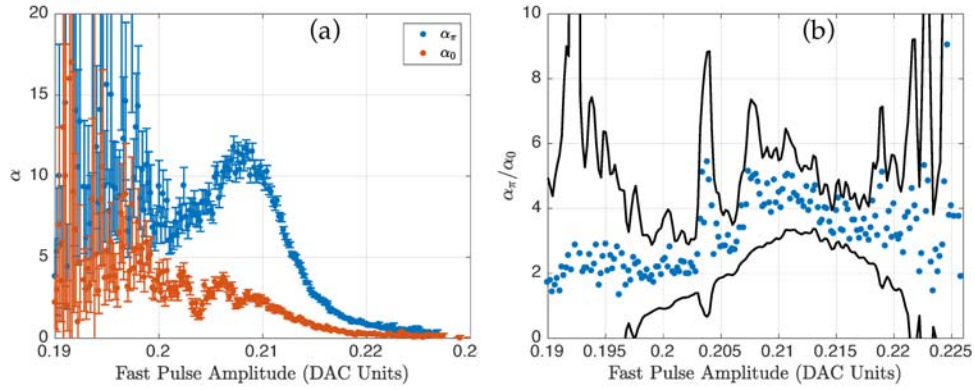
Figure 6.14: (a) Calculated figure of merit α for qubits measured with and without a π-pulse. (b) Ratio of the two figure of merits. Black lines indicate 1σ errors.

choice of qubit parameters, a tunable coupler at the output of the cavity [132, 153], or a cavity reset pulse that selectively drives the $\left|\alpha_{|0\rangle}\right\rangle$ back to the vacuum. To quantify the effect of this unwanted photon population, we calculate the JPM figure of merit α_π, α_0 for a qubits prepared both with and without a π-pulse using eq. (5.14). The figure of merit for the two experiments and their ratio is plotted in Figure 6.14. As $\alpha = \eta\lambda/\Gamma_d$, the ratio is a measurement of the difference in the cavity photon population for the two qubit preparations. We observe that $\bar{n}_{|1\rangle} \approx 5\bar{n}_{|0\rangle}$, which we certainly could improve. The calculation of the optimal qubit and cavity parameters for the generation of high-fidelity pointer states is performed in appendix B.

The extracted figure of merit α also allows us to calculate the expected maximum contrast for a cavity that has been perfectly reset using the expression for $C_{\max}$ in eq. (3.14). This is shown in Figure 6.15, where we also correct for infidelity due to energy relaxation during the measurement drive. The data below FPA ≈ 0.2 should be ignored as the small switching probabilities make the data too noisy to
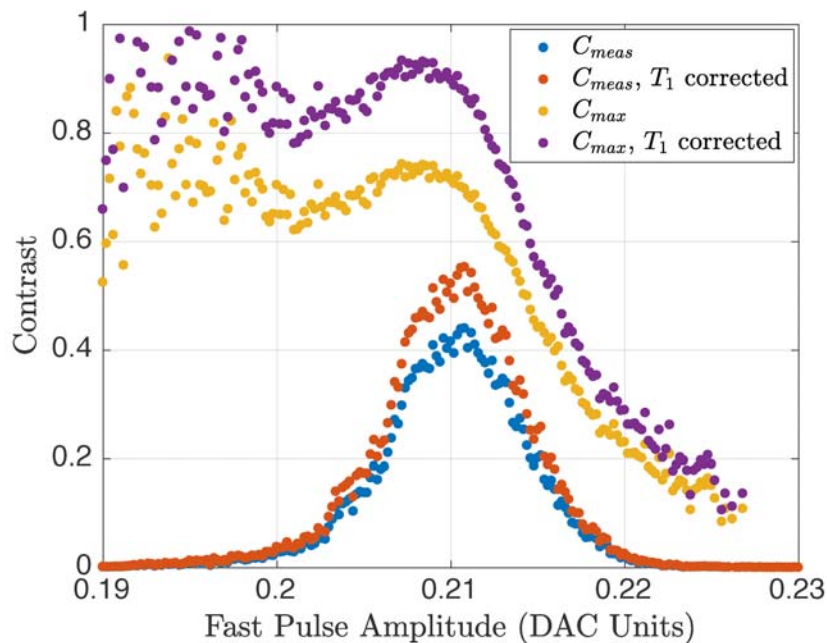
Figure 6.15: Measured contrast C_{means} and expected maximum contrast C_{max} for the bright state readout, and contrast corrected for infidelity due to energy relaxation during measurement, taking $t_{\mathrm{RO}} = 320\,\mathrm{ns}$ and $T_1 = 700\,\mathrm{ns}$.

draw any conclusions. The corrected contrast data show that it should be possible with a longer-lived qubit and a better-optimized pointer state preparation protocol to reach measurement fidelities in excess of 90%, comparable to those achieved with heterodyne readout.

7 CONCLUSIONS AND OUTLOOK

In summary, we have described the development and measurement of a microwave photon counter based on a current biased Josephson junction. We have measured its quantum efficiency to be at the percent level at $5\,\mathrm{GHz}$, with a noise equivalent power comparable to other photon counters. We have also discussed its use as a readout tool for measurement of the state of a transmon qubit. We observe maximum raw measurement fidelities of 35% in the dispersive limit and 62% using a bright state readout.

A look at the JPM figure of merit $\alpha = \eta\lambda/\Gamma_d$ shows the options available to us for improving the fidelity to the greater than 90% needed to make the JPM a truly useful tool in cQED systems. Increasing quantum efficiency η will require better matching at the JPM input, as well as a reduction in the loss between the qubit and counter. We should be able to reduce the dark switching rate by using microwave-assisted measurement of a third $|f\rangle$ state in the junction well, and by using the phase-biased JPM design discussed below. Finally, improved qubit readout protocols that include a cavity reset pulse, or different techniques for preparing cavity pointer states such as the use of a tunable coupler should increase the photon number contrast during a measurement. In parallel, an improved theoretical understanding of the JPM measurement should be developed, beyond the approximations derived in section 3.3.

7.1 Improved JPM Circuits

7.1.1 Flux-Biased JPM
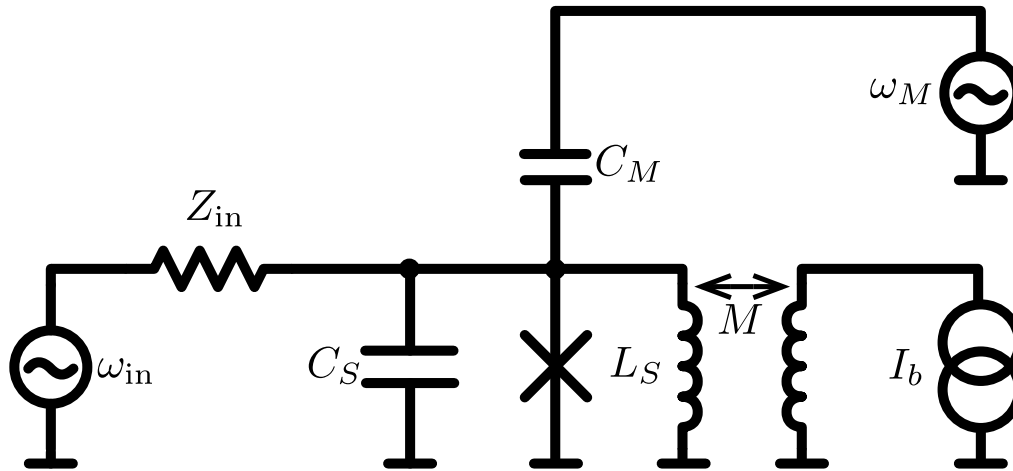
Figure 7.1: Flux-biased JPM circuit.

A major limitation of the current biased junction JPM is the long reset time that is needed to allow heat and quasiparticles to dissipate. A circuit that does not switch to the voltage state would be preferable to the current set-up. One possibility is to shunt the output of the JPM with a small resistance, but a better idea seems to be to move towards a circuit that more closely resembles that of a phase qubit. By shunting the junction with an inductor, the potential energy gains an additional δ^2 curvature, where δ is the phase across the junction. If the inductance is chosen such that [38] $\beta_L = 2L_S I_c/\Phi_0 \lesssim 2.5$, there will be two potential energy minima with different plasma frequencies. A microwave reflection measurement can then determine the state of the junction by monitoring the reflection on a weakly capacitively coupled port. Not only does this circuit not switch out to the voltage

state, but the relatively higher quality factor of the circuit should make it possible to use a third level in the junction minimum to further suppress the dark counting rate. Using an inductively coupled flux bias line also helps shield the junction against decoherence from the current bias source. One challenge of implementing this circuit is that an input matching network will pull and de-Q the plasma resonances of the JPM; we hope that the quantum efficiency gain from using a two-photon readout will offset the lack of a matching network.

7.1.2 SFQ Readout JPM
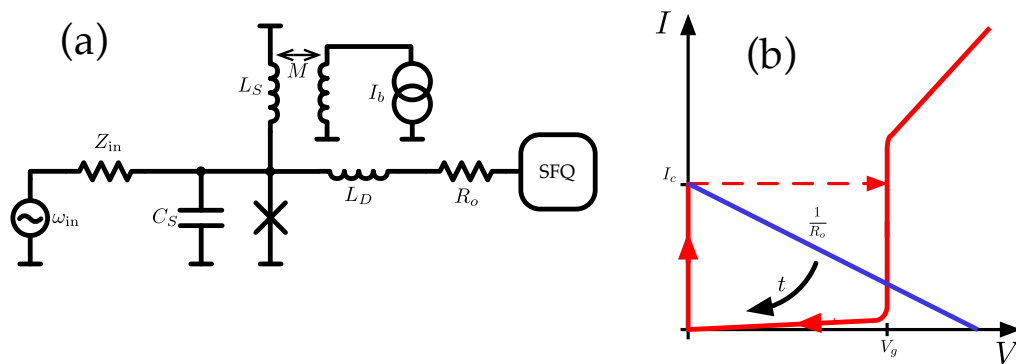
Figure 7.2: (a) SFQ Readout JPM circuit diagram. (b) SFQ Readout JPM current-voltage characteristic, showing the load line of the output circuit in blue.

Recently, a scheme for controlling quantum circuits using single flux quantum (SFQ) logic was proposed [104]. SFQ logic [93, 21] is an all-superconducting digital logic family that relies on the propagation of individual flux quanta to represent data. It has been extensively studied and used to develop extremely fast classical digital circuits. This is an attractive proposal as SFQ is inherently compatible with existing superconducting quantum logic. Bringing the control hardware as close as

possible to the quantum devices offers the potential for significant reductions in overhead, and is a much more viable proposal for scaling to large quantum devices.

The JPM integrates naturally into a SFQ control set-up as its binary output is well-suited to be interfaced to flux quantum logic. This can be accomplished using a circuit like the one drawn in Figure 7.2a. A small output resistor ($R_o \sim 1\,\Omega$, the input impedance of an SFQ circuit) converts the JPM switch into a flux slip that can be coupled to the digital logic. A large output decoupling inductor $L_D \gg L_J$ protects the junction from being decohered by the low-impedance SFQ logic. This inductor also has the advantage of automatically resetting the JPM, in a similar manner to what happens in a Josephson relaxation oscillator [142]. The Josephson junction will attempt to switch to the voltage state, but this voltage will be discharged as a current develops through the shunt inductor. This reduces the junction bias (or equivalently, reduces the tilt of the washboard potential) until the junction retraps into the voltage state [92]. As long as the output load line, shown in blue in Figure 7.2b intersects the steep part of the junction IV characteristic, the load line will swing back towards the origin in a time $t_{\text{reset}} \sim L_D/R$. Numerical simulations have shown the validity of this concept, and we hope it will find a role in future implementations of SFQ-qubit control circuits.

7.2 Conclusion

To our knowledge, the results in this thesis are the first measurement of a transmon qubit with a photon-counting circuit. They therefore represent only the

first steps in a wider world of qubit readout, especially when compared to the large body of work published on heterodyne measurements. Microwave photon counting has received increasing attention, with groups proposing implementations different to our own [129, 68]. We hope that continued attention will bring new results, and show a promising way forward for the development of quantum computation.

A   DETAILS OF THE JOSEPHSON JUNCTION POTENTIAL

In this appendix we summarize several useful results on the tilted washboard potential (Equation 2.20) that describes a Josephson junction of critical current I_c biased with current I_b. We first derive the cubic approximation to this potential, which is valid near one of the potential minima for $I_b/I_c \to 1$ so long as $E_J/E_C \gg 1$. Experimentally, typical values of $E_J \equiv \Phi_0 I_0/2\pi \sim 1\,\text{eV}$ and $E_C = e^2/2C_J \sim 10^{-8}\,\text{eV}$, so the current biased junction is safely in this limit. We then use the WKB appoximation to calculate the energies and tunneling rates of the states localized in the well. Finally, we use the complex scaling method to numerically compute these energies and widths with higher accuracy.

While most this material has already been extensively studied ([23, 24, 86, 87, 41, 101, 40, 102, 1]) , these results are necessary to calculate various parameters of the JPM. They can be hard to track down in the literature (especially the exact transformation used to get the cubic approximation) and different authors use different conventions. The complex scaling method in A.3 was first developed for calculating resonances in atomic systems, and publications on the subject are difficult to unpack. It is hoped that the reader will find this a useful and clear exposition, if somewhat lacking in mathematical rigor. For the gory details, the reader is encouraged to read Frank Strauch's thesis [138] for an especially lucid exposition of these issues.

A.1 Cubic Approximation

We first write the complete Hamiltonian for the current biased Josephson junction as:

$$\hat{H} = \frac{4E_C}{\hbar^2}\hat{p}_\delta^2 - E_J(\cos\hat{\delta} + i_b\hat{\delta}) \tag{A.1}$$

where $\hat{\delta}$ is the operator for the phase difference across the junction and $\hat{p}_\delta^2$ its conjugate momentum. For convenience, in the rest of this appendix we will drop the "hat" notation for operators. The "mass" of the phase particle is given by $m^{-1} = 8E_C\hbar^{-2}$. The minimum and maximum of the potential are located at:

$$\delta_{min} = \arcsin i_b \tag{A.2}$$

$$\delta_{max} = \pi - \arcsin i_b \tag{A.3}$$

and the frequency of small oscillations around this minimum (the plasma frequency) is:

$$\begin{aligned}\omega_p &= \sqrt{\frac{1}{m}\frac{d^2U(\delta_{min})}{d\delta^2}} \\ &= \frac{1}{\hbar}\sqrt{8E_C E_J}(1 - i_b^2)^{1/4}\end{aligned} \tag{A.4}$$

It is convenient for the calculations that follow to shift and scale the potential energy so that its minimum is at $\delta = 0$. One possible transformation to accomplish this is:

$$\begin{aligned}x &= \alpha^{-1}\left(\delta - \arcsin i_b\right) \\ p &= \alpha p_\delta\end{aligned} \tag{A.5}$$

where we have defined

$$\alpha = \left(\frac{8E_C}{E_J} \right)^{1/4} \left(1 - i_b^2 \right)^{-1/8} \tag{A.6}$$

Applying A.5 to Equation A.1, we are left with:

$$H = \frac{1}{2m\alpha^2} p^2 + E_J \left(\sqrt{1 - i_b^2} \left(1 - \cos \alpha x \right) + i_b \sin \alpha x - i_b \alpha x \right) \tag{A.7}$$

up to an arbitrary constant that we ignore. Defining $\hbar \omega_p = 1/m\alpha^2$, this can be rewritten as:

$$\frac{H}{\hbar \omega_p} = \frac{1}{2} p^2 + \frac{1}{\alpha^2} \left(1 - \cos \alpha x + i_b \left(1 - i_b^2 \right)^{-1/2} \left(\sin \alpha x - \alpha x \right) \right) \tag{A.8}$$

As mentioned in the introduction, for typical junction parameters α is small, so we expand the potential energy term in α to get the cubic approximation to the washboard potential:

$$\frac{H}{\hbar \omega_p} = \frac{1}{2} p^2 + \frac{1}{2} x^2 - g x^3 + \mathcal{O}(\alpha^2) \tag{A.9}$$

with $g = \alpha i_b / (6\sqrt{1 - i_b^2})$. The cubic approximation to $V(x)$ is plotted in Figure A.1. The minimum is again at $x = 0$, and the maximum at $x_{max} = 1/3g$ with the height of the barrier $V(x_{max}) = 1/54g^2$. Since for this scaled potential the frequency of small oscillations $\hbar \omega = 1$, $V(x_{max})$ is equal to the number of states under the barrier N_s, therefore:

$$g = 1/\sqrt{54 N_s} \tag{A.10}$$
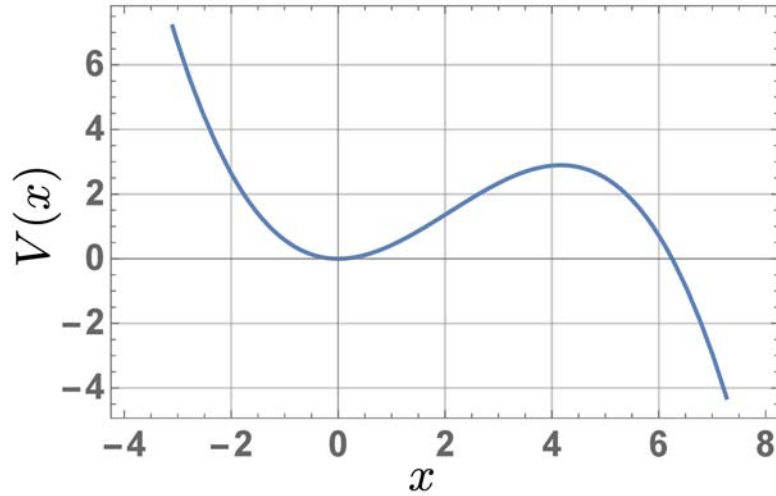
Figure A.1: Plot of the cubic approximation to the washboard with $g = 0.08$.

The number of levels is a useful parameter that completely characterizes the shape of the potential, so it is useful to write it in terms of the physical control knob for this system, the reduced current bias. Working backwards through the various substitutions we have made, the number of states in the well can also be written as:

$$N_s = \frac{1}{3\sqrt{2}} \sqrt{\frac{E_J}{E_C}} \frac{\left(1 - i_b^2\right)^{5/4}}{i_b^2} \tag{A.11}$$

The quantum mechanical study of this cubic potential will be the object of the next two sections. It is interesting to note that even though we commonly speak of the "energy levels" near the minimum of the washboard or cubic potentials, these are not true energy levels but more akin to scattering resonances [1, 34]. They are metastable superpositions of the true eigenstates of the system that are initially localized to the minimum, but over time evolve to states which have a large

amplitude outside of the well. This exponential decay process to the voltage state is of course exactly the mechanism through which we detect photons with the JPM.

A.2 Perturbation Theory and WKB Formulae

A.2.1 Energy Levels

A useful first step in calculations involving the cubic potential A.9 is to use perturbation theory to characterize the energies of the metastable states. As usual, we write

$$
\begin{aligned}
H &= H_0 + gH_1 \\
H_0 &= \frac{1}{2}\left(p^2 + x^2\right) \\
H_1 &= -x^3
\end{aligned}
\tag{A.12}
$$

This is a valid approach since we know that experimentally g is small. Furthermore, the cubic has a nice symmetry property which can be seen by considering the action of the parity operator $\Pi\,|x\rangle = |-x\rangle$:

$$
H(-g) = \Pi^\dagger H(g)\Pi
\tag{A.13}
$$

Since Π is unitary, $H(-g)$ and $H(g)$ have the same eigenvalues and we need only consider $g \geq 0$.

A thorough treatment through Rayleigh-Schrödinger perturbation theory, while

possible, is extremely tedious, and results in power series that are formally divergent. Alvarez [1] has studied the perturbation theory in detail using Borel summation. We will content ourselves with calculating the energies to second order using harmonic oscillator wavefunctions. In this basis, it can be shown that

$$\langle n|x^3|m\rangle = \frac{1}{2\sqrt{2}}(\sqrt{m(m-1)(m-2)}\delta_{n,m-3}+$$

$$3\sqrt{m^3}\delta_{n,m-1} + 3\sqrt{(m+1)^3}\delta_{n,m+1}+$$

$$\sqrt{(m+1)(m+2)(m+3)}\delta_{n,m+3}) \quad (A.14)$$

A straightforward application of perturbation theory [127] gives for the first three level splittings:

$$\omega_{10} = 1 - \frac{15g^2}{2}$$
$$\omega_{21} = 1 - 15g^2 \quad (A.15)$$
$$\omega_{32} = 1 - \frac{179g^2}{8}$$

Recalling that we have defined the coupling $g = 1/\sqrt{54N_s}$ and that to make the connection to the Josephson junction potential we should rescale these energies by $\hbar\omega_p$, we recover the expression usually found in the literature for the transition frequency between ground and first excited states:

$$\hbar\omega_{10} = \hbar\omega_p \left(1 - \frac{5}{36N_s}\right) \quad (A.16)$$

Note that the system's anharmonicity is given by:

$$\alpha = \omega_{21} - \omega_{10} = -\frac{5\hbar\omega_p}{36N_s} \tag{A.17}$$

which leads to a relative anharmonicity of 8% for $N_s = 2$.

A.2.2 Tunneling Rates

Because of the significant experimental effort ([101, 41], and many others) devoted to testing the effects of macroscopic quantum tunneling in Josephson junctions the calculation of tunneling rates using the WKB approxmation. The most important work is that of Caldeira and Leggett [23, 24, 25], who also include the effects of dissipation due to the system's connection to the environment which acts as a heat bath. We should also mention the theory due to Larkin and Ovchinnikov [86, 87, 40] which considers the effect of a coherent drive on the lifetime of metastable states. Rather than give a complete overview of the lengthy WKB calculations[1], we will only sketch out the method, following [138] and cite the most important results.

The WKB method [133] consists in approximating solutions to the Schrödinger equation in the form

$$\Psi(x) \sim \exp\left(\int_x^{x_t} \frac{\sqrt{2m}}{\hbar} \sqrt{E - V(x')} dx'\right) \tag{A.18}$$

where x_t are classical turning points of the potential. To apply the approximation

---

[1]The WKB approach in this section is based on the standard wavefunction-matching approach, while Caldiera and Leggett use a more general path integral formulation. See [138] and [133] for details.

to Equation A.9 we need to find the roots of the cubic in the WKB integral of Equation A.18:

$$\frac{1}{2}x^2 - gx^3 - E \tag{A.19}$$

Using the trigonometric solution to the cubic [84], they can be written as

$$
\begin{aligned}
x_0 &= \frac{1}{6g}(1 + 2\cos(\theta + 2\pi/3)) \\
x_1 &= \frac{1}{6g}(1 + 2\cos(\theta + 4\pi/3)) \\
x_3 &= \frac{1}{6g}(1 + 2\cos(\theta))
\end{aligned}
\tag{A.20}
$$

where

$$\theta = \frac{1}{3}\arccos\left(1 - 108g^2 E\right) \tag{A.21}$$

Expanding these expressions for small g to $\mathcal{O}(g^3)$, we get:

$$
\begin{aligned}
\theta &= (24E)^{1/2}g + \frac{3}{8}(24E)^{3/2}g^3 \\
x_0 &= -\sqrt{2E} + 2Eg - 5\sqrt{2E^3}g^2 + 32E^2 g^3 \\
x_1 &= \sqrt{2E} + 2Eg + 5\sqrt{2E^3}g^2 + 32E^2 g^3 \\
x_2 &= (2g)^{-1} - 4Eg - 64E^2 g^3
\end{aligned}
\tag{A.22}
$$

The WKB integral in the classically forbiddden region under the barrier is

$$
\begin{aligned}
S(x) &= \int_{x_1}^{x_2} dx' \sqrt{x'^2 - 2\lambda x'^3 - 2E} \\
&= \sqrt{2g}\int_{x_1}^{x_2}\sqrt{(x - x_0)(x - x_1)(x - x_2)}
\end{aligned}
\tag{A.23}
$$

This integral is messy, but it can be computed using the asymptotic form of the hypergeometric function[2] [138] to find

$$S = \frac{1}{15g^2} - \frac{E}{2} + \frac{1}{2} E \log\left(\frac{Eg^2}{8}\right) + \mathcal{O}(g \log g) \tag{A.24}$$

Assuming that the wavefunctions in the well are well approximated by those of the harmonic oscillator so that $E = n + 1/2$, this expression can be substituted into the Gamow formula [51] for tunneling rates to finally obtain:

$$\Gamma_n = \frac{\omega_p}{n!\sqrt{2\pi}} (432N_s)^{n+1/2} \exp\left(-\frac{36}{5}N_s\right) \tag{A.25}$$

A.3 Complex Scaling Method

In this section, we study the energies and tunneling rates of the cubic anharmonic oscillator states numerically, using the complex scaling method. This method, which was first developed to study resonances in atomic and nuclear systems, greatly simplifies the computation of the complex eigenenergies of continuum states. We will first give a brief, informal overview of the method and then apply it to the cubic oscillator. Our treatment largely follows that of Aoyama *et al.* [4]. For a much more comprehensive treatment of the subject, we recommend the excellent review article by Moiseyev [108].

---

[2]Mathematica to the rescue, as usual.

A.3.1   The Method

The resonances of a scattering problem are characterized by two parameters: their energy E and width Γ, which can be considered the real and imaginary parts of a complex energy $\epsilon = E + i\Gamma/2$. For a given Hamiltonian H, these energies are the poles [161] of the operator $G = (H - \epsilon)^{-1}$, which is essentially the Green's function corresponding to H. Bound states correspond to poles on the real axis, while resonances are located in the lower half-plane, typically hidden by branch cuts in G. This is because the wavefunctions which describe the resonance states are not bounded as $\Psi(x \to \infty)$, and are therefore not in the Hilbert space of the problem.

To illustrate this, consider the solutions to the time-independent Schrödinger equation of a scattering problem, which can be written in the form [127]:

$$\Psi(r \to \infty) \simeq e^{-ikr} + S(k)\frac{e^{ikr}}{r} \tag{A.26}$$

where the wavevector k is given by $E = (\hbar k)^2/2m$. Since $k = k' - ik''$ is complex, the outgoing wave will be

$$\Psi_{out}(r) \sim e^{ikr} = e^{ik'r}e^{k''r} \tag{A.27}$$

Clearly, the imaginary part of ϵ will cause the wavefunction to diverge. The insight

of the complex scaling method is that by making the substitution[3]:

$$r' = re^{i\theta} \tag{A.28}$$

we can change the asymptotic behavior of Ψ. The effect of this substitution on A.27 is:

$$\Psi_{out}(r') \to \exp\left[i(k'\cos\theta + k''\sin\theta)r\right]\exp\left[-(k'\sin\theta - k''\cos\theta)r\right] \tag{A.29}$$

so that as long as $\tan\theta > k''/k'$ the state is normalizable. Practically, we define a transformed Hamiltonian[4]:

$$H(\theta) = e^{-2i\theta}T + e^{-i\theta}V \tag{A.30}$$

where T and V are the kinetic and potential energy operators. We then pick a convenient (finite) basis $\{\psi_n(\theta)\}$ for the wavefunctions and solve the eigenvalue problem

$$[H(\theta) - \epsilon_n(\theta)]\,\psi_n(\theta) = 0 \tag{A.31}$$

There remains the problem of determining the scaling parameter θ, which may be in general complex. Yaris and Winkler [160] suggest using the so-called hypervirial theorem to check that

$$2\langle T(\theta)\rangle = -\langle V(\theta)\rangle \tag{A.32}$$

---

[3] Also known as the *dilatation* transformation.

[4] A theorem by Balslev and Combes [6] shows that the eigenvalues of this transformed Hamiltonian are independent of θ if it is sufficiently large and are exactly those of the unscaled problem.

is satisfied for the correct value of θ. This is equivalent [83] to checking that

$$\frac{\partial}{\partial\theta}\operatorname{Tr}H = 0 \qquad\qquad (A.33)$$

For the cubic, it is enough to consider only real values of θ, and we simply plot the energies found from Equation A.31 for different values of the scaling parameter and choose a value where $\partial E_n/\partial\theta = 0$.

A.3.2   The Cubic Potential

We now apply the complex scaling method (CSM) to the Hamiltonian of Equation A.9. A convenient basis to use is the wavefunctions of the quantum harmonic oscillator:

$$\psi_n(x) = \left(\frac{1}{\sqrt{\pi}2^n n!}\right)^{1/2} e^{-x^2/2}H_n(x) \qquad\qquad (A.34)$$

where $H_n(x)$ are the Hermite polynomials. Writing H as a matrix, we then numerically solve the eigenvalue equation A.31 to calculate the complex energies of the cubic oscillator, as well as the wavefunctions that correspond to those energies

$$\Psi(x) = \sum_{n=0}^{N} c_n\psi_n(x) \qquad\qquad (A.35)$$

We find that $N = 100$ is sufficient to ensure convergence for all values of g, consistent with the results of Alvarez [1]. The real part of ϵ_n is plotted for different values of the complex scaling parameter θ in Figure A.2; there is a large region wherein $\operatorname{Re}\epsilon$ is constant, indicating that the method has converged. We choose $\theta = 0.1\pi$, a value

that ensures convergence for all tested values of g. Figure A.3 shows the first three wavefunctions calculated using Equation A.35. As expected, $\langle \Psi_n \rangle$ is localized to the potential well.
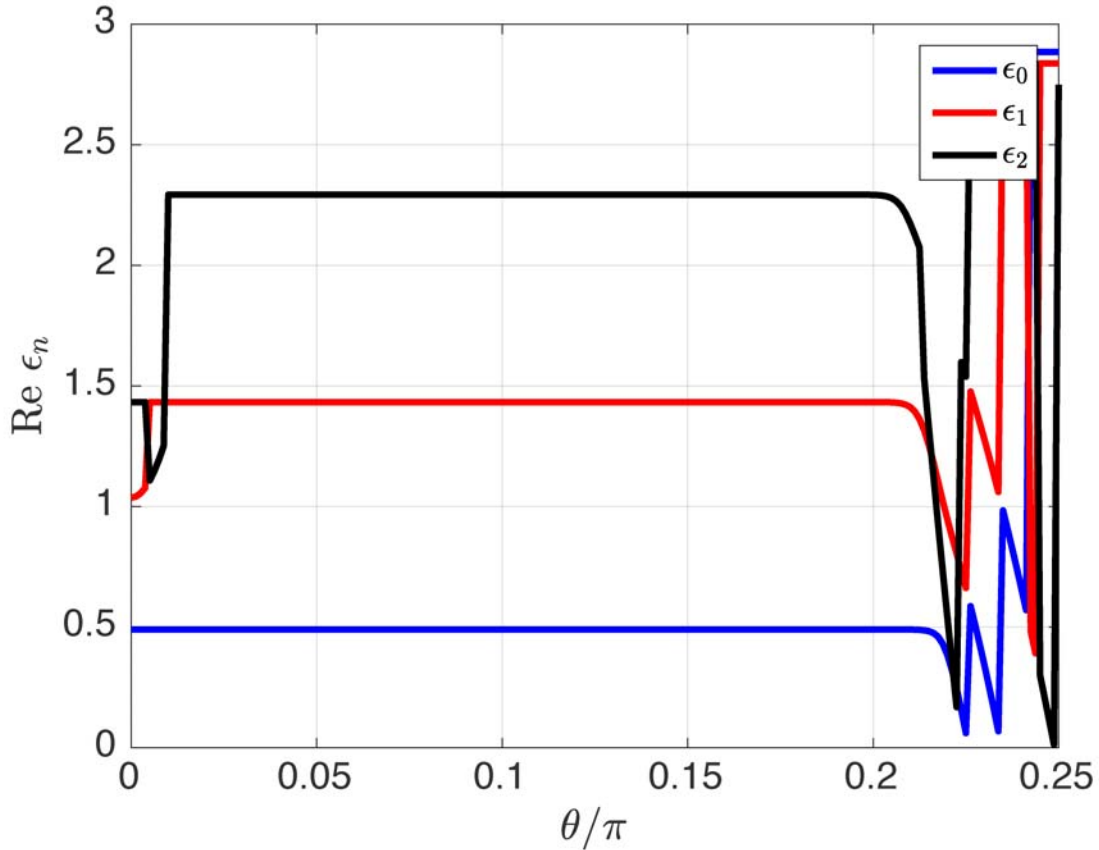
Figure A.2: Real part of the first three eigenvalues of H with $g = 0.08$.

With the complex scaling method outlined above, it becomes simple to calculate the energy levels and tunneling rates of the Josephson junction. We need only pick $g = 1/\sqrt{54 N_s}$ and calculate $E_n = \operatorname{Re} \epsilon_n$ and $\Gamma = -2 \operatorname{Im} \epsilon_n$. This is done for typical JPM parameters in Figure A.4 for different values of the normalized current bias. As
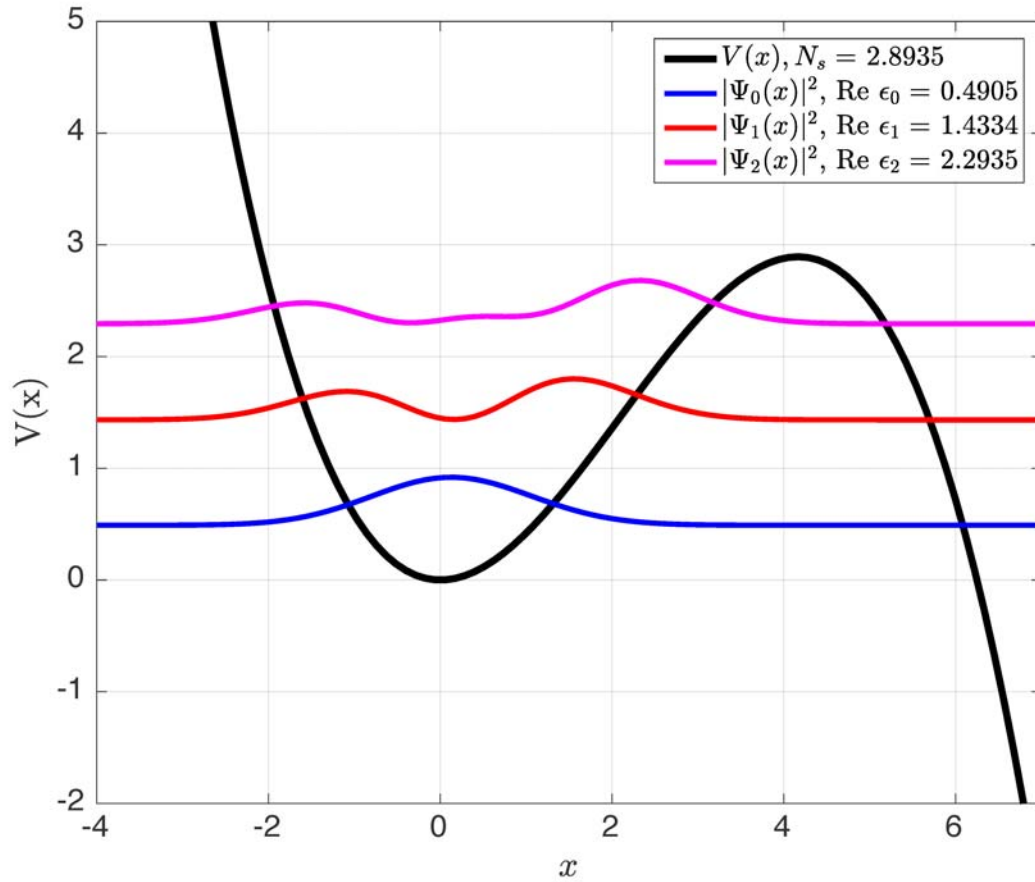
Figure A.3: Potential and probability distributions for the first three eigenfunctions of H with $g = 0.08$ calculated with the complex scaling method at $\theta = 0.1\pi$. Each wavefunction is shifted upwards from the x-axis by an amount corresponding to $\mathrm{Re}\,\epsilon_n$.

can be seen by comparing the CSM energies and tunneling rates to those computed from the perturbation theory and WKB approximations of section A.2, the latter are quite accurate for deeper wells, over-estimating the transition frequencies and under-estimating tunneling rates. However, once $N_s < 2$ and the upper level begins

to approach the top of the energy barrier the CSM calculation deviates significantly. This makes sense, as when there is only one energy level in the potential well the $n = 1$ state loses its metastable character and is more akin to a continuum state, and it is no longer appropriate to think of it as tunneling out of the well.

Finally, we calculate the coupling between energy levels for the JPM. As shown in section 3.3, the interaction Hamiltonian between the JPM and its input line is given by:

$$\mathcal{H}_{\text{int}} = \left(\frac{\Phi_0}{2\pi}\right) \Delta \hat{I} \hat{\delta} \tag{A.36}$$

where $\hat{\delta}$ is the junction phase operator. We are therefore interested in the matrix elements $\langle m|\hat{\delta}|n\rangle$. In the formalism we have developed, the position operator $\hat{x}$ takes the place of the junction phase, and it is straightforward to calculate these matrix elements from the coefficients $\boldsymbol{c} = \{c_n\}$ calculated for each wavefunction:

$$\langle m|\hat{\delta}|n\rangle = \boldsymbol{c}_m \cdot \hat{x} \cdot \boldsymbol{c}_n \tag{A.37}$$

These coefficients are plotted in Figure A.5.
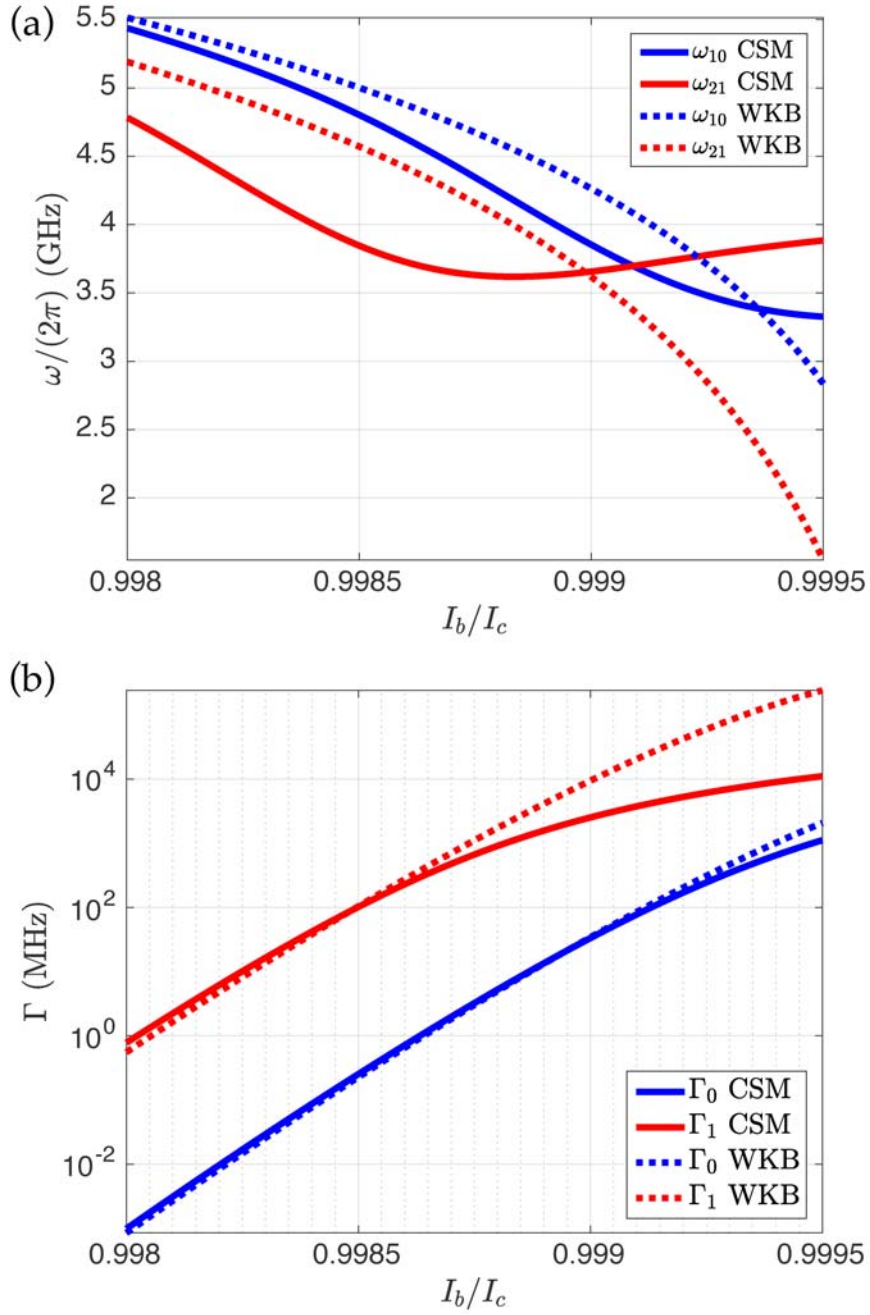
Figure A.4: (a) Transition energies $\omega_{n+1,n}$ and (b) tunneling rates Γ_n calculated for a current biased JPM with junction area $500\,\mu\text{m}^2$ and critical current density $40\,\text{A}/\text{cm}^2$ found using the complex scaling method (CSM) and the WKB approximation.

.
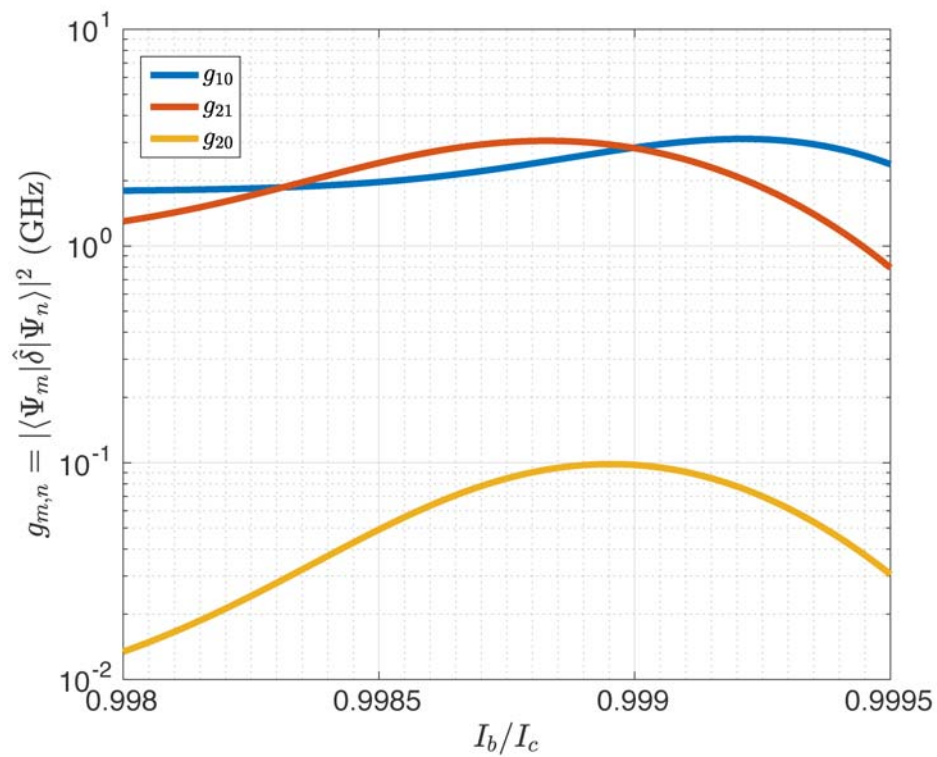
Figure A.5: Matrix elements of the phase operator between ground and the first excited state and the first and second excited states. Calculated for a current biased junction of area $500\,\mu m^2$ and critical current density $40\,A/cm^2$.

In this appendix, we consider the dynamics of the coupled qubit-cavity system, and derive several useful results from a semi-classical perspective. Much of this work is based on the studies by Boissonneault *et al.* [16, 17, 18], and is inspired by the model considered in [13].

B.1   Semiclassical Qubit and Cavity

We first consider the conventional circuit-QED setup, with a qubit coupled with strength g to a cavity at frequency ω_r. The qubit has $|0\rangle$-$|1\rangle$ transition frequency ω_{10} a fixed detuning $\Delta = \omega_{01} - \omega_r$ from the cavity frequency and anharmonicity α. From standard cQED theory:

$$\chi = \frac{g^2}{\Delta}\frac{\alpha}{\Delta - \alpha} \tag{B.1}$$

$$n_{crit} = \frac{1}{4}\left(\frac{\Delta}{g}\right)^2 \tag{B.2}$$

The two Lamb-shifted qubit frequencies are $\omega_\pm = \omega_r \pm \chi$. The cavity can be asymetrically coupled, such that the total photon loss rate out of the cavity is $\kappa = \kappa_{in} + \kappa_{out}$. Note that $\kappa = \omega_r/Q$.

An rf drive is applied to the cavity with amplitude ϵ and drive detuning $\Delta_d = \omega_d - \omega_r$. We write down the equations of motion governing the coherent state

amplitude α inside the cavity for the two possible qubit states as :

$$\dot{\alpha}_+ = -i\epsilon - i(\Delta_d + \chi - i\kappa/2)\alpha_+ \tag{B.3}$$

$$\dot{\alpha}_- = -i\epsilon - i(\Delta_d - \chi - i\kappa/2)\alpha_- \tag{B.4}$$

For a drive at the low frequency dressed state with $\Delta_d = -\chi$, the above two equations are:

$$\dot{\alpha}_+ = -i\epsilon - \kappa\alpha_+/2 \tag{B.5}$$

$$\dot{\alpha}_- = -i\epsilon + 2i\chi\alpha_- - \kappa\alpha_-/2 \tag{B.6}$$

The formal solution for theses equations for arbitrary drive $\epsilon(t)$ is given by:

$$\alpha_+(t) = -ie^{-\kappa t/2} \int_0^t \epsilon(t')e^{\kappa t'/2}dt' \tag{B.7}$$

$$\alpha_-(t) = -ie^{-\kappa t/2+2i\chi t} \int_0^t \epsilon(t')e^{\kappa t'/2-2i\chi t'}dt' \tag{B.8}$$

In the rest of this note we will assume a constant drive field $\epsilon(t) = \epsilon$. Solving for the coherent state amplitudes:

$$\alpha_+(t) = -i\frac{2\epsilon}{\kappa}\left(1 - e^{-\kappa t/2}\right) \tag{B.9}$$

$$\alpha_-(t) = \frac{2\epsilon}{4\chi + i\kappa}\left(1 - e^{-\kappa t/2}e^{2i\chi t}\right) \tag{B.10}$$

Typical state trajectories as a function of drive length t_d are shown in Figure B.1a, and photon population in Figure B.1b. The state resonant with the drive grows

along one axis in quadrature space, while the other state spirals towards a point along the other axis. Note that if $\kappa = 0$, the detuned cavity state will return to the origin after $t_d = \pi/\chi$.
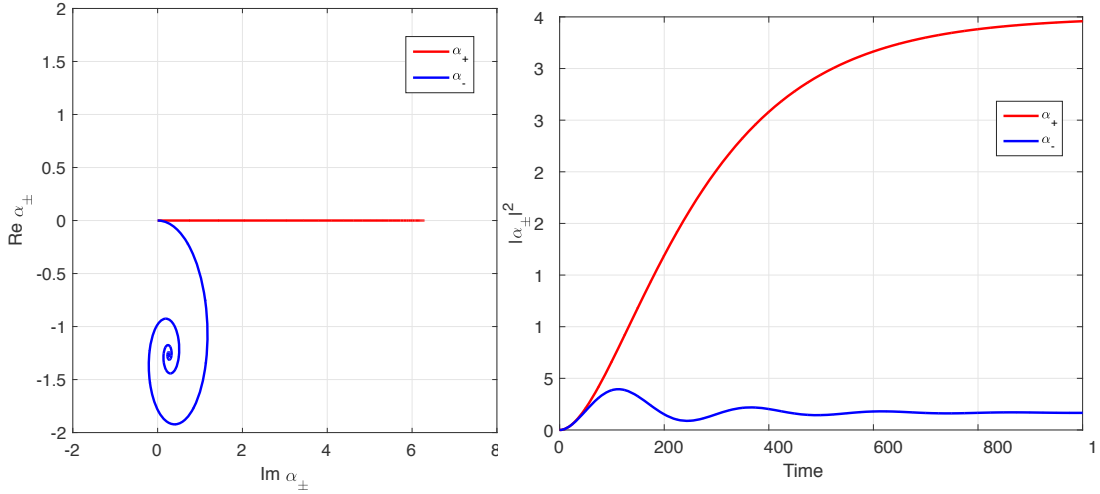
Figure B.1: (a) Cavity state trajectories in IQ space and (b) cavity photon population as a function of time, for $\chi/2\pi = 2\,\mathrm{MHz}$, $\kappa^{-1} = 100\,\mathrm{ns}$, $t_d = 2\pi/\chi$ and $\bar{n} = 40$.

We will assume that we can perform a strong, fast reset of the cavity state, bringing one state back to the origin. This implies that the quantity of interest is the magnitude of the separation between the different cavity states:

$$D = |\alpha_+ - \alpha_-|^2 \tag{B.11}$$

Calculating this quantity using the full expression for the state amplitudes yields an oscillatory function that is not particularly enlightening. Instead, we look at the limit in which damping due to cavity relaxation and is strong enough that the

cavity has reached a steady state. In this case, equivalent to taking the $t \to \infty$:

$$\alpha_+ = -i\frac{2\epsilon}{\kappa} \tag{B.12}$$

$$\alpha_- = \frac{2\epsilon}{4\chi + i\kappa} \tag{B.13}$$

Calculating D:

$$\begin{aligned}
D &= |\alpha_+ - \alpha_-|^2 \\
&= \left| -i\frac{2\epsilon}{\kappa} - \frac{2\epsilon}{4\chi + i\kappa} \right|^2 \\
&= \frac{64\epsilon^2}{\kappa^2} \frac{\chi^2}{16\chi^2 + \kappa^2} \tag{B.14}
\end{aligned}$$

Since we are driving on one of the cavity resonances, we can use Equation B.9 to find a relation between ϵ and the steady state cavity photon population, $\bar{n} = |\alpha_+(t \to \infty)|^2$:

$$\epsilon = \frac{\kappa}{2}\sqrt{\bar{n}} \tag{B.15}$$

We are interested in the flux λ of photons leaving the cavity at the output port, which is given by:

$$\begin{aligned}
\lambda &= \kappa_{out} D \\
&= 16\bar{n}\frac{\kappa\chi^2}{16\chi^2 + \kappa^2} \tag{B.16}
\end{aligned}$$

where we have assumed that the cavity is only weakly coupled at the input and thus $\kappa \approx \kappa_{out}$. Maximizing this function with respect to κ, we find that the optimal cavity

decay rate is given by $\kappa = 4\chi$ and $\lambda_{max} = 2\bar{n}\chi$. Figure B.2a shows the photon flux as a function of κ for long times. As the drive becomes shorter, the optimal value of κ increases, as shown in Figure B.2b, and the maximum possible λ decreases (Figure B.2c). Of interest are the values at $t_d\chi = 0.5$, the optimal time for the $\kappa = 0$ cavity; we find $\lambda_{max}/2\chi\bar{n} = 0.9965$ and $\kappa/\chi = 4.08$.
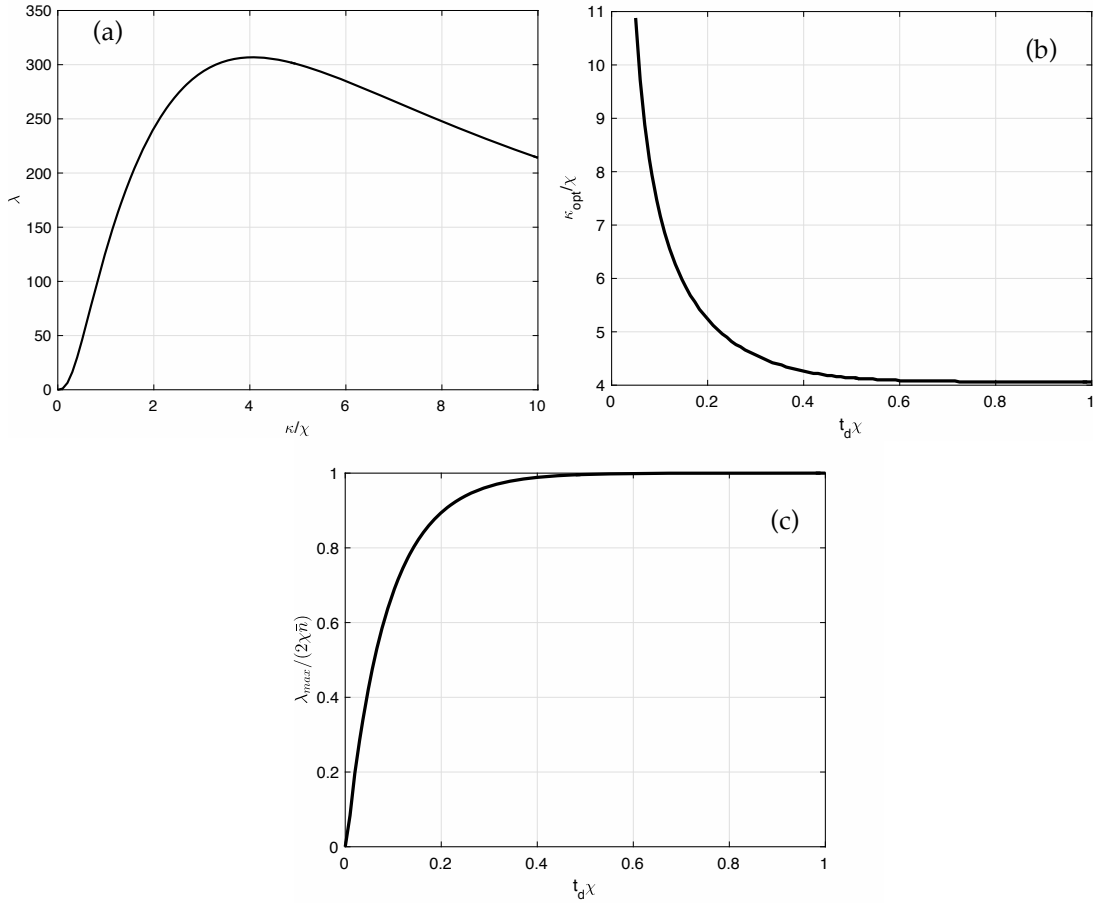
Figure B.2: (a) Photon flux λ vs κ at long times, $\pi/\kappa \ll t$ and $\bar{n} = 10$. The maximum is at $\kappa = 4\chi$. (b) Optimal κ vs. time of cavity drive t_d at fixed $\bar{n}$. (c) Maximum λ for a given cavity drive time at fixed $\bar{n}$.

B.2 Semiclassical Cavity and Quantum Qubit

The model in the previous section is essentially semiclassical, as it does not take into account the drive amplitude dependence of the readout resonator frequency. In order to properly account for this, we treat the qubit quantum mechanically, using an exact diagonalization [18] of the Jaynes-Cummings Hamiltonian in both the two-level approximation and the three-level approximation. A rigorous justification of this model can be found in the papers by Larson and Stenhold [88] and Larson [89], and in the three level case is similar to the model for a Ξ-atom considered in [158][1].

B.2.1 Diagonalizing the Jaynes-Cummings Hamiltonian

Two Level Qubit

Consider a two level qubit with transition frequency ω_{10} coupled to a cavity with frequency ω_r with coupling strength g. The Hamiltonian for this system, using the rotating wave approximation, is:

$$\hat{\mathcal{H}}_2 = \omega_c \hat{a}^\dagger \hat{a} + \frac{\omega_{10}}{2} \hat{\sigma}_z + g \left(\hat{a} \hat{\sigma}^\dagger + \hat{a}^\dagger \hat{\sigma} \right) \tag{B.17}$$

The total number of quanta in the system

$$\hat{N}_q = \hat{a}^\dagger \hat{a} + \frac{1}{2} \hat{\sigma}_z \tag{B.18}$$

---

[1]With the important difference that Wu and Yang diagonalize the Hamiltonian in terms of level energies instead of detunings.

is a conserved quantity, since $\left[\hat{\mathcal{H}}_2, \hat{N}_q\right] = 0$. We therefore diagonalize the Hamiltonian in the basis of constant total excitation number $\{|\pm, n\rangle\}$. In this basis, the Hamiltonian becomes

$$
\begin{aligned}
\hat{\mathcal{H}}_2' &= \hat{\mathcal{H}}_2 - \omega_c \hat{N}_q \\
&= \begin{pmatrix} \Delta/2 & g\sqrt{n} \\ g\sqrt{n} & -\Delta/2 \end{pmatrix}
\end{aligned}
\tag{B.19}
$$

where $\Delta = \omega_r - \omega_{10}$ with degenerate eigenvalues

$$
\chi_\pm = \sqrt{\frac{\Delta^2}{4} + g^2 n}
\tag{B.20}
$$

The original Hamiltonian is therefore

$$
\hat{\mathcal{H}}_2 = \omega_r \hat{a}^\dagger \hat{a} + \frac{1}{2}\left(\omega_z + \chi\right)\hat{\sigma}_z
\tag{B.21}
$$

This last equation makes it clear that the dispersive shift is in fact given by eq. (B.20).

Three Level Qubit

We repeat the same procedure for a three level system. The Hamiltonian is now:

$$
\hat{\mathcal{H}}_3 = \omega_c \hat{a}^\dagger \hat{a} + \sum_{j=0}^{2} \omega_j \hat{\Pi}_{jj} + \sum_{j=0}^{1} g_j \left(\hat{a}\hat{\Pi}_{j+1,j} + \hat{a}^\dagger \hat{\Pi}_{j,j+1}\right)
\tag{B.22}
$$

where ω_j is the energy of the j$^{\text{th}}$ level and $\hat{\Pi}_{ij} = |i\rangle\langle j|$. We can re-write this Hamiltonian in terms of the transition frequencies:

$$\hat{\mathcal{H}}_3 = \omega_c \hat{a}^\dagger \hat{a} + \omega_{10}\hat{\Pi}_{11} + (\Delta_{10} + \Delta_{21})\hat{\Pi}_{22} + \hat{\mathcal{H}}_{\text{int}} \tag{B.23}$$

The total number of quanta is given by:

$$\hat{N}_q = \hat{a}^\dagger \hat{a} + \hat{\Pi}_{11} + \hat{\Pi}_{22} \tag{B.24}$$

and the transformed Hamiltonian in the basis $|j, n\rangle$ is given by

$$\hat{\mathcal{H}}_3' = \hat{\mathcal{H}}_3 - \omega_c \hat{N}_q$$

$$= \begin{pmatrix} 0 & g_0\sqrt{n} & 0 \\ g_0\sqrt{n} & (\Delta_{10} - \omega_c) & g_1\sqrt{n-1} \\ 0 & g_1\sqrt{n-1} & (\Delta_{21} + \Delta_{10} + \omega_c) \end{pmatrix} \tag{B.25}$$

In terms of the eigenvalues of the three-level Hamiltonian $\Lambda_{0,1,2}$, the Hamiltonian is:

$$\hat{\mathcal{H}}_3' = \omega_c \hat{a}^\dagger \hat{a} + \sum_{j=0}^{2} (\omega_c + \Lambda_j)\hat{\Pi}_{jj} \tag{B.26}$$

We plot the calculated dispersive shift for the two-level case and the three-level case as a function of cavity occupation in Figure B.3. The two-level approximation captures the expected features, with the dispersive shifts for the two levels being symmetric and going to zero at large photon numbers. The three-level case is more interesting: we see that the dispersive shifts for both $|1\rangle$ and $|0\rangle$ are on the same
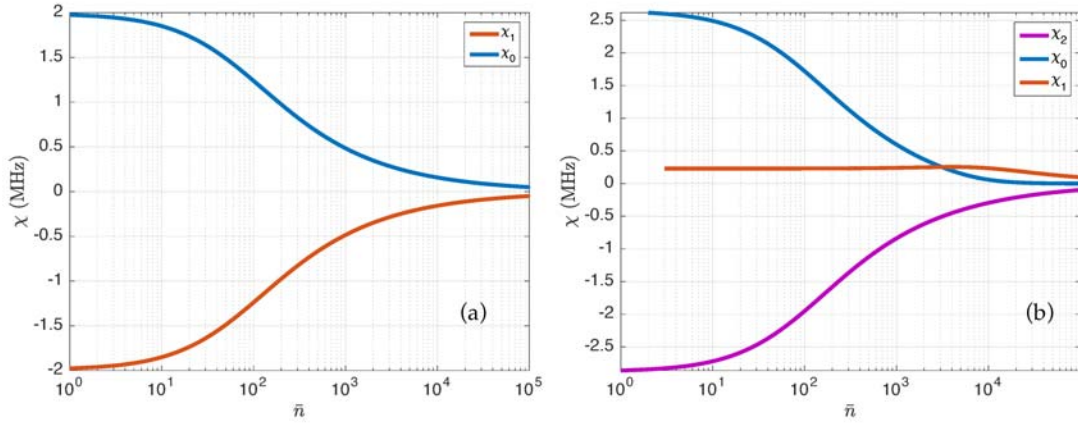
Figure B.3: Qubit dispersive shifts as a function of cavity photon number for (a) two-level qubit (b) three-level qubit. Parameters are $\omega_c = 5\,\text{GHz}$, $\omega_{10} = 4.5\,\text{GHz}$, low power $\chi_0 = 2\,\text{MHz}$, $\kappa = 6\,\text{MHz}$, $\alpha = -300\,\text{MHz}$ and a drive frequency $\omega_d = \omega_c + \chi$.
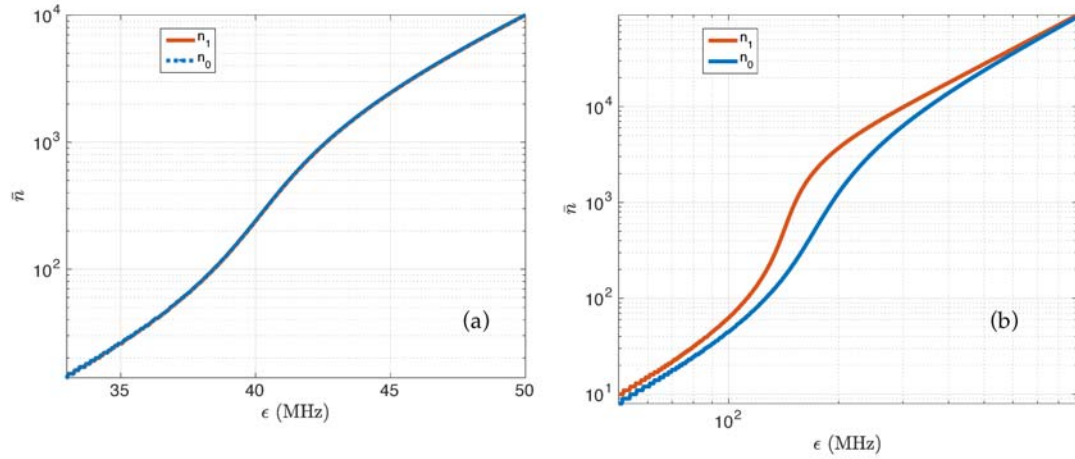
Figure B.4: Cavity occupation as a function of cavity drive strength $\epsilon = \kappa\sqrt{\bar{n}}/2$ for (a) two-level qubit and (b) three-level qubit. Parameters are the same as Figure B.3.

side of the cavity and have unequal magnitudes. The transition from the dispersive to the normal cavity state can be seen for the two-level qubit in Figure B.4a, while the modification of cavity occupation from the third level and the existence of a bright state is clear from Figure B.4b.

REFERENCES

[1]   Alvarez, Gabriel. 1988. Coupling-constant behavior of the resonances of the cubic anharmonic oscillator. *Phys. Rev. A* 37:4079–4083.

[2]   Ambegaokar, Vinay, and Alexis Baratoff. 1963. Tunneling between superconductors. *Phys. Rev. Lett.* 10:486–489.

[3]   Ansmann, Markus. 2009. Benchmarking the superconducting josephson phase qubit - the violation of bell's inequality. Ph.D. thesis, Unversity of California - Santa Barbara.

[4]   Aoyama, Shigeyoshi, Takayuki Myo, Kiyoshi Katō, and Kiyomi Ikeda. 2006. The complex scaling method for many-body resonances and its applications to three-body resonances. *Progress of Theoretical Physics* 116(1):1–35.

[5]   Baez, J. C., and B. Fong. 2015. A compositional framework for passive linear networks. ArXiv:1504.05625 [math.CT].

[6]   Balslev, E, and J.M. Combes. 1971. Spectral properties of many-body schrödinger operators with dilatation-analytic interactions. *Comm. Math Phys.* 22(4):280–294.

[7]   Bardeen, J., L. N. Cooper, and J. R. Schrieffer. 1957. Theory of superconductivity. *Phys. Rev.* 108:1175–1204.

[8]   Barends, R., J. Kelly, A. Megrant, A. Veitia, D. Sank, E. Jeffrey, T. C. White, J. Mutus, A. G. Fowler, B. Campbell, Y. Chen, Z. Chen, B. Chiaro, A. Dunsworth, C. Neill, P. O/'Malley, P. Roushan, A. Vainsencher, J. Wenner, A. N. Korotkov, A. N. Cleland, and John M. Martinis. 2014. Superconducting quantum circuits at the surface code threshold for fault tolerance. *Nature* 508(7497):500–503.

[9]   Barends, R., A. Shabani, L. Lamata, J. Kelly, A. Mezzacapo, U. Las Heras, R. Babbush, A. G. Fowler, B. Campbell, Y. Chen, Z. Chen, B. Chiaro, A. Dunsworth, E. Jeffrey, E. Lucero, A. Megrant, J. Y. Mutus, M. Neeley, C. Neill, P. J. J. O'Malley, C. Quintana, P. Roushan, D. Sank, A. Vainsencher, J. Wenner, T. C. White, E. Solano, H. Neven, and J. M. Martinis. 2016. Digitized adiabatic quantum computing with a superconducting circuit. ArXiv:1411.03316 [quant-ph].

[10] Barends, R., J. Wenner, M. Lenander, Y. Chen, R. C. Bialczak, J. Kelly, E. Lucero, P. O'Malley, M. Mariantoni, D. Sank, H. Wang, T. C. White, Y. Yin, J. Zhao, A. N. Cleland, John M. Martinis, and J. J. A. Baselmans. 2011. Minimizing quasiparticle generation from stray infrared light in superconducting quantum circuits. *Applied Physics Letters* 99(11).

[11] Besser, Les, and Rowan Gilmore. 2003. *Practical rf circuit design for modern wireless systems*, vol. I: Passive Circuits and Systems. Artech House.

[12] Bialczak, Radoslaw C., R. McDermott, M. Ansmann, M. Hofheinz, N. Katz, Erik Lucero, Matthew Neeley, A. D. O'Connell, H. Wang, A. N. Cleland, and John M. Martinis. 2007. $1/f$ flux noise in josephson phase qubits. *Phys. Rev. Lett.* 99:187006.

[13] Bishop, Lev S., Eran Ginossar, and S. M. Girvin. 2010. Response of the strongly driven jaynes-cummings oscillator. *Phys. Rev. Lett.* 105:100505.

[14] Bladh, K., D. Gunnarsson, E. Hurfeld, S. Devi, C. Kristoffersson, B. Smalander, S. Pehrson, T. Claeson, P. Delsing, and M. Taslakov. 2003. Comparison of cryogenic filters for use in single electronics experiments. *Rev. Sci. Instrum.* 74(3):1323.

[15] Blais, A., R.-S. Huang, A. Wallraff, Girvin S. M., and R. J. Schoelkopf. 2004. Cavity quantum electrodynamics for superconducting electrical circuits: An architecture for quantum computation. *Physical Review A* 69:062320.

[16] Boissonneault, Maxime, J. M. Gambetta, and Alexandre Blais. 2008. Nonlinear dispersive regime of cavity qed: The dressed dephasing model. *Phys. Rev. A* 77:060305.

[17] ———. 2009. Dispersive regime of circuit qed: Photon-dependent qubit dephasing and relaxation rates. *Phys. Rev. A* 79:013819.

[18] ———. 2010. Improved superconducting qubit readout by qubit-induced nonlinearities. *Phys. Rev. Lett.* 105:100504.

[19] Bouchiat, V, D Vion, P Joyez, D Esteve, and M H Devoret. 1998. Quantum coherence with a single cooper pair. *Physica Scripta* 1998(T76):165.

[20] Boulant, N., G. Ithier, P. Meeson, F. Nguyen, D. Vion, D. Esteve, I. Siddiqi, R. Vijay, C. Rigetti, F. Pierre, and M. Devoret. 2007. Quantum nondemolition readout using a josephson bifurcation amplifier. *Phys. Rev. B* 76:014525.

[21] BUNYK, PAUL, KONSTANTIN LIKHAREV, and DMITRY ZINOVIEV. 2001. Rsfq technology: Physics and devices. *International Journal of High Speed Electronics and Systems* 11(01):257–305.

[22] Bylander, Jonas, Simon Gustavsson, Fei Yan, Fumiki Yoshihara, Khalil Harrabi, George Fitch, David G. Cory, Yasunobu Nakamura, Jaw-Shen Tsai, and William D. Oliver. 2011. Noise spectroscopy through dynamical decoupling with a superconducting flux qubit. *Nat Phys* 7(7):565–570.

[23] Caldeira, A. O., and A. J. Leggett. 1981. Influence of dissipation on quantum tunneling in macroscopic systems. *Phys. Rev. Lett.* 46:211–214.

[24] Caldeira, A.O., and A.J. Leggett. 1983. Path integral approach to quantum brownian motion. *Physica A: Statistical Mechanics and its Applications* 121(3): 587 – 616.

[25] Caldeira, A.O, and A.J Leggett. 1983. Quantum tunnelling in a dissipative system. *Annals of Physics* 149(2):374 – 456.

[26] Catelani, G., S. E. Nigg, S. M. Girvin, R. J. Schoelkopf, and L. I. Glazman. 2012. Decoherence of superconducting qubits caused by quasiparticle tunneling. *Phys. Rev. B* 86:184514.

[27] Caves, Carlton M. 1982. Quantum limits on noise in linear amplifiers. *Phys. Rev. D* 26:1817–1839.

[28] Chen, Y.-F., D. Hover, S. Sendelbach, L. Maurer, S. T. Merkel, E. J. Pritchett, F. K. Wilhelm, and R. McDermott. 2011. Microwave photon counter based on josephson junctions. *Phys. Rev. Lett.* 107:217401.

[29] Chen, Zijun, A. Megrant, J. Kelly, R. Barends, J. Bochmann, Yu Chen, B. Chiaro, A. Dunsworth, E. Jeffrey, J. Y. Mutus, P. J. J. O'Malley, C. Neill, P. Roushan, D. Sank, A. Vainsencher, J. Wenner, T. C. White, A. N. Cleland, and John M. Martinis. 2014. Fabrication and characterization of aluminum airbridges for superconducting microwave circuits. *Applied Physics Letters* 104(5).

[30] Chow, Jerry M., Jay M. Gambetta, Easwar Magesan, David W. Abraham, Andrew W. Cross, B R Johnson, Nicholas A. Masluk, Colm A. Ryan, John A. Smolin, Srikanth J. Srinivasan, and M Steffen. 2014. Implementing a strand of a scalable fault-tolerant quantum computing fabric. *Nat Commun* 5.

[31] Clarke, John, and Frank K. Wilhelm. 2008. Superconducting quantum bits. *Nature* 453(7198):1031–1042.

[32] Clerk, A. A., M. H. Devoret, S. M. Girvin, Florian Marquardt, and R. J. Schoelkopf. 2010. Introduction to quantum noise, measurement, and amplification. *Rev. Mod. Phys.* 82:1155–1208.

[33] Corcoles, A. D., Easwar Magesan, Srikanth J. Srinivasan, Andrew W. Cross, M. Steffen, Jay M. Gambetta, and Jerry M. Chow. 2015. Demonstration of a quantum error detection code using a square lattice of four superconducting qubits. *Nat Commun* 6.

[34] Delabaere, Eric, and Duc Tai Trinh. 2000. Spectral analysis of the complex cubic oscillator. *Journal of Physics A: Mathematical and General* 33(48):8771.

[35] Deutsch, D. 1985. Quantum theory, the church-turing principle and the universal quantum computer. *Proceedings of the Royal Society of London A: Mathematical, Physical and Engineering Sciences* 400(1818):97–117.

[36] ———. 1989. Quantum computational networks. *Proceedings of the Royal Society of London A: Mathematical, Physical and Engineering Sciences* 425(1868): 73–90.

[37] Devoret, M. H. 1995. Quantum fluctuations in electrical circuits. *Les Houches, Session LXIII* 7(8).

[38] Devoret, M.H., and J. M. Martinis. 2004. Implementing qubits with superconducting integrated circuits. *Quantum Information Processing* 3(1-5):163–203.

[39] Devoret, M.H., and R. J. Schoelkopf. 2013. Superconducting circuits for quantum information: An outlook. *Science* 339(6124):1169–1174.

[40] Devoret, Michel H., Daniel Esteve, John M. Martinis, Andrew Cleland, and John Clarke. 1987. Resonant activation of a brownian particle out of a potential well: Microwave-enhanced escape from the zero-voltage state of a josephson junction. *Phys. Rev. B* 36:58–73.

[41] Devoret, Michel H., John M. Martinis, and John Clarke. 1985. Measurements of macroscopic quantum tunneling out of the zero-voltage state of a current-biased josephson junction. *Phys. Rev. Lett.* 55:1908–1911.

[42] Dial, O., D. T. McClure, S Poletto, J. M. Gambetta, D. W. Abraham, J. M. Chow, and M. Steffen. 2015. Bulk and surface loss in superconducting transmon qubits. ArXiv:1509.03859.

[43] DiVincenzo, D. P. 2000. The physical implementation of quantum computation. ArXiv:quant-ph/0002077.

[44] Dolan, G. J. 1977. Offset masks for lift-off photoprocessing. *Applied Physics Letters* 31(5):337.

[45] Feynman, R. P. 1982. Simulating physics with computers. *International Jounral of Theoretical Physics* 21(6/7):467–488.

[46] Fowler, Austin G., Matteo Mariantoni, John M. Martinis, and Andrew N. Cleland. 2012. Surface codes: Towards practical large-scale quantum computation. *Phys. Rev. A* 86:032324.

[47] Fowler, Austin G., Ashley M. Stephens, and Peter Groszkowski. 2009. High-threshold universal quantum computation on the surface code. *Phys. Rev. A* 80:052312.

[48] Frunzio, L., A. Wallraff, D. I. Schuster, J. Majer, and R. J. Schoelkopf. 2005. Fabrication and characterization of superconducting circuit qed devices for quantum computation. *IEEE Transactions on Applied Superconductivity* 15(2): 860–863.

[49] Gambetta, Jay, Alexandre Blais, M. Boissonneault, A. A. Houck, D. I. Schuster, and S. M. Girvin. 2008. Quantum trajectory approach to circuit qed: Quantum jumps and the zeno effect. *Phys. Rev. A* 77:012112.

[50] Gambetta, Jay, W. A. Braff, A. Wallraff, S. M. Girvin, and R. J. Schoelkopf. 2007. Protocols for optimal readout of qubits using a continuous quantum nondemolition measurement. *Phys. Rev. A* 76:012325.

[51] Gamow, G. 1928. Zur quantentheorie des atomkernes. *Zeitschrift für Physik* 51(3):204–212.

[52] Geerlings, K., Z. Leghtas, I. M. Pop, S. Shankar, L. Frunzio, R. J. Schoelkopf, M. Mirrahimi, and M. H. Devoret. 2013. Demonstrating a driven reset protocol for a superconducting qubit. *Phys. Rev. Lett.* 110:120501.

[53] Geller, Michael R., Emmanuel Donate, Yu Chen, Michael T. Fang, Nelson Leung, Charles Neill, Pedram Roushan, and John M. Martinis. 2015. Tunable coupler for superconducting xmon qubits: Perturbative nonlinear model. *Phys. Rev. A* 92:012320.

[54] Goppl, M., A. Fragner, M. Baur, R. Bianchetti, S. Filipp, J. M. Fink, P. J. Leek, G. Puebla, L. Steffen, and A. Wallraff. 2008. Coplanar waveguide resonators for circuit quantum electrodynamics. *Journal of Applied Physics* 104(11).

[55] Gottesman, D. 1997. Stabilizer codes and quantum error correction. Ph.D. thesis, Caltech.

[56] Govia, Luke C. G., Emily J. Pritchett, Seth T. Merkel, Deanna Pineau, and Frank K. Wilhelm. 2012. Theory of josephson photomultipliers: Optimal working conditions and back action. *Phys. Rev. A* 86:032311.

[57] Govia, Luke C. G., Emily J. Pritchett, B. L. T. Plourde, Maxim G. Vavilov, R. McDermott, and Frank K. Wilhelm. 2015. Scalable two- and four-qubit parity measurement with a threshold photon counter. *Phys. Rev. A* 92:022335.

[58] Govia, Luke C. G., Emily J. Pritchett, Canran Xu, B. L. T. Plourde, Maxim G. Vavilov, Frank K. Wilhelm, and R. McDermott. 2014. High-fidelity qubit measurement with a microwave-photon counter. *Phys. Rev. A* 90:062307.

[59] Hadfield, Robert H. 2009. Single-photon detectors for optical quantum information applications. *Nat Photon* 3(12):696–705.

[60] Hagmann, C., and P.L. Richards. 1995. Adiabatic demagnetization refrigerators for small laboratory experiments and space astronomy. *Cryogenics* 35(5): 303 – 309.

[61] Hansen, Nikolaus. 2011. The cma evolution strategy: A tutorial. Tech. Rep., Laboratoire de Recerce en Informatique.

[62] Ho Eom, Byeong, Peter K. Day, Henry G. LeDuc, and Jonas Zmuidzinas. 2012. A wideband, low-noise superconducting amplifier with high dynamic range. *Nat Phys* 8(8):623–627.

[63] Houck, A. A., J. A. Schreier, B. R. Johnson, J. M. Chow, Jens Koch, J. M. Gambetta, D. I. Schuster, L. Frunzio, M. H. Devoret, S. M. Girvin, and R. J. Schoelkopf. 2008. Controlling the spontaneous emission of a superconducting transmon qubit. *Phys. Rev. Lett.* 101:080502.

[64] Hover, D. 2013. Dispersive readout of a superconducting qubit using a slug amplifier. Ph.D. thesis, University of Wisconsin-Madison.

[65] Hover, D., Y.-F. Chen, G. J. Ribeill, S. Zhu, S. Sendelbach, and R. McDermott. 2012. Superconducting low-inductance undulatory galvanometer microwave amplifier. *Applied Physics Letters* 100(6):–.

[66] Hover, D., S. Zhu, T. Thorbeck, G. J. Ribeill, D. Sank, J. Kelly, R. Barends, John M. Martinis, and R. McDermott. 2014. High fidelity qubit readout with the superconducting low-inductance undulatory galvanometer microwave amplifier. *Applied Physics Letters* 104(15):–.

[67] Hutchings, M., and B. L. T. Plourde. 2015. personal communication.

[68] Inomata, K., Zhirong Lin, K. Koshino, W. D. Oliver, J. S. Tsai, T. Yamamoto, and Y. Nakamura. 2016. Single microwave-photon detector using an artificial lambda-type three-level system. ArXiv:1601.05513 [quant-ph].

[69] Jackson, J.D. 1988. *Classical electrodynamics*. 3rd ed. Wiley.

[70] Jacobs, K. 2014. *Quantum measurement theory and its applications*. 1st ed. Cambridge University Press.

[71] Jin, X. Y., S. Gustavsson, J. Bylander, F. Yan, F. Yoshihara, Y. Nakamura, T. P. Orlando, and W. D. Oliver. 2015. z-gate operation on a superconducting flux qubit via its readout squid. *Phys. Rev. Applied* 3:034004.

[72] Johansson, J. R., G. Johansson, C. M. Wilson, and Franco Nori. 2010. Dynamical casimir effect in superconducting microwave circuits. *Phys. Rev. A* 82: 052509.

[73] Johnson, B. R., M. D. Reed, A. A. Houck, D. I. Schuster, Lev S. Bishop, E. Ginossar, J. M. Gambetta, L. DiCarlo, L. Frunzio, S. M. Girvin, and R. J. Schoelkopf. 2010. Quantum non-demolition detection of single microwave photons in a circuit. *Nat Phys* 6(9):663–667.

[74] Kamon, M., M. J. Tsuk, and J. White. 1993. Fasthenry: A multipole-accelerated 3-d inductance extraction program. In *Proceedings of the 30th international design automation conference*, 678–683. DAC '93, New York, NY, USA: ACM.

[75] Katzgraber, Helmut G., H. Bombin, and M. A. Martin-Delgado. 2009. Error threshold for color codes and random three-body ising models. *Phys. Rev. Lett.* 103:090501.

[76] Kelly, J., R. Barends, B. Campbell, Y. Chen, Z. Chen, B. Chiaro, A. Dunsworth, A. G. Fowler, I.-C. Hoi, E. Jeffrey, A. Megrant, J. Mutus, C. Neill, P. J. J. O'Malley, C. Quintana, P. Roushan, D. Sank, A. Vainsencher, J. Wenner, T. C. White, A. N. Cleland, and John M. Martinis. 2014. Optimal quantum control using randomized benchmarking. *Phys. Rev. Lett.* 112:240504.

[77] Kelly, J., R. Barends, A. G. Fowler, A. Megrant, E. Jeffrey, T. C. White, D. Sank, J. Y. Mutus, B. Campbell, Yu Chen, Z. Chen, B. Chiaro, A. Dunsworth, I. C. Hoi, C. Neill, P. J. J. O/'Malley, C. Quintana, P. Roushan, A. Vainsencher, J. Wenner, A. N. Cleland, and John M. Martinis. 2015. State preservation by repetitive error detection in a superconducting quantum circuit. *Nature* 519(7541):66–69.

[78] Kitaev, A. Y. 1997. Quantum computations: algorithms and error correction. *Russian Mathematical Surveys* 52(6):1191.

[79] Kleinsasser, A. W., R. E. Miller, and W. H. Mallison. 1995. Dependence of critical current density on oxygen exposure in nb-alo$_x$-nb tunnel junctions. *IEEE Transactions on Applied Superconductivity* 5(1):26–30.

[80] Koblitz, N., and A. Menezes. 2015. A wriddle wrapped in an enigma. Cryptology ePrint Archive, Report 2015/1018. `http://eprint.iacr.org/`.

[81] Koch, Jens, Terri M. Yu, Jay Gambetta, A. A. Houck, D. I. Schuster, J. Majer, Alexandre Blais, M. H. Devoret, S. M. Girvin, and R. J. Schoelkopf. 2007. Charge-insensitive qubit design derived from the cooper pair box. *Phys. Rev. A* 76:042319.

[82] Koshino, Kazuki, Kunihiro Inomata, Zhirong Lin, Yasunobu Nakamura, and Tsuyoshi Yamamoto. 2015. Theory of microwave single-photon detection using an impedance-matched Λ system. *Phys. Rev. A* 91:043805.

[83] Kuroś, Arkadiusz, Przemysław Kościk, and Anna Okopińska. 2013. Determination of resonances by the optimized spectral approach. *Journal of Physics A: Mathematical and Theoretical* 46(8):085303.

[84] Lambert, W. D. 1906. A generalized trigonometric solution of the cubic equation. *The American Mathematical Monthly* 13(4):73–76.

[85] Lang, K.M., S. Nam, J. Aumentado, C. Urbina, and John M. Martinis. 2003. Banishing quasiparticles from josephson-junction qubits: why and how to do it. *Applied Superconductivity, IEEE Transactions on* 13(2):989–993.

[86] Larkin, A. I., and Yu. N. Ovchinnikov. 1985. Resonance reduction of the lifetime of the metastable state of tunnel junctions. *Journal of Low Temperature Physics* 63(3):317–329.

[87] Larkin, A.I., and Yu. N. Ovchinnikov. 1986. Effect of level quantization on the lifetime of metastable states. *Sov. Phys. JETP* 4(1):185–190.

[88] Larson, J., and S. Stenholm. 2006. Validity of adiabaticity in cavity qed. *Phys. Rev. A* 73:033805.

[89] Larson, Jonas. 2007. Dynamics of the jaynes–cummings and rabi models: old wine in new bottles. *Physica Scripta* 76(2):146.

[90] Leduc, Henry G., Bruce Bumble, Peter K. Day, Byeong Ho Eom, Jiansong Gao, Sunil Golwala, Benjamin A. Mazin, Sean McHugh, Andrew Merrill, David C. Moore, Omid Noroozian, Anthony D. Turner, and Jonas Zmuidzinas. 2010. Titanium nitride films for ultrasensitive microresonator detectors. *Applied Physics Letters* 97(10).

[91] Lenander, M., H. Wang, Radoslaw C. Bialczak, Erik Lucero, Matteo Mariantoni, M. Neeley, A. D. O'Connell, D. Sank, M. Weides, J. Wenner, T. Yamamoto, Y. Yin, J. Zhao, A. N. Cleland, and John M. Martinis. 2011. Measurement of energy decay in superconducting qubits from nonequilibrium quasiparticles. *Phys. Rev. B* 84:024501.

[92] Likharev, K. K. 1986. *Dynamics of josephson junctions and circuits*. CRC Press.

[93] Likharev, K. K., and V. K. Semenov. 1991. Rsfq logic/memory family: a new josephson-junction technology for sub-terahertz-clock-frequency digital systems. *IEEE Transactions on Applied Superconductivity* 1(1):3–28.

[94] Loss, D., and D. P. DiVincenzo. 1998. Quantum computation with quantum dots. *Physical Review A* 57(1):120–126.

[95] Louisell, W. H. 1964. *Radiation and noise in quantum electronics*. McGraw-Hill.

[96] Macklin, C., K. O'Brien, D. Hover, M. E. Schwartz, V. Bolkhovsky, X. Zhang, W. D. Oliver, and I. Siddiqi. 2015. A near–quantum-limited josephson traveling-wave parametric amplifier. *Science* 350(6258):307–310.

[97] Makhlin, Yuriy, and Alexander Shnirman. 2004. Dephasing of solid-state qubits at optimal points. *Phys. Rev. Lett.* 92:178301.

[98] Martinis, J. M., and A. Megrant. 2014. Ucsb final report for the csq program: Review of decoherence and materials physics for superconducting qubits. ArXiv:1410.5793.

[99] Martinis, John M., M. Ansmann, and J. Aumentado. 2009. Energy decay in superconducting josephson-junction qubits from nonequilibrium quasiparticle excitations. *Phys. Rev. Lett.* 103:097002.

[100] Martinis, John M., K. B. Cooper, R. McDermott, Matthias Steffen, Markus Ansmann, K. D. Osborn, K. Cicak, Seongshik Oh, D. P. Pappas, R. W. Simmonds, and Clare C. Yu. 2005. Decoherence in josephson qubits from dielectric loss. *Phys. Rev. Lett.* 95:210503.

[101] Martinis, John M., Michel H. Devoret, and John Clarke. 1985. Energy-level quantization in the zero-voltage state of a current-biased josephson junction. *Phys. Rev. Lett.* 55:1543–1546.

[102] ———. 1987. Experimental tests for the quantum behavior of a macroscopic degree of freedom: The phase difference across a josephson junction. *Phys. Rev. B* 35:4682–4698.

[103] Martinis, John M., S. Nam, J. Aumentado, K. M. Lang, and C. Urbina. 2003. Decoherence of a superconducting qubit due to bias noise. *Phys. Rev. B* 67: 094510.

[104] McDermott, R., and M. G. Vavilov. 2014. Accurate qubit control with single flux quantum pulses. *Phys. Rev. Applied* 2:014007.

[105] Megrant, A., C. Neill, R. Barends, B. Chiaro, Yu Chen, L. Feigl, J. Kelly, Erik Lucero, Matteo Mariantoni, P. J. J. O'Malley, D. Sank, A. Vainsencher, J. Wenner, T. C. White, Y. Yin, J. Zhao, C. J. Palmstrøm, John M. Martinis, and A. N. Cleland. 2012. Planar superconducting resonators with internal quality factors above one million. *Applied Physics Letters* 100(11).

[106] Mermin, N. D. 2007. *Quantum computer science: An introduction.* 1st ed. Cambridge University Press.

[107] Miller, R, T E Northup, K M Birnbaum, A Boca, A D Boozer, and H J Kimble. 2005. Trapped atoms in cavity qed: coupling quantized light and matter. *Journal of Physics B: Atomic, Molecular and Optical Physics* 38(9):S551.

[108] Moiseyev, Nimrod. 1998. Quantum theory of resonances: calculating energies, widths and cross-sections by complex scaling. *Physics Reports* 302(5–6):212 – 293.

[109] Mutus, J. Y., T. C. White, E. Jeffrey, D. Sank, R. Barends, J. Bochmann, Yu Chen, Z. Chen, B. Chiaro, A. Dunsworth, J. Kelly, A. Megrant, C. Neill, P. J. J. O'Malley, P. Roushan, A. Vainsencher, J. Wenner, I. Siddiqi, R. Vijay, A. N. Cleland, and John M. Martinis. 2013. Design and characterization of a lumped element single-ended superconducting microwave parametric amplifier with on-chip flux bias line. *Applied Physics Letters* 103(12).

[110] Nakamura, Y., Yu. A. Pashkin, and J. S. Tsai. 1999. Coherent control of macroscopic quantum states in a single-cooper-pair box. *Nature* 398:786–788.

[111] Neill, C., A. Megrant, R. Barends, Yu Chen, B. Chiaro, J. Kelly, J. Y. Mutus, P. J. J. O'Malley, D. Sank, J. Wenner, T. C. White, Yi Yin, A. N. Cleland, and John M. Martinis. 2013. Fluctuations from edge defects in superconducting resonators. *Applied Physics Letters* 103(7).

[112] Nielsen, M. A., and I. L. Chuang. 2000. *Quantum computation and quantum information*. Cambridge University Press.

[113] Nsanzineza, I., and B. L. T. Plourde. 2014. Trapping a single vortex and reducing quasiparticles in a superconducting resonator. *Phys. Rev. Lett.* 113.

[114] O'Malley, P. J. J.., J. Kelly, R. Barends, B. Campbell, Y. Chen, Z. Chen, B. Chiaro, A. Dunsworth, A. G. Fowler, I.-C. Hoi, E. Jeffrey, A. Megrant, J. Mutus, C. Neill, C. Quintana, P. Roushan, D. Sank, A. Vainsencher, J. Wenner, T. C. White, A. N. Korotkov, A. N. Cleland, and John M. Martinis. 2015. Qubit metrology of ultralow phase noise using randomized benchmarking. *Phys. Rev. Applied* 3:044009.

[115] Poudel, A., R. McDermott, and M. G. Vavilov. 2012. Quantum efficiency of a microwave photon detector based on a current-biased josephson junction. *Phys. Rev. B* 86:174506.

[116] Pozar, D. M. 2011. *Microwave engineering*, vol. 4. Wiley.

[117] Pozar, David M. 2004. *Microwave engineering*. 3rd ed. Wiley.

[118] Quintana, C. M., A. Megrant, Z. Chen, A. Dunsworth, B. Chiaro, R. Barends, B. Campbell, Yu Chen, I.-C. Hoi, E. Jeffrey, J. Kelly, J. Y. Mutus, P. J. J. O'Malley,

C. Neill, P. Roushan, D. Sank, A. Vainsencher, J. Wenner, T. C. White, A. N. Cleland, and John M. Martinis. 2014. Characterization and reduction of microfabrication-induced decoherence in superconducting quantum circuits. *Applied Physics Letters* 105(6).

[119] Reed, M. D. 2013. Entanglement and quantum error correction with superconducting qubits. Ph.D. thesis, Yale University.

[120] Reed, M. D., L. DiCarlo, B. R. Johnson, L. Sun, D. I. Schuster, L. Frunzio, and R. J. Schoelkopf. 2010. High-fidelity readout in circuit quantum electrodynamics using the jaynes-cummings nonlinearity. *Phys. Rev. Lett.* 105: 173601.

[121] Renker, D. 2006. Geiger-mode avalanche photodiodes, history, properties and problems. *Nuclear Instruments and Methods in Physics Research Section A: Accelerators, Spectrometers, Detectors and Associated Equipment* 567(1):48 – 56.

[122] Ribeill, G. J., D. Hover, Y.-F. Chen, S. Zhu, and R. McDermott. 2011. Superconducting low-inductance undulatory galvanometer microwave amplifier: Theory. *Journal of Applied Physics* 110(10):–.

[123] Richards, P.L., T.M. Shen, R.E. Harris, and F.L. Lloyd. 1980. Superconductor-insulator-superconductor quasiparticle junctions as microwave photon detectors. *Applied Physics Letters* 36:480.

[124] Rigetti, Chad, Jay M. Gambetta, Stefano Poletto, B. L. T. Plourde, Jerry M. Chow, A. D. Córcoles, John A. Smolin, Seth T. Merkel, J. R. Rozen, George A. Keefe, Mary B. Rothwell, Mark B. Ketchen, and M. Steffen. 2012. Superconducting qubit in a waveguide cavity with a coherence time approaching 0.1 ms. *Phys. Rev. B* 86:100506.

[125] Romero, G., J. J. García-Ripoll, and E. Solano. 2009. Microwave photon detector in circuit qed. *Phys. Rev. Lett.* 102:173602.

[126] Saffman, M., T. G. Walker, and K. Mølmer. 2010. Quantum information with rydberg atoms. *Reviews of Modern Physics* 82(3):2313–2363.

[127] Sakurai, J.J. 1993. *Modern quantum mechanics*. Addison Wesley.

[128] Sank, Daniel, R. Barends, Radoslaw C. Bialczak, Yu Chen, J. Kelly, M. Lenander, E. Lucero, Matteo Mariantoni, A. Megrant, M. Neeley, P. J. J. O'Malley, A. Vainsencher, H. Wang, J. Wenner, T. C. White, T. Yamamoto, Yi Yin, A. N.

Cleland, and John M. Martinis. 2012. Flux noise probed with real time qubit tomography in a josephson phase qubit. *Phys. Rev. Lett.* 109:067001.

[129] Sathyamoorthy, S. R., T. M. Stace, and G. Johansson. 2015. Detecting itinerant single microwave photons. ArXiv:1504.04970 [quant-ph].

[130] Schondorf, Marius. 2015. Optimization conditions for a jpm coupled to a transmission line. Pers. comm.

[131] Schuster, D. I. 2007. Circuit quantum electrodynamics. Ph.D. thesis, Yale University.

[132] Sete, Eyob A., Andrei Galiautdinov, Eric Mlinar, John M. Martinis, and Alexander N. Korotkov. 2013. Catch-disperse-release readout for superconducting qubits. *Phys. Rev. Lett.* 110:210501.

[133] Shankar, R. 2011. *Principles of quantum mechanics*. 2nd ed. Plenum Press.

[134] Shor, P. W. 1997. Polynomial-time algorithms for prime factorization and discrete logarithms on a quantum computer. *SIAM Journal on Computing* 26(5):1484–1509.

[135] Simons, Rainee N. 2001. *Coplanar waveguide circuits, components and systems*. Wiley-IEEE Press.

[136] Song, C., M. P. DeFeo, K. Yu, and B. L. T. Plourde. 2009. Reducing microwave loss in superconducting resonators due to trapped vortices. *Applied Physics Letters* 95(23).

[137] Strand, J. D., Matthew Ware, Félix Beaudoin, T. A. Ohki, B. R. Johnson, Alexandre Blais, and B. L. T. Plourde. 2013. First-order sideband transitions with flux-driven asymmetric transmon qubits. *Phys. Rev. B* 87:220505.

[138] Strauch, F. W. 2004. Theory of superconducting phase qubits. Ph.D. thesis, University of Maryland, College Park.

[139] Taylor, John R. 1997. *An introduction to error analysis*. 2nd ed. University Science Books.

[140] Tinkham, M. 2004. *Introduction to superconductivity*. 2nd ed. Dover Publications.

[141] Van Duzer, T., and C. W. Turner. 1998. *Principles of superconductive devices and circuits*. 2nd ed. Prentice Hall.

[142] Vernon Jr., F. L., and R. J. Pedersen. 1968. Relaxation oscillations in josephson junctions. *J. Appl. Phys.* 39:2661.

[143] Vijay, R., C. Macklin, D. H. Slichter, S. J. Weber, K. W. Murch, R. Naik, A. N. Korotkov, and I. Siddiqi. 2012. Stabilizing rabi oscillations in a superconducting qubit using quantum feedback. *Nature* 490(7418):77–80.

[144] Vijay, R., D. H. Slichter, and I. Siddiqi. 2011. Observation of quantum jumps in a superconducting artificial atom. *Phys. Rev. Lett.* 106:110502.

[145] Vion, D., A. Aassime, A. Cottet, P. Joyez, H. Pothier, C. Urbina, D. Esteve, and M. H. Devoret. 2002. Manipulating the quantum state of an electrical circuit. *Science* 296(5569):886–889. `http://science.sciencemag.org/content/296/5569/886.full.pdf`.

[146] Vogel, W, and D.-G. Welsch. 2006. *Quantum optics*. 3rd ed. Wiley-VCH.

[147] Wallraff, A., D. I. Schuster, A. Blais, L. Frunzio, J. Majer, M. H. Devoret, S. M. Girvin, and R. J. Schoelkopf. 2005. Approaching unit visibility for control of a superconducting qubit with dispersive readout. *Phys. Rev. Lett.* 95:060501.

[148] Walther, Herbert, Benjamin T H Varcoe, Berthold-Georg Englert, and Thomas Becker. 2006. Cavity quantum electrodynamics. *Reports on Progress in Physics* 69(5):1325.

[149] Wang, C., Y. Y. Gao, I. M. Pop, U. Vool, C. Axline, T. Brecht, R. W. Heeres, L. Frunzio, M. H. Devoret, G. Catelani, L. I. Glazman, and R. J. Schoelkopf. 2014. Measurement and control of quasiparticle dynamics in a superconducting qubit. *Nat Commun* 5.

[150] Ware, Matthew. 2015. Flux-tunable superconducting transmons for quantum information processing. Ph.D. thesis, Syracuse University.

[151] Weber, J. R., W. F. Koehl, J. B. Varley, A. Janotti, B. B. Buckley, C. G. Van de Walle, and D. D. Awschalom. 2010. Quantum computing with defects. *Proceedings of the National Academy of Sciences* 107(19):8513–8518.

[152] Wells, D. A. 1938. Application of the lagrangian equations to electrical circuits. *J. Appl. Phys.* 9:312–320.

[153] Wenner, J., Yi Yin, Yu Chen, R. Barends, B. Chiaro, E. Jeffrey, J. Kelly, A. Megrant, J. Y. Mutus, C. Neill, P. J. J. O'Malley, P. Roushan, D. Sank, A. Vainsencher, T. C. White, Alexander N. Korotkov, A. N. Cleland, and John M. Martinis. 2014. Catching time-reversed microwave coherent state photons with 99.4% absorption efficiency. *Phys. Rev. Lett.* 112:210501.

[154] Wenner, J., Yi Yin, Erik Lucero, R. Barends, Yu Chen, B. Chiaro, J. Kelly, M. Lenander, Matteo Mariantoni, A. Megrant, C. Neill, P. J. J. O'Malley, D. Sank, A. Vainsencher, H. Wang, T. C. White, A. N. Cleland, and John M. Martinis. 2013. Excitation of superconducting qubits from hot nonequilibrium quasiparticles. *Phys. Rev. Lett.* 110:150502.

[155] White, Guy K., and Philip Meeson. 2002. *Experimental techniques in low-temperature physics*. 4th ed. Oxford University Press.

[156] White, T. C., J. Y. Mutus, J. Dressel, J. Kelly, R. Barends, E. Jeffrey, D. Sank, A. Megrant, B. Campbell, Y. Chen, Z. Chen, B. Chiaro, A. Dunsworth, I.-C. Hoi, C. Neill, P. J. J. O'Malley, P. Roushan, A. Vainsencher, J. Wenner, A. N. Korotkov, and J. M. Martinis. 2015. Preserving entanglement during weak measurement demonstrated with a violation of the bell–leggett–garg inequality. *npj Quantum Information* 2:15022.

[157] White, T. C., J. Y. Mutus, I.-C. Hoi, R. Barends, B. Campbell, Yu Chen, Z. Chen, B. Chiaro, A. Dunsworth, E. Jeffrey, J. Kelly, A. Megrant, C. Neill, P. J. J. O'Malley, P. Roushan, D. Sank, A. Vainsencher, J. Wenner, S. Chaudhuri, J. Gao, and John M. Martinis. 2015. Traveling wave parametric amplifier with josephson junctions using minimal resonator phase matching. *Applied Physics Letters* 106(24):–.

[158] Wu, Ying, and Xiaoxue Yang. 1997. Effective two-level model for a three-level atom in the Ξ configuration. *Phys. Rev. A* 56:2443–2446.

[159] Yaakobi, O., L. Friedland, C. Macklin, and I. Siddiqi. 2013. Parametric amplification in josephson junction embedded transmission lines. *Phys. Rev. B* 87:144301.

[160] Yaris, R, and P Winkler. 1978. Electron scattering resonances using dilatation transformations. i. condition for dilatational stability. *Journal of Physics B: Atomic and Molecular Physics* 11(8):1475.

[161] Yaris, Robert, John Bendler, Ronald A. Lovett, Carl M. Bender, and Peter A. Fedders. 1978. Resonance calculations for arbitrary potentials. *Phys. Rev. A* 18:1816–1825.

[162] Yurke, Bernard, and John S. Denker. 1984. Quantum network theory. *Phys. Rev. A* 29:1419–1437.

[163] Zhang, Z., R. Rajavel, P. Deelman, and P. Fay. 2011. Sub-micron area heterojunction backward diode millimeter-wave detections with 0.18 pw/hz$^{1/2}$ noise equivalent power. *IEEE Microwave and Wireless Components Letters* 21(5): 267–269.